UNIVERSIDADE FEDERAL DE SÃO CARLOS
Centro de Ciências Exatas e de Tecnologia
Departamento de Química
PROGRAMA DE PÓS-GRADUAÇÃO EM QUÍMICA

"MÉTODO EXPERIMENTAL/TEÓRICO PARA INTERPRETAÇÃO DE SEMICONDUTORES INORGÂNICOS"

Amanda Fernandes Gouveia*

Tese apresentada como parte dos requisitos para obtenção do título de DOUTORA EM CIÊNCIAS, área de concentração: QUÍMICA INORGÂNICA.

Orientador: Elson Longo

***bolsista FAPESP (nº 2013/26671-9)**

São Carlos - SP

2018

UNIVERSIDADE FEDERAL DE SÃO CARLOS

Centro de Ciências Exatas e de Tecnologia
Programa de Pós-Graduação em Química

Folha de Aprovação

Assinaturas dos membros da comissão examinadora que avaliou e aprovou a Defesa de Tese de Doutorado da candidata Amanda Fernandes Gouveia, realizada em 27/07/2018:

Prof. Dr. Elson Longo da Silva
UFSCar

Prof. Dr. Miguel Angel San-Miguel Barrera
UNICAMP

Profa. Dra. Ieda Lucia Viana Rosa
UFSCar

Prof. Dr. Luís Fernando da Silva
UFSCar

Profa. Dra. Maria Aparecida Zaghete Bertochi
UNESP

PUBLICAÇÕES

Publicações Presentes

1. PEREIRA, P. F. S.; GOUVEIA, A. F.; ASSIS, M.; DE OLIVEIRA, R. C.; PINATTI, I. M.; PENHA, M.; GONÇALVES, R. F.; GRACIA, L.; ANDRÉS, J. & LONGO, E. "$ZnWO_4$ nanocrystals: synthesis, morphology, photoluminescence and photocatalytic properties". Phys. Chem. Chem. Phys., **20**: 1923, 2018.

2. ANDRÉS, J.; GRACIA, L.; GOUVEIA, A. F.; FERRER, M. M. & LONGO, E. "Effects of surface stability on the morphological transformation of metals and metal oxides as investigated by first-principles calculations". Nanotechnology, **26**: 405703, 2015.

3. GOUVEIA, A. F.; FERRER, M. M.; SAMBRANO, J. R.; ANDRÉS, J. & LONGO, E. "Modeling the atomic-scale structure, stability, and morphological transformations in the tetragonal phase of $LaVO_4$". Chem. Phys. Lett., **660**: 87, 2016.

4. MACEDO, N. G.; GOUVEIA, A. F.; ROCA, R. A.; ASSIS, M.; GRACIA, L.; ANDRÉS, J.; LEITE, E. R. & LONGO, E. "Surfactant-mediated morphology and photocatalytic activity of α-Ag_2WO_4 material". J. Phys. Chem. C, 122 (15): 8667, 2018.

Outras Publicações

5. SANTANNA, M. A.; MENEZES, W. T.; SANTANA, Y. V. B.; FERRER, M. M.; GOUVEIA, A. F.; FACETO, A. D.; TEREZO, A. J.; OLIVEIRA, A. J. A.; LONGO, E.; FREITAS, R. G. & PEREIRA, E. C. "The effect of TiO_2 nanotube morphological engineering and ZnS quantum dots on the water splitting reaction: A theoretical and experimental study". Int. J. Hydrogen Energy, **43**: 6838, 2018.

6. TRENCH, A. B.; MACHADO, T. R.; GOUVEIA, A. F.; ASSIS, M.; DA TRINDADE, L. G.; SANTOS, C.; PERRIN, A.; PERRIN, C.; OLIVA, M.; ANDRÉS, J. & LONGO, E.

"Connecting structural, optical, and electronic properties and photocatalytic activity of Ag_3PO_4:Mo complemented by DFT calculations". Appl. Catal., B, **238**: 198, 2018.

7. PEREIRA, P. F. S.; SANTOS, C. C.; GOUVEIA, A. F.; FERRER, M. M.; PINATTI, I. M.; BOTELHO, G.; SAMBRANO, J. R.; ROSA, I. L. V.; ANDRÉS, J. & LONGO, E. "α-$Ag_{2-2x}Zn_xWO_4$ ($0 \leq x \leq 0.25$) solid solutions: Structure, morphology, and optical properties". Inorg. Chem., **56**: 7360, 2017.

8. ROCA, R. A.; GOUVEIA, A. F.; LEMOS, P. S.; GRACIA, L.; ANDRÉS, J. & LONGO, E. "Formation of Ag nanoparticles on β-Ag_2WO_4 through electron beam irradiation: A synergetic computational and experimental study". Inorg. Chem., **55**: 8661, 2016.

9. GOUVEIA, A. F.; SCZANCOSKI, J. C.; FERRER, M. M.; LIMA, A. S.; SANTOS, M. R. M. C.; LI, M. SIU; SANTOS, R. S.; LONGO, E. & CAVALCANTE, L. S. "Experimental and theoretical investigations of electronic structure and photoluminescence properties of α-Ag_2MoO_4 microcrystals". Inorg. Chem., **53**: 5589, 2014.

10. ASSIS, M.; CORDONCILLO, E.; TORRES-MENDIETA, R.; BELTRAN, H.; MINGUEZ-VEGA, G.; GOUVEIA, A. F.; LEITE, E. R.; ANDRÉS, J. & LONGO, E. "Laser-induced formation of bismuth nanoparticles". Phys. Chem. Chem. Phys., Accepted Manuscript, 2018.

11. ANDRÉS, J.; GOUVEIA, A. F.; GRACIA, L.; LONGO, E.; MANZEPPI FACCIN, G.; DA SILVA, E. Z.; PEREIRA, D. H. & SAN-MIGUEL, M. A. "Formation of Ag nanoparticles under electron beam irradiation: Atomistic origins from first-principles calculations". Int. J. Quantum Chem., **118**: e25551, 2017.

12. BYZYNSKI, G.; MELO, C.; VOLANTI, D. P.; FERRER, M. M.; GOUVEIA, A. F.; RIBEIRO, C.; ANDRÉS, J. & LONGO, E. "The interplay between morphology and photocatalytic activity in ZnO and N-doped ZnO crystals". Mater. Des., **120**: 363, 2017.

13. FERRER, M. M.; GOUVEIA, A. F.; GRACIA, L.; LONGO, E. & ANDRÉS, J. "A 3D platform for the morphology modulation of materials: first principles calculations on the thermodynamic stability and surface structure of metal oxides: Co_3O_4, α-Fe_2O_3, and In_2O_3". Modell. Simul. Mater. Sci. Eng., **24**: 025007, 2016.

14. LEMOS, P. S.; ALTOMARE, A.; GOUVEIA, A. F.; NOGUEIRA, I. C.; GRACIA, L.; LLUSAR, R.; ANDRÉS, J.; LONGO, ELSON & CAVALCANTE, L. S. "Synthesis and characterization of metastable β-Ag_2WO_4: An experimental and theoretical approach". Dalton Trans., **45**: 1185, 2016.

15. FERRER, M. M.; DE SANTANA, Y. V. B.; RAUBACH, C. W.; LA PORTA, F. A.; GOUVEIA, A. F.; LONGO, E. & SAMBRANO, J. R. "Europium doped zinc sulfide: a correlation between experimental and theoretical calculations". J. Mol. Model., **20**: 2375, 2014.

16. LONGO, V. M.; DE FOGGI, C. C.; FERRER, M. M.; GOUVEIA, A. F.; ANDRÉ, R. S.; AVANSI, W.; VERGANI, C. E.; MACHADO, A. L.; ANDRÉS, J.; CAVALCANTE, L. S.; HERNANDES, A. & LONGO, E. "Potentiated electron transference in α-Ag_2WO_4 microcrystals with Ag nanofilaments as microbial agent". J. Phys. Chem. A, **118**: 5769, 2014.

“A fé nos mantêm vivos e confiantes na certeza de que o Senhor cuida de nós nas tempestades mais agitadas da vida.”

AGRADECIMENTOS

Quero agradecer primeiramente a **Deus**, pelo dom da sabedoria e inteligência, pois sem os quais não seria possível finalizar mais uma etapa da minha vida.

Ao meu orientador, **Prof. Dr. Elson Longo** por ter acreditado no meu trabalho, auxiliando-me em todos os momentos e, principalmente, por todo conhecimento transmitido.

Ao Laboratório Interdisciplinar de Eletroquímica & Cerâmica (LIEC) e ao Centro de Desenvolvimento de Materiais Funcionais (CDMF), em especial: **Andressa**, **Aline**, **Daniela**, **Camila**, **Luma**, **Marcelo**, **Marisa**, **Mateus**, **Paula**, **Renan** e **Thiago**.

Ao **Prof. Dr. Juan Andrés** por ter aceitado ser o meu orientador no período do doutorado sanduíche e também pelos seus ensinamentos.

A **Profª. Drª. Lourdes Gracia** por estar sempre disponível a esclarecer minhas dúvidas ao longo do desenvolvimento do projeto.

Ao apoio financeiro concedido pela **FAPESP** (N° do Processo: 2013/26671-9) e **FAPESP/BEPE** (N° do Processo: 2017/07240-8);

Ao apoio financeiro concedido pelo **CNPq** (N° do Processo: 140830/2014-6);

Ao apoio financeiro concedido pela **CAPES/PDSE** (N° do Processo: 99999.002998/2014-9);

Ao Programa de **Pós-Graduação em Química** da UFSCar, por ter me aceitado como aluna.

A todos da minha **família** que sempre incentivaram e apoiaram meus estudos, principalmente **meus pais**, **Walter** e **Amália**.

Ao meu esposo, **Diego**, com muito amor e carinho.

LIST OF TABLES

LIST OF FIGURES

LIST OF SCHEME

RESUMO

MÉTODO EXPERIMENTAL/TEÓRICO PARA INTERPRETAÇÃO DE SEMICONDUTORES INORGÂNICOS. Sabe-se que a morfologia, a dimensionalidade e a estrutura cristalina dos materiais desempenham papéis importantes nas propriedades eletrônicas, ópticas, catalíticas, dentre outras. Compreender o papel dessas superfícies e encontrar a sua relação com sua física e química são de extrema importância. Os cálculos teóricos das superfícies fornecem um conhecimento profundo sobre os tipos de defeitos superficiais, isto é, vacâncias de oxigênio e distorções locais, e como elas estão ligadas com as propriedades dos semicondutores, tais como diminuição do valor do *band gap*, melhora da fotocatálise dentre outras. Um dos objetivos deste projeto foi associar os resultados experimentais e teóricos, a fim de proporcionar uma melhor compreensão das estruturas e propriedades eletrônicas de ambos nanocristais de tungstato de zinco ($ZnWO_4$) e dos cristais de tungstato de prata (α-Ag_2WO_4) como semicondutores inorgânicos representativos. Por meio dos cálculos de primeiro princípios, baseados na construção de Wulff, foi possível prever a morfologia desses materiais e, em particular explicar como ocorre o processo fotocatalítico dos nanocristais de $ZnWO_4$, assim como o efeito da utilização de surfactante na síntese e na atividade fotocatalítica dos cristais de α-Ag_2WO_4.

Palavras-Chave: Semicondutor Inorgânico. Síntese. Morfologia. DFT. Construção de Wulff.

ABSTRACT

EXPERIMENTAL/THEORETICAL METHOD FOR INTERPRETING INORGANIC SEMICONDUCTORS. It is known that the morphology, dimensionality and crystalline structure of materials play important roles in electronic, optical, catalytic properties, among others. Understanding the role of these surfaces and find a relationship with their physical and chemical are of extreme importance. The theoretical calculations of the surfaces provide a deep knowledge about the kind of superficial defect, i.e. oxygen vacancies and local distortions, and how they are linked with the semiconductor properties, such as decrease of the band gap value, improve in the photocatalysis among others. One of the objectives of this project was to associate experimental and theoretical results in order to provide a better understanding of the structural and electronic properties of both zinc tungstate ($ZnWO_4$) nanocrystals and silver tungstate (α-Ag_2WO_4) crystals, as representative inorganic semiconductors. By means of the first-principle calculations, based on the Wulff construction, it was possible to predict the morphology of these materials and, in particular, explaining how the photocatalytic process of the $ZnWO_4$ nanocrystals occurs, as well as the effect of the surfactant on the photocatalytic activity of the as-synthetized α-Ag_2WO_4.

Keywords: Inorganic Semiconductor. Synthesis. Morphology. DFT. Wulff Construction.

SUMÁRIO

1 – INTRODUCTION

The word “material” includes the kinds of substances, pure or mixed, that are used to construct a device with a desirable property.[1,2] The importance of the materials in human life is so significant that different periods of civilization have been defined according to the material used at the moment, for example: the age of stone, bronze, and iron.[1] In this context, the society always aims to improve the properties of the materials in order to develop new technological devices, generating breakthroughs in all areas of the industry and technology.[3] A good example of the synergy between scientific discovery and technological development, according to Cushing and co-authors,[3] is the electronics industry, where it has led to the development of ever smaller electronic devices with higher capacities and processing speeds.

A class of material that has great interest is the inorganic semiconductors that are defined as inorganic solids capable of changing their conductivity, passing from an insulator to a conductor. This increase in the electrical conductivity is directly related to the presence of a forbidden region separating the valence band (VB) and the conduction band (CB), called band gap region. As a result, when some energy is supplied to the solid, electrons are excited from the VB to the CB gaining some mobility in the system. The strong point of the inorganic semiconductors is the fact that electrical conductivity can be altered by external and internal stimuli,[4] which encourages many research groups to study these materials.[5-8]

In the field of materials research it is very common find papers in which the experimental and theoretical works are combined. These two lines of research, when applied together, provoke a favorable synergism, being a powerful tool to study and to explain the structural and electronic properties of the materials, responsible of the subsequent technological applications. Therefore, there are two research fronts: (1) the experimental line in which the aim is the development of new syntheses methodology to find a material with desirable properties and (2) the theoretical line in which the first-principles calculations complement experimental results, being a fundamental guide to a rational design of innovative materials.

Figure 1 illustrates a schematic representation of the study of the materials. Depending on the syntheses applied and the materials in question, the as-synthetized materials can present size in the micro- or nano-scale, for example. From

the structural parameters obtained by the experimental results, it is possible to construct the adequate theoretical model and by means of first-principles calculations find the nature of the mechanism to explain the materials properties in order to apply in certain applications.

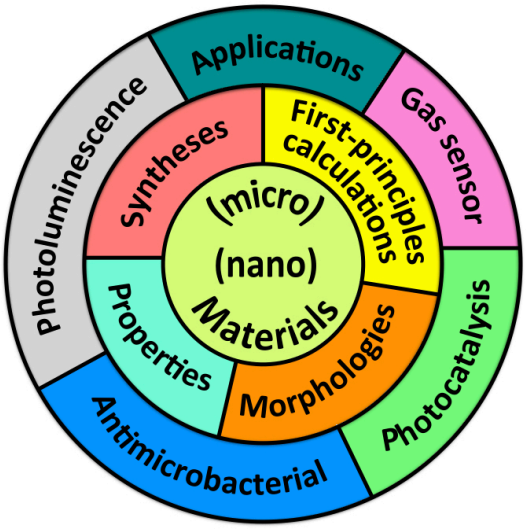

FIGURE 1 – Schematic representation of the study of materials.

The control of crystal morphology is a complex and difficult process, which depends both on the crystal internal structures process and external factors. There are important factors involved in a synthesis process that affect the final morphology of the end product, including the precursor, solvent, temperature, organic and inorganic additives, reducing agent, ligand agent, capping agent, and so on.

It is known that the morphology, dimensionality and crystalline structure of materials play important roles in electronic, optical, catalytic properties, among others.[9,10] Understanding the role of theses surfaces and find a relationship with their physical and chemical are of extreme importance. The crystal morphology is composed of different exposed surfaces in which the metal clusters (the local coordination of the metal), as the constituent building blocks of the materials, present under-coordinated positions. From the surface energy calculations it is possible to obtain the crystals shape applying the Wulff construction.[11,12] This simple method offers a methodology to determine the equilibrium crystal shape, i.e. the morphology. By a proper adjustment of the ratio of the values for the surface energy of different surfaces it was possible to find a given morphology and to construct a map of available morphologies for different kinds of inorganic semiconductors.

The inorganic semiconductors investigated by an experimental and theoretical approach in this thesis were the $ZnWO_4$ and the α-Ag_2WO_4. In the case of $ZnWO_4$ nanocrystals study, the principal aim it was to find the effect of the temperature on their morphology, photoluminescence properties and photocatalytic activity and to investigate the role of the each surface. In the α-Ag_2WO_4 study, the morphology was manipulated by a simple controlled-precipitation method with and without the presence of the anionic surfactant sodium dodecyl sulfate along with the synthesis method and an energy profile was built from the polyhedron energy associating the surface energy and the Wulff construction.

The focus of this thesis was the achievement of an interdisciplinary research, from fundamental to applications, in inorganic semiconductors with different sizes. In some results were used the theoretical and experimental approach to better discuss the materials properties and demonstrated how the methods and techniques of the theoretical and computational chemistry can be used for an understanding of physical and chemical properties of semiconductors for searching a rational material design.

2 – PUBLISHED ARTICLES

The published articles that compose this doctoral thesis with the associated experimental and theoretical approach are found at the following pages.

2.1 – $ZnWO_4$ nanocrystals: synthesis, morphology, photoluminescence and photocatalytic properties

PCCP

PAPER

Check for updates

Cite this: *Phys. Chem. Chem. Phys.*, 2018, **20**, 1923

$ZnWO_4$ nanocrystals: synthesis, morphology, photoluminescence and photocatalytic properties†

P. F. S. Pereira,[a] A. F. Gouveia,[a] M. Assis,[a] R. C. de Oliveira,[a] I. M. Pinatti,[a] M. Penha,[a] R. F. Gonçalves,[b] L. Gracia,[c] J. Andrés *[d] and E. Longo[a]

The present joint experimental and theoretical work provides in-depth understanding on the morphology and structural, electronic, and optical properties of $ZnWO_4$ nanocrystals. Monoclinic $ZnWO_4$ nanocrystals were prepared at three different temperatures (140, 150, and 160 °C) by a microwave hydrothermal method. Then, the samples were investigated by X-ray diffraction with Rietveld refinement analysis, field-emission scanning electron microscopy, transmission electronic microscopy, micro-Raman and Fourier transform infrared spectroscopy, ultraviolet-visible spectroscopy, and photoluminescence measurements. First-principles theoretical calculations within the framework of density functional theory were employed to provide information at the atomic level. The band structure diagram, density of states, Raman and infrared spectra were calculated to understand the effect of structural order–disorder on the properties of $ZnWO_4$. The effects of the synthesis temperature on the above properties were rationalized. The band structure revealed direct allowed transitions between the VB and CB and the experimental results in the ultraviolet-visible region were consistent with the theoretical results. Moreover, the surface calculations allowed the association of the surface energy stabilization with the temperature used in the synthesis of the $ZnWO_4$ nanocrystals. The photoluminescence properties of the $ZnWO_4$ nanocrystals prepared at 140, 150, and 160 °C were attributed to oxygen vacancies in the $[WO_6]$ and $[ZnO_6]$ clusters, causing a red shift of the spectra. The $ZnWO_4$ nanocrystals obtained at 160 °C exhibited excellent photodegradation of Rhodamine under ultraviolet light irradiation, which was found to be related to the surface energy and the types of clusters formed on the surface of the catalyst.

Received 30th October 2017,
Accepted 15th December 2017

DOI: 10.1039/c7cp07354b

rsc.li/pccp

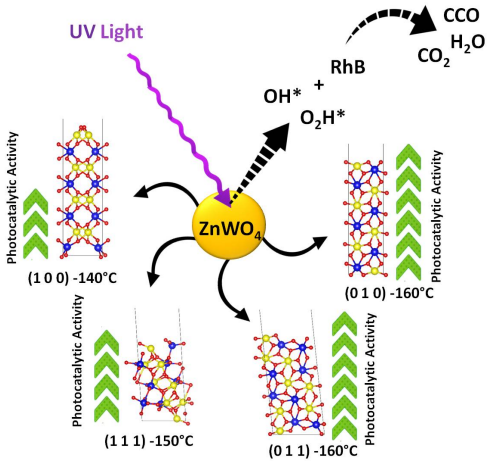

$ZnWO_4$ nanocrystals: Synthesis, morphology, and photoluminescence and photocatalytic properties

P. F. S. Pereira,[a] A. F. Gouveia,[a] M. Assis,[a] R. C. de Oliveira,[a] I. M. Pinatti,[a] M. Penha,[a] R. F. Gonçalves,[b] L. Gracia,[c] J. Andrés[d,*] and E. Longo[a]

[a]CDMF, LIEC, Chemistry Department of the Federal University of São Carlos (UFSCar), P.O. Box 676, 13565-905 São Carlos, SP, Brazil.

[b]Federal University of São Paulo (UNIFESP), 09972-270 Diadema, SP, Brazil

[c]Department of Physical Chemistry, University of Valencia (UV), Burjassot 46100, Spain.

[d]Department of Analytical and Physical Chemistry, University Jaume I (UJI), Castelló 12071, Spain.

The present joint experimental and theoretical work provides in-depth understanding on the morphology, structural, electronic, and optical properties of $ZnWO_4$ nanocrystals. Monoclinic $ZnWO_4$ nanocrystals were prepared at three different temperatures (140, 150, and 160 °C) by a microwave hydrothermal method. Then, the samples were investigated by X-ray diffraction with Rietveld refinement analysis, field-emission scanning electron microscopy, transmission electronic microscopy, micro-Raman and Fourier transform infrared spectroscopy, ultraviolet-visible spectroscopy, and photoluminescence measurements. First-principles theoretical calculations within the framework of the density functional theory were employed to provide information at the atomic level. The band structure diagram, density of states, Raman and infrared spectra were calculated to understand the effect of structural order–disorder on the properties of $ZnWO_4$. The effects of the synthesis temperature on the above properties were rationalized. The band structure revealed direct allowed transitions between the VB and CB and the experimental results in the ultraviolet-visible were consistent with the theoretical results. Moreover, the surface calculations allowed the association of the surface energy stabilization with the temperature used in the synthesis of the $ZnWO_4$ nanocrystals. The photoluminescence properties of the $ZnWO_4$ nanocrystals prepared at 140, 150, and 160 °C were attributed to oxygen vacancies in the $[WO_6]$ and $[ZnO_6]$ clusters, causing a red shift of the spectra. The $ZnWO_4$ nanocrystals obtained at 160 °C exhibited excellent photodegradation of Rhodamine under ultraviolet light irradiation, which was found to be related to the surface energy and the types of clusters formed on the surface of the catalyst.

Introduction

Water pollution by industrial effluents is a major source of concern for environmentalists worldwide.[1] The agriculture and textile industries are among the largest polluters of water globally. About 10000 tons of synthetic dyes are produced per year.[2] Inevitably, losses exist during dye manufacturing and processing operations, accounting for approximately 12% of the dye production. The effluents from these operations are usually highly colored, toxic, carcinogenic, or mutagenic waste. The color of dyes makes the effluents aesthetically unpleasant, and the dyes may also undergo degradation to form byproducts that are carcinogenic and toxic. Moreover, they also reduce the photosynthetic activity of water streams and disturb the aquatic equilibrium.[3, 4]

Many of these chemicals released by different industries cannot be removed by filtration or other simple processes. Owing to the complexity of their structure and their low biodegradability, the removal of these dyes from water poses a challenging problem.[5–7] The removal of such materials to safe levels through green routes and within reasonable costs is a current interest in pollutant management.[8–13] All these considerations have drawn attention towards the crucial need for nanomaterials for environmental remediation owing to their ability to induce photocatalytic oxidation (complete mineralization) of pollutants over their surface under UV/visible/solar light irradiation.[14–19] Nanomaterials are very promising materials as they possess high surface area, sorption sites, short intraparticle diffusion distances, and interesting surface chemistry; hence, they readily adsorb dye molecules.[20–22] Consequently, the development of semiconductor nanostructures as photocatalysts for sunlight utilization is increasingly becoming an important research topic owing to the current global energy shortage. Solar energy conversion through photocatalysis needs to maximize the utilization of visible light; dye-sensitized semiconductors have been widely studied for this purpose.[23–26]

$ZnWO_4$ is characterized by its high light yield, average refractive index, as well as X-ray absorption coefficient and short decay time, and it is considered a promising material for photocatalysts for organic pollution degradation.[27–29] In this context, vast research efforts have been dedicated in the last few years to the synthesis of $ZnWO_4$ nanostructures as promising visible light photocatalysts for organic pollutant degradation due to their high photosensitivity, excellent chemical stability, non-toxicity, several unique characteristics,[27, 28] and their potential applications in optical fibers, scintillation materials, luminescence devices, solid-state laser hosts, optical and acoustic fibers, humidity and gas sensors,[28, 30–37] electronic devices, anode materials for lithium-ion batteries,[38] stimulated Raman scattering (SRS),[39] and heavy material treatments through electro-assisted photocatalytic systems.[40]

To date, a plethora of synthetic methods have been used to obtain $ZnWO_4$ samples, such as solid-

state reactions, co-precipitation, mechanochemical, the Czochralski technique, ultrasonic irradiation, self-propagating combustion, sol–gel, hydrothermal microwave-assisted methods,[28, 31, 42–62] electrosynthesis,[29] and solvothermal synthesis.[38] However, comprehensive understanding of how different synthetic methods can affect the morphology, photoluminescence properties, as well as the photocatalytic activity (PCA) of the final materials has been rarely discussed in the literature. In this work, $ZnWO_4$ nanocrystals were synthesized by a hydrothermal microwave-assisted method as a fast, simple, and efficient method to prepare nanosized inorganic materials.[63–65] Microwave irradiation has been widely applied for the rapid synthesis of inorganic solids. Since this type of radiation affords internal heating of the material, lower temperatures and shorter times can be used compared to those applying conventional heating.[66–68] Microwave heating is an inexpensive, facile, and relatively fast method for the preparation of nanocrystalline samples with unique or enhanced properties.

Inspired by the above considerations, in this paper we report the synthesis of $ZnWO_4$ nanocrystals via a microwave hydrothermal (MH) method at three different temperatures (140, 150, and 160 °C). Our principal aim was to understand the fine effects of the synthesis temperature on the morphology and photoluminescence properties of the as-synthesized $ZnWO_4$ nanocrystals and to investigate the role of the electronic structure on their photocatalytic activity. Herein, we clarify these points by performing a detailed theoretical and experimental study on the PCA of $ZnWO_4$ nanocrystals. The evaluation was carried out by decomposing rhodamine B (RhB) under visible irradiation. The synthesized materials were characterized by X-ray diffraction (XRD) with Rietveld refinement, field-emission scanning electron microscopy (FE-SEM), transmission electronic microscopy (TEM and HR-TEM), and micro-Raman (MR) and Fourier transform infrared (FT-IR) spectroscopy. Moreover, their optical properties were investigated by ultraviolet-visible (UV-vis) spectroscopy and photoluminescence (PL) measurements at room temperature. First-principles theoretical calculations within the framework of the density functional theory (DFT) were employed to obtain information at the atomic level. The band structure diagram, density of states (DOS), and Raman and Infrared spectra were calculated to understand the effects of structural order-disorder on the properties of $ZnWO_4$.

Experimental and Theoretical Methods

Synthesis of $ZnWO_4$ nanocrystals. The $ZnWO_4$ nanocrystals were prepared by the MH method at 140, 150 and 160 ^oC for 1 hour. The corresponding procedure is described below: 2 x 10^{-3} mol of tungstate (VI) sodium dihydradrate ($Na_2WO_4.2H_2O$; 99.5% purity, Sigma-Aldrich) and 2 x 10^{-3} mol of zinc nitrate ($Zn(NO_3)_2$; 99.9% purity, Sigma-Aldrich) were dissolved separately in 50 mL of deionised water at room temperature in beaker under magnetic stirring. The solution with Zn^{2+} and NO_3^- was added to the glass beaker of solution containing the WO_4^{2-} ions and this solution remained at room temperature under magnetic stirring for some minutes until complete precipitation. Thus, a white suspension appeared and 100 mL of these solutions were inverted into a Teflon autoclave vessel without magnetic stirring. This suspension was processed at 140, 150 and 160 ^oC for 1 hour. The resulting suspensions were washed several times with deionized water to remove the residual Na^+ ions. The crystalline $ZnWO_4$ nanocrystals were collected and dried in an oven at 70 ^oC for some hours. Previously, Tan and co-workers[59] investigated the formation of $ZnWO_4$ phase by microwave-assisted hydrothermal synthesis and only obtained the pure phase at 220 °C for 1 h. In the present study, we also obtain pure phase at lower temperatures.

Characterization. The $ZnWO_4$ nanocrystals were structurally characterized by XRD patterns using a D/Max-2000PC diffractometer Rigaku (Japan) with Cu Ka radiation (λ = 1.5406 Å) in the 2θ range from 10° to 70° in the normal routine with a scanning velocity of 2°/min and from 10° to 110° with a scanning velocity of 1°/min in the Rietveld routine. MR spectroscopy was conducted on a Horiba Jobin-Yvon (Japan) spectromoter charge-coupled device detector and argon-ion laser (Melles Griot, United States) operating at 514.5 nm with maximum power of 200 mW. The spectra were measured in the range 200-1000 cm^{-1}. FT-IR spectroscopy was recorded in the range from 200 to 1000 cm^{-1} using KBr pellets as a reference in a Bomem Michelson spectrophotometer in transmittance mode (model MB102). The shapes and sizes of these $ZnWO_4$ nanocrystals were observed with a field-emission scanning electron microscope model FE-SEM Inspect F50 (FEI Company, Hillsboro, OR) operated at 5 kV. The TEM analysis was performed using JEM 2100F TEM/STEM microscope operating at 200 kV. The optical properties of the $ZnWO_4$ nanocrystals were analyzed by UV-Vis and PL spectroscopies. UV-vis spectra were taken using a (Varian, USA) spectrophotometer (model Cary 5G) in a

diffuse-reflectance mode. PL measurements were performed through a Monospec 27 monochromator (Thermal Jarrel Ash) coupled to a R446 photomultiplier (Hamamatsu Photonics, Japan). A krypton-ion laser (Coherent Innova 90K; λ = 350.7 nm) was used as the excitation source; its maximum output power was maintained at 500 mW. The laser beam was passed through an optical chopper, and its maximum power on the sample was maintained at 40 mW. PL measurements were performed at room temperature.

Photocatalytic tests of $ZnWO_4$. Photocatalytic activities (PCA) of the prepared $ZnWO_4$ nanocrystals were evaluated by photocatalytic degradation of 100 mL of the Rhodamine B (RhB) in aqueous solution under UV light. In a typical process, 50 mg $ZnWO_4$ nanocrystals synthesized by MH method at 140, 150 and 160 ^{o}C for 1 hour were dispersed in 50 mL of the RhB solution (1 x 10^{-5} mol). The above mixture was transferred into a 100 mL Pyrex glass bottle and stirred for 30 min to make the catalyst blend evenly in the solution. The suspensions were irradiated by six lamps (PHILIPS TL-D, 15 W). After the reaction, the mixture was centrifuged at 13.000 rpm for 10 min to completely remove the catalyst particles. The remaining solution was analyzed with by UV-Vis absorption spectroscopy on a V-660 spectrophotometer (JASCO). Variations in the absorption band (maximum λ = 554 nm) were monitored.

Computational Method. Theoretical calculations for $ZnWO_4$ were performed using DFT as implemented in the VASP program.[69, 70] The Kohn-Sham equations were solved using the functional proposed by Perdew, Purke, and Ernzerhof (PBE),[71] and the electron-ion interaction was described using projector augmented wave pseudopotentials.[69, 72] The plane-wave expansion was truncated at a cutoff energy of 460 eV, and the Brillouin zones were sampled through 6 × 6 × 1 Monkhorst−Pack special k-points grids that ensure geometrical and energetic convergence for the $ZnWO_4$ structure. A vacuum spacing of 15 Å was introduced in the z-direction such that the surfaces did not interact with each other. Each surface was modeled using stoichiometric systems. The surface energy (E_{surf}) was defined as:

$$E_{surf} = \frac{E_{slab} - nE_{bulk}}{2A} \quad (1)$$

where E_{slab} is the total energy per repeating cell of the slab, E_{bulk} is the total energy of the perfect crystal per molecular unit, n is the number of molecular units of the surface, and A is the surface area per repeating cell of the 2 sides of the slab. The procedure to obtain the complete set of morphologies, based on the Wulff construction and the surface energy, has been previously presented by Andrés et al.[73]

The screened hybrid functional HSE06 was used in order to obtain the band structure diagram, the density of states (DOS) as well as Raman/IR vibrational modes using numerical second derivatives of the total energies.

Results and discussion

XRD analysis. The XRD technique allows ascertaining the degree of structural order–disorder at long-range distances or the periodicity of $ZnWO_4$ nanocrystals. Fig. 1 (a–c) shows the influence of the reaction temperature on ZnWO4 nanocrystals synthesized at 140, 150, and 160 °C for 1 h via an MH method. Fig. 1 (a–c) shows that the diffraction peaks for all $ZnWO_4$ nanocrystals can be successfully indexed to the pure monoclinic sanmartinite phase[74, 75] with a wolframite structure and a space group of $P2/c$[41, 46, 74–76] with C_{2h}^4 symmetry[52, 77] and two molecules per unit cell (Z = 2).

These crystals present sharp and well-defined diffraction peaks, indicating a good degree of structural order at long-range distances.[61, 78–82] The strong diffraction peaks for the (111) plane observed in Fig. 1 (a–c) suggest that all the prepared $ZnWO_4$ samples are highly crystalline.[74] All diffraction peaks are consistent with the Inorganic Crystal Structure Database (ICSD) pattern No. 84540.[83] As can be observed from Fig. 1, the intensity of the diffraction peaks increased with the increasing temperature, from 140 to 160 °C during the MH procedure. This behavior confirms structural organization at long distances and indicates the high crystallinity of the materials. In addition, the diffraction peaks were slightly shifted to higher 2θ values with the increasing synthesis temperature, consequently resulting in smaller interplanar distances and causing a slight reduction of the unit cell volume.

The average crystallite size was estimated by Scherrer's equation using the full width at half maximum (FWHM) of the most intense peak of the (111) plane. As reported in the literature,[74] Scherrer's equation (Equation (2)) is described as follows:

$$D = \frac{0.9\lambda}{B\cos\theta} \quad (2)$$

where D is the average crystallite size, λ is the X-ray wavelength (0.15406 nm), θ is the Bragg angle, and B is the FWHM.[74, 84] As observed, the average crystallite size for the $ZnWO_4$ samples increased slightly with the increasing temperature, from 11.7 to 13.9 nm for the $ZnWO_4$ nanocrystals prepared by the MH method.

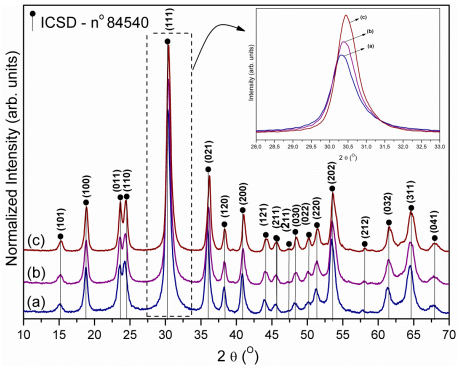

FIGURE 1 – XRD of the $ZnWO_4$ nanoparticles obtained by the MH method at: (a) 140, (b) 150, and (c) 160 °C.

Rietveld refinement analysis. Fig. ESI-1 (Electronic Supplementary Information) shows the Rietveld refinement plot for the $ZnWO_4$ nanocrystals prepared by the MH method at 140, 150, and 160 °C for 1 h.

Structural analysis via Rietveld refinement[85] was employed to confirm the wolframite structure of the $ZnWO_4$ nanocrystals. Such a structural refinement was performed using the general structure analysis (GSAS) program.[86] The calculated patterns were adjusted to fit the observed patterns and thus provide the structural parameters of the material and the diffraction profile. As such, the experimental lattice parameters, unit cell volume, and atomic positions of the $ZnWO_4$ nanocrystals were calculated using the Rietveld refinement method. The refined parameters were discussed in a previous work.[87]

The analysis of Fig. ESI-1 (a–c) shows good agreement between the observed XRD patterns and the theoretical fit, indicating the successful application of the Rietveld refinement method. Therefore, all the structural refinement results obtained using this method[85] were consistent with the ICSD Nº 84540 pattern, confirming the presence of a single phase in all the $ZnWO_4$ nanocrystals corresponding to a wolframite structure with a symmetry space group *P*2/*c* and two molecules per unit cell (*Z* = 2). These results confirmed the effectiveness of our synthetic method.

The success of the Rietveld refinement method was verified by the small differences (nearly zero) in the intensity scale, as illustrated by the line Y_{Obs} - Y_{Calc}. The experimental and calculated data from the DFT and Rietveld refinement methods are summarized in Table 1, including the lattice parameters, cell volume, and statistical parameters (R_{Bragg}, χ^2, R_{wp}, and R_p). The statistical *R*-values presented in this table suggest that the refinement results are reliable.

From the results reported in Table 1, it is possible to verify slight variations in the lattice parameters and cell volume values (all consistent with the ICSD card Nº 84540). These results indicate that the octahedral [ZnO_6] and [WO_6] clusters (the building blocks of the structure) are distorted, thus generating structural defects in the $ZnWO_4$ lattice.

Table 2 shows the atomic coordinates for the Zn, W, and O atoms obtained from the Rietveld refinement. Upon analyzing these data, it is possible to note a considerable variation in the atomic positions of the oxygen atoms, as these atoms do not occupy fixed positions in such a structure, while the Zn and W cations practically maintain their positions fixed throughout the structure. Fig. 2 illustrates the unit cell of $ZnWO_4$ prepared by the MH method at 160 °C for 1 h with a *P*2/*c* space group and C_{2h}^4 point-group symmetry,[88, 89] and also the experimental and calculated clusters present in the $ZnWO_4$ wolframite, modeled using the Visualization for Electronic and Structural Analysis (VESTA) program.[90]

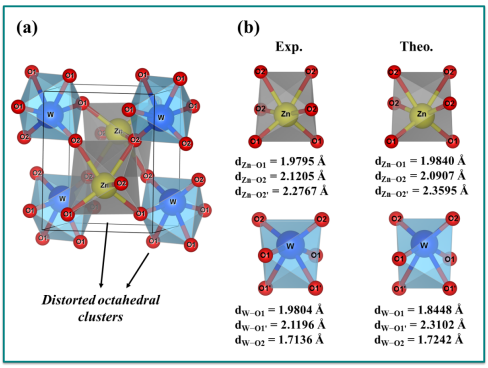

FIGURE 2 – (a) Unit cell of $ZnWO_4$, and (b) bond distances of theoretical calculations and experimental results for the [ZnO_6] and [WO_6] clusters.

The structural parameters and atomic coordinates obtained from the Rietveld refinement were employed to model the unit cell of $ZnWO_4$, whose values are listed in Tables 1 and 2.

Analysis of the results reported in Tables 1 and 2 confirmed that the $ZnWO_4$ lattice is composed of Zn and W cations coordinated with six oxygen atoms forming distorted [ZnO_6] and [WO_6] clusters (6 vertices and faces, respectively, and 12 edges) in an octahedral configuration. These results are consistent with those reported in the literature.[88, 89, 91] Therefore, both crystals have clusters of the symmetry group O_h with octahedral symmetry sites (C_2). In the monoclinic $ZnWO_4$ structure, there are distorted [ZnO_6] and [WO_6] clusters with three pairs of different lengths for both Zn−O and W−O bonds (see Fig. 2 (b)). There are two types of O anions in the [WO_6] clusters: four O1 and two O2; while there are two positions for O1 and four positions for O2 in the [ZnO_6] clusters.[91–93]

Micro-Raman spectroscopy analysis. Fig. 3 (a) displays the MR spectra of $ZnWO_4$ nanocrystals synthesized by the MH method at 140, 150, and 160 °C for 1 h. A comparison of the experimental and calculated Raman vibrational modes of $ZnWO_4$ nanocrystals is presented in Fig. 3 (b), and their values are listed in Table ESI-1 in comparison with relevant data from the literature.[94, 95]

As shown in Table ESI-1, both experimental and theoretical results are in good agreement with the results found in the literature. The slight variations in the positions of the typical vibrational modes of our samples relative to those reported in the literature can be attributed to the different syntheses, crystal sizes, distortions on the bonds and angles of the [O–Zn–O]/[O–W–O] moieties at short-range distances, and/or intermolecular forces between the $[ZnO_6]$–$[WO_6]$ clusters.[89]

The $ZnWO_4$ nanocrystals present a wolframite structure within the monoclinic space group $P2/c$[96] and 36 lattice modes in accordance with group theory calculations; however, only 18 vibrational modes (8Ag + 10Bg) are Raman active.[97] These vibrational modes are classified in two types: internal and external modes. The internal vibrational modes are assigned to distorted octahedral $[WO_6]$ clusters, while the external vibrational modes are associated with the distorted octahedral $[ZnO_6]$ clusters in the lattice.[89, 98]

The phonon frequencies of the internal vibration modes associated with the W–O bonds of $[WO_6]$ are higher than those of the external modes associated with Zn–O bonds. This occurs because the internal covalent bonding in the $[WO_6]$ octahedrons is stronger than the external lattice binding in $[ZnO_6]$.[98, 99] In general, internal vibrations are expected to occur at higher wavenumbers than external vibrations;[99] this behavior arises from the strong covalent nature of the W–O bonds.

TABLE 1 – Lattice parameters, unit cell volume and statistical parameters of quality obtained by Rietveld refinement for the $ZnWO_4$ nanoparticles synthesized by MH method at 140, 150 and 160 °C for 1 hour.

$ZnWO_4$	Lattice Parameters				Cell volume	R_{Bragg} (%)	χ^2 (%)	R_{wp} (%)	R_p (%)
	a (Å)	b (Å)	c (Å)	β	(Å^3)				
140 °C	4.6883(7)	5.7600(8)	4.9732(6)	90.498	134.30(1)	1.25	1.79	6.69	5.05
150 °C	4.6868(1)	5.7545(7)	4.9568(3)	90.566	133.68(2)	1.11	1.50	5.61	4.14
160 °C	4.6861(2)	5.7500(5)	4.99495(6)	90.582	133.36(2)	1.30	1.49	5.63	4.12
Theo.	4.6823	5.8076	4.8214	89.979	131.108	-	-	-	-
ICSD N° 84540	4.6926(3)	5.7212(9)	4.9280(5)	-	132.3	-	-	-	-

TABLE 2 – Atomic coordinates of the $ZnWO_4$ nanoparticles synthesized by MH method at 140, 150, and 160 °C for 1 hour.

Atoms	$ZnWO_4$								
	140 °C			150 °C			160 °C		
	x	y	z	x	y	z	x	y	z
Zn	0.5000	0.6833	0.2500	0.5000	0.6833	0.2500	0.5000	0.6833	0.2500
W	0.0000	0.1823	0.2500	0.0000	0.1823	0.2500	0.0000	0.1823	0.2500
O1	0.2601	0.3540	0.3852	0.2582	0.3599	0.3940	0.2536	0.3650	0.3938
O2	0.2224	0.8723	0.4207	0.2206	0.8782	0.4295	0.2160	0.8833	0.4293

Analysis of Fig. 3 (a) revealed the presence of 18 well-defined Raman active vibrational modes between 50 and 1000 cm^{-1}. Higher symmetric and anti-symmetric stretching modes are associated with internal vibrations inside the $[WO_6]$ clusters, showing several peaks corresponding to Raman-active internal A_g and B_g modes with their vibrations composed of six internal modes (four A_g and two B_g).[89, 99]

The main mode (A_g) is associated to the intense peak located at around 903.3 cm^{-1} ascribed to the symmetric stretching of (←O←W→O→), see inset in Fig. 3 (a). The Raman B_g and A_g modes at 781.6 and 705.2 cm^{-1}, respectively, are assigned to asymmetric stretching of (→O→W→O→), see inset in Fig. 3 (a).[89, 99] The Raman A_g and B_g modes at 672.9 (B_g), 543.8 (A_g), 513.0 (B_g), and 403.5 (A_g) cm^{-1} are attributed to stretching modes of the long W–O bonds. The Raman modes of low intensity at around 120.1 (A_g), 145.7 (B_g), 161.5 (B_g), 188.5 (B_g), and 194.1 (A_g) are assigned to the symmetric stretch of (←O←Zn→O→) bonds, while the modes at 309.9 (B_g), 269.9 (A_g), and 277.3 (A_g) are attributed to the vibrations of cationic sublattices (see inset in Fig. 3 (a)).[76, 89, 99–101] Therefore, all the vibration modes presented in Fig. 3 (a) are intense and well-defined, suggesting that the $ZnWO_4$ nanocrystals are structurally ordered in the short range and correspond to a wolframite-type monoclinic structure.

Table ESI-2 shows the FWHM, and the Raman peak position and intensity for the $ZnWO_4$

nanocrystals. The linewidth of the main mode (A_g) for the intense peak located at around 903.3 cm^{-1} was obtained by assuming a deconvolution of Lorentzian curves. Table ESI-2 illustrates the temperature dependence of the linewidth, showing narrow and more intense peaks and a moderate wavenumber shift is also observed with the increasing temperature. This reveals a temperature dependence of the structural order in the short range. These results corroborate the XRD and Rietveld refinement data.

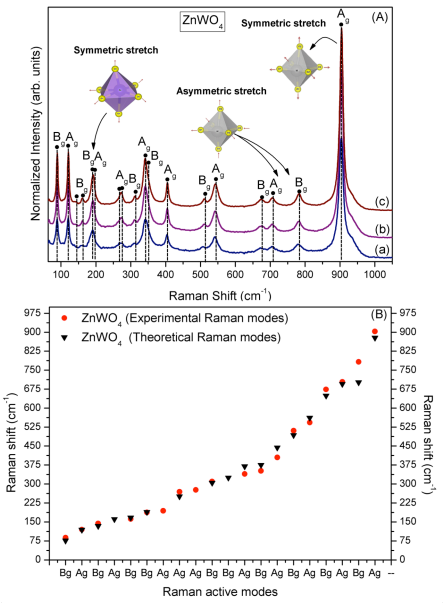

FIGURE 3 – (A) Raman spectra of the $ZnWO_4$ nanocrystals obtained by the MH method at (a) 140, (b) 150 and (c) 160 °C for 1 h. (B) Comparative between the relative positions of theoretical and experimental Raman-active modes of $ZnWO_4$ nanocrystals.

FT-IR spectroscopy analysis. Molybdate and tungstate crystals with a wolframite-type monoclinic structure exhibit 36 different vibrational modes according to group theory calculations. Among these vibrational modes, 18 modes ($8A_u$ and $10B_u$) are expected to appear in the infrared spectra; however, three modes ($1A_u$ and $2B_u$) correspond to acoustic vibrations and thus, only 15 modes ($7A_u$ and $8B_u$) are IR active.[76, 89]

In this work, IR spectroscopy was used in transmittance mode to characterize the structure in the metal–oxygen bond region. The stretching absorption bands (symmetric, asymmetric, and anti-symmetric) associated with metal–oxygen bonds can be observed between 200 and 1000 cm^{-1}.

Fig. 4 (A and B) shows the normalized FT-IR spectra of the experimental and theoretical infrared modes of the $ZnWO_4$ nanocrystals prepared at 140, 150, and 160 °C, respectively. Fig. 4 (a) displays 10 IR active vibrational modes. The B_u mode at around 256 cm^{-1} is attributed to the asymmetric stretching of bonds in the $[ZnO_6]$–$[ZnO_6]$ clusters. The A_u mode at 321 and 368 cm^{-1} are assigned to the symmetric stretch (O←Zn←O→Zn→O) of distorted octahedral $[ZnO_6]$–$[ZnO_6]$ clusters, and the A_u mode at around 428 cm^{-1} is ascribed to the asymmetric stretch (O→Zn→O→Zn→O) of the distorted octahedral $[ZnO_6]$ clusters.

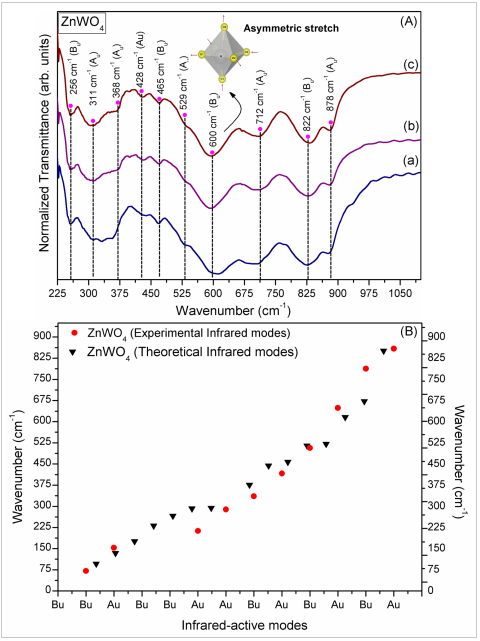

FIGURE 4 – (A) FT-IR spectra of the $ZnWO_4$ nanocrystals obtained by the MH method at (a) 140, (b) 150 and (c) 160 °C for 1 h. (B). Comparative between the relative positions of theoretical and experimental FT-IR modes of $ZnWO_4$ nanocrystals.

The B_u and A_u modes at approximately 465 and 529 cm^{-1} are associated with asymmetric stretching (O←W←O←W←O) of distorted octahedral $[WO_6]$–$[WO_6]$ clusters.

The broad absorption band at 600 cm^{-1} corresponds to a B_u mode attributed to asymmetrical vibrations of the bridging oxygen atoms of the O–W–O groups of distorted octahedral $[WO_6]$ clusters (see inset in Fig. 4 (a)).

The absorption band at around 712 cm^{-1} is assigned to the A_u mode and the absorption bands at around 822 and 878 cm^{-1} are related to B_u and A_u modes, respectively, which are assigned to the symmetric stretching (←O←W→O→) of distorted octahedral $[WO_6]$ clusters.[46, 47, 76, 89, 100, 102] The FT-IR results confirm the formation of $ZnWO_4$ nanocrystals in all the samples.[100]

Fig. 4 (b) shows the theoretical and experimental positions of the FT-IR active modes and their values are listed in Table ESI-3, as well as values reported in the literature.[103, 104] Analysis of the results revealed good agreement between the wavenumbers of the FT-

IR modes of the experimental and theoretical calculations; however, the theoretical results illustrated more B_u and A_u modes at 96, 134, 176, and 231 cm^{-1}, which were not experimentally detected due to the low detection limit of the FT-IR spectrophotometer used. In addition, Table ESI-3 shows that both experimental and theoretical results are in good agreement with the results found in the literature. The same conclusion was reached for the FT-IR and Raman modes, in which a small variation in the positions of FT-IR active modes of $ZnWO_4$ nanocrystals was observed. This behavior is probably due to variations in the bonds lengths and angles of the O–Zn–O, O–W–O, and Zn–O–W moieties.[89]

FE-SEM, TEM, and HRTEM images and Wulff construction analysis. The detailed morphology of the materials was examined by FE-SEM, TEM, and HR-TEM. As shown in Fig. 5, different morphologies were obtained upon changing the synthesis temperature.

Fig. 5 (a–c) shows the FE-SEM images, where the presence of $ZnWO_4$ nanocrystals of agglomerated nature can be discerned in all samples. However, it was not possible to correctly define the shape and size of the nanocrystals. Thus, the TEM technique was used to better define the morphological characteristics of the nanostructures and the surface morphology of the $ZnWO_4$ nanocrystals, as well as to confirm the wolframite monoclinic structure.

Fig. 6 (a, e, i, and m) shows the TEM images of the $ZnWO_4$ nanocrystals as function of the temperature. An analysis of these images point out that the temperature has a large effect on the morphology and size of ZnWO4 nanocrystals. At 140 °C, the nanocrystals exhibit undefined morphology (see Fig. 6 (a)). However, deformed polyhedrons were observed when the temperature was increased to 150 °C, revealing the formation of nanorods of rectangular form with different sizes (see Fig. 6 (e)). At 160 °C, $ZnWO_4$ nanocrystals were obtained as fully defined polyhedral (e.g., nanorods), rectangular, and hexagonal plates (see Fig. 6 (i), (m)).

The crystalline planes and morphologies are also shown in Fig. 6 (b, c, f, g, j, k, n, and o). These images confirm the high crystallinity of the materials and prove that these nanocrystals have the monoclinic structure of wolframite.

Growth is observed in the (100) direction for the sample processed at 140 °C, in the (111) direction for the sample prepared at 150 °C, and growth of the sample synthesized at 160 °C occurs in the (011) and (010) faces.

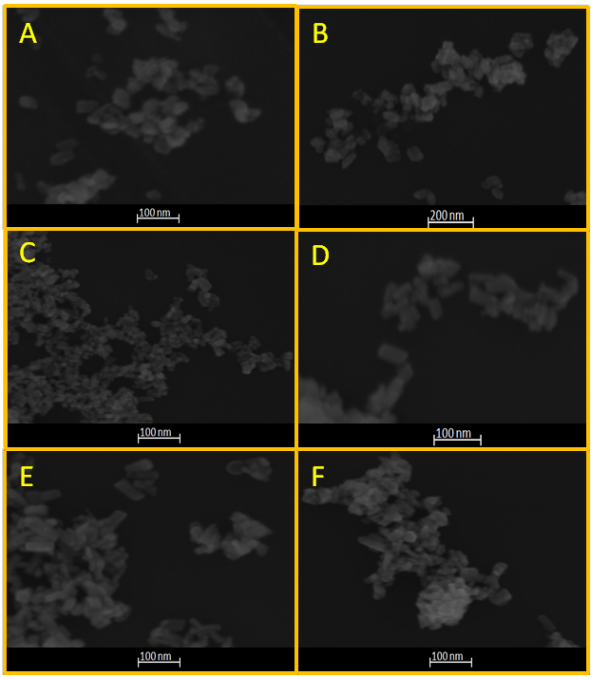

FIGURE 5 – FE-SEM images of $ZnWO_4$ nanocrystals, obtained by the MH method at (A, B) 140, (C, D) 150 and (E, F) 160 °C for 1 h.

Therefore, it is possible to conclude that these nanocrystals do not present a predominant growth mechanism; however, the increase in the temperature changes the growth process from the (100) and (111) directions to the (010) and (011) ones. Both (010) and (011) surfaces present lower E_{surf} values than the (100) and (111) surfaces, as demonstrated below by theoretical calculations.

The size distributions are shown in Fig. ESI-2, and analysis of the results indicates that the length and thickness of the samples increase with the temperature.

Table ESI-4 lists the corresponding surface energy (E_{surf}) values calculated using the DFT method for the low-index facets of $ZnWO_4$. The stability order of the surfaces is (010), 0.26 eV < (110), 0.54 eV < (011), 0.58 eV < (001), 0.84 eV < (111), 1.23 eV < (101), 1.43 eV < (100), 2.63 eV. The (010), (011), (001), and (100) surfaces are ZnO-terminated, while the (110), (111), and (101) surfaces are WO-terminated. It is worth noting that there are different types of $[ZnO_x]$ and $[WO_x]$ clusters at the top (first layer) of theses surfaces in the presence of oxygen vacancies, V_O^x, and also in the second layer for the (110), (011), (001), (111), and (101) surfaces. Fig. 7 depicts the surface representation of the $ZnWO_4$ structure used in the calculations.

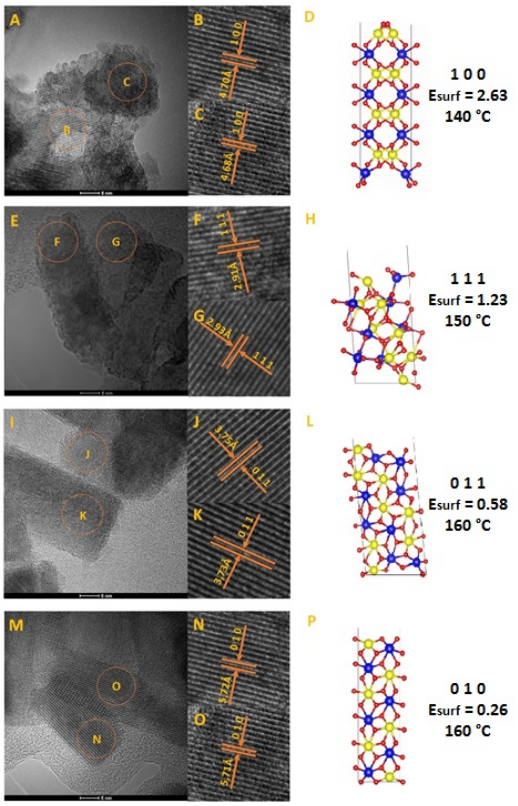

FIGURE 6 – TEM images of $ZnWO_4$ nanocrystals obtained by the MH method at 140 °C (A), 150 °C (E) and 160 °C (I, and M) for 1 h; HR-TEM images of $ZnWO_4$ nanocrystals prepared at 140 °C (B, C), 150 °C (F, G) and 160 °C (J, K and N, O); Surface models involves in each morphology of the $ZnWO_4$ nanocrystals, (D) (100) surface for 140 °C, (H) (111) surface for 150 °C and (L, P) ((011), (010), respectively) surfaces for 160 °C. Surface energy (E_{surf}) in eV.

Based on the E_{surf} values for all the facets and the Wulff construction implemented in the VESTA program,[90] it was possible to determine the crystal shape of the $ZnWO_4$ nanocrystals in vacuum. The present equilibrium morphology was derived from the calculated E_{surf} values under the assumption that the crystal faces with the lowest surface energies control the crystal morphology, as illustrated in Fig. 8.

The ideal morphology of $ZnWO_4$ is depicted in the center of Fig. 8, where a map of the available morphologies of $ZnWO_4$ is also presented. Different crystal morphologies can be achieved by tuning the surface energy values of some facets using the Wulff construction method.[73, 105, 106] Based on these results, it is possible to modulate the morphology, which is dependent on the relative values of the surface energy as well as the percentage of the area in the structure.[73, 105, 106] Thus, the material properties are linked with the type of clusters in the surface.

In the case of $ZnWO_4$ nanocrystals, it is not possible to associate the FE-SEM images to the Wulff construction. However, we can associate the surface energy stabilization with the temperature. At 140 °C, the only surface found is the interplanar distal 4.69 Å, corresponding to the (100) plane; at 150 °C, the interplanar distance of 2.93 Å corresponds to the (111) plane; while, at 160 °C, the 5.72 and 3.73 Å distances correspond to the (010) and (011) surfaces, respectively. The surface energy decreases as follows: $E_{surf}^{(100)}$ = 2.63 > $E_{surf}^{(111)}$ = 1.23 > $E_{surf}^{(011)}$ = 0.58 > $E_{surf}^{(010)}$ = 0.26, as shown in Fig. 8. Thus, the increasing temperature enhances the growth path in the direction of surfaces with lower energy values.

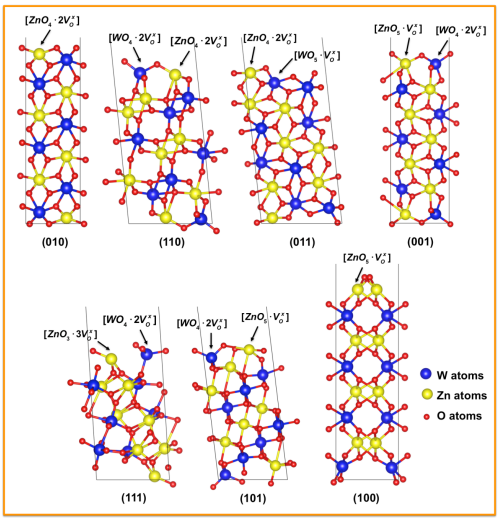

FIGURE 7 – Surface representation of the $ZnWO_4$ structure.

UV-vis absorption spectroscopy analysis. The optical band gap energy (E_{gap}) of the $ZnWO_4$ nanocrystals was calculated by the Wood–Tauc[107] method and the Kubelka–Munk[108] function. This methodology is based on the transformation of diffuse reflectance measurements to estimate the E_{gap} values with high accuracy within the limits of certain assumptions when modeled in three dimensions. Assuming that $ZnWO_4$ presents direct transitions between the valence (VB) and conduction (CB) bands,[74, 89, 109-111] the E_{gap} values for all the samples were calculated using n = 1.[112, 113] The E_{gap} was obtained by extrapolating the linear portion of the $(\alpha h\upsilon)^2$ versus $h\upsilon$ plots of the UV-vis curves, according to $[\alpha h\upsilon = A(h\upsilon - E_{gap})^{n/2}]$[112, 113] equation, where α is the absorption coefficient and $h\upsilon$ is the photon energy.[74, 89, 112, 113]

Fig. ESI-3 shows the UV-vis spectra for the $ZnWO_4$ nanocrystals obtained by the MH method at 140, 150, and 160 °C and the corresponding E_{gap} values are listed in Table 3.

Table 3 illustrates the experimental E_{gap} values, showing a slight decrease in the values with the increasing temperature, showing a red shift of the absorption band edge.[74, 114] The relatively low E_{gap} value obtained for $ZnWO_4$ indicates a large number of

structural defects generating allowed states between the VB and CB. The increase of the E_{gap} values is linked to a reduction of the intermediary energy levels between the VB and CB by reducing the number of defects in local lattice distortions,[89] since the optical band gap energy is controlled by the degree of structural order-disorder in the lattice.[78]

The study of the electronic levels in these nanocrystals can be achieved by theoretical calculations. The band structure of $ZnWO_4$ is presented in Fig. 9 (A), which shows a direct band gap value of 3.85 eV located at the Y point of the Brillouin zone. This value is consistent with the experimental band gap value.

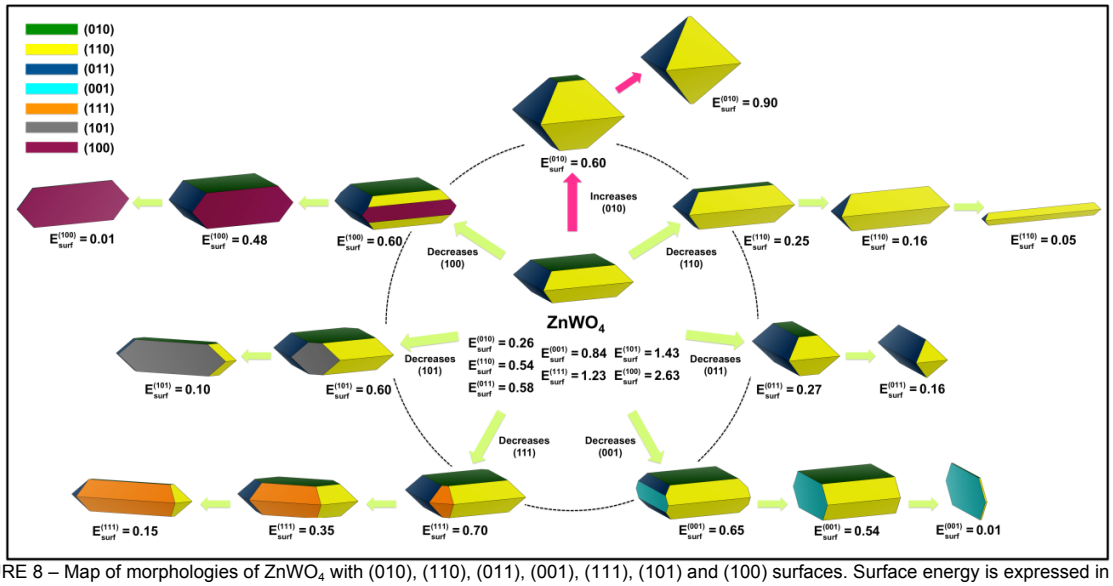

FIGURE 8 – Map of morphologies of $ZnWO_4$ with (010), (110), (011), (001), (111), (101) and (100) surfaces. Surface energy is expressed in J m^{-2}.

TABLE 3 – Optical band gap energy (E_{gap}) values to $ZnWO_4$ nanoparticles obtained by MH method at 140, 150, and 160 °C for 1 hour.

$ZnWO_4$	E_{gap} (eV)
140 °C	3.96
150 °C	3.97
160 °C	3.87

Generally, a reduction of E_{gap} can be achieved by temperature effects, by changing the synthetic method (thin films or powders), by introducing impurities in the lattice, by disordering the structure due to structural defects in the medium range, by local bond distortions [78, 115] in the $[WO_6]$–$[WO_6]$, $[ZnO_6]$–$[ZnO_6]$, or $[WO_6]$–$[ZnO_6]$ clusters, by tuning the particle shape, size, intrinsic surface states and interfaces, etc.[49] Thus, these factors can be directly associated with these electronic properties.

Fig. 9 (B) shows the partial DOS projected on the Zn, W, and O atoms and the total DOS projected over all atoms in the $ZnWO_4$ structure.

The analysis of the total DOS shows that the VB is predominantly composed of O atoms, while the partial DOS reports that this band is mainly formed by p-type orbitals ($2p_x + 2p_y + 2p_z$ and $3p_x + 3p_y + 3p_z$), of which a small portion are bonding orbitals for both Zn and W atoms. Most of these p-type orbitals are anti-bonding orbitals and the electrons present in theses anti-bonding orbitals result in polarization of both $[ZnO_6]$ and $[WO_6]$ clusters. Also, a minor contribution of 3d and 4d orbitals is observed from Zn and W atoms, respectively. The CB is mainly formed by W atoms with a minor contribution of O 2p atoms. The partial DOS shows that the W orbitals are $4d_{xz} + 4d_{yz} + 4d_{xy}$ and $4d_z^2 + 4d_{x^2-y^2}$, with higher contributions from the latter. The orbitals in the CB are mainly bonding orbitals, constituted by the hybridization of O 2p and W 4d orbitals.

This fact ensures that distortions in the $[WO_6]$ clusters generate intermediary levels in the forbidden zone between the VB and CB, narrowing the band gap. Distortions in the $[ZnO_6]$ clusters can also contribute by creating intermediate levels, although at a smaller scale.

Photoluminescence. PL is a physical process involving the electronic structure of the sample at a medium range, which can be used to determine the defect density of $ZnWO_4$ samples.[80] Fig. 10 shows the PL spectra of the $ZnWO_4$ nanocrystals prepared by the MH method at 140, 150, and 160 °C under 350.7 nm excitation.

Fig. 10 shows the PL emission from 350 to 800 nm for all the samples, where broad band profiles can

be observed, covering all the visible spectrum with a maximum emission in the blue-green region at 515 nm.

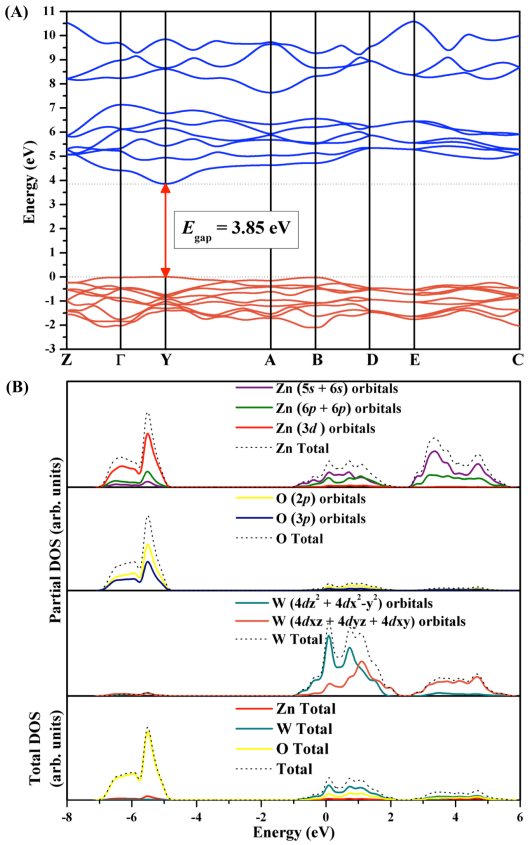

FIGURE 9 – (A) Band structure of $ZnWO_4$ model. (B) Density of states projected in $ZnWO_4$ structure.

The profile of the emission band is typical of a multiphonon process, where relaxation occurs by several paths involving several energy states within the band gap.[116–118]

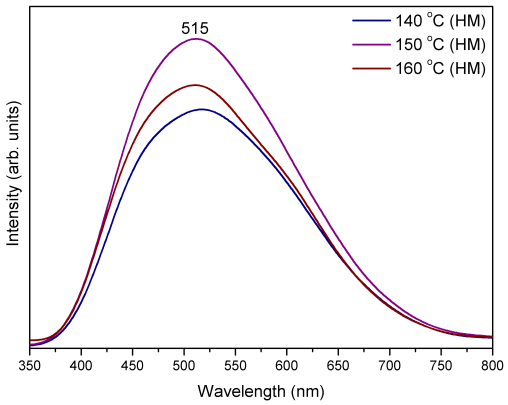

FIGURE 10 – Emission spectra of the $ZnWO_4$ nanocrystals obtained by the MH method at 140, 150 and 160 °C for 1 h; excited at 350.7 nm with a krypton ion laser.

According to the literature,[41, 52, 74, 119, 120] the blue-green emission of $ZnWO_4$ is linked to the intrinsic emission of WO_6^{6-} complexes, where WO_6^{6-} octahedra act as luminescence centers in the matrix and the charge transfer occurs between the O 2p orbitals and empty 4d W orbitals. On the other hand, the yellow-red emission has been found to be extrinsic and may be a defect-related emission.[121] Consequently, this is linked to oxygen vacancies which are key in the formation of luminescence centers.

Previously, some of us[118] have reported that the PL properties are directly connected to the structural order–disorder of the lattice, indicating that the intensity increase of the PL emission requires some simultaneous order–disorder in the system and that totally disordered or highly crystalline structures afford reduced PL emission.

Fig. 10 shows the temperature dependence of the PL emission, in which an increase of the luminescence intensity is observed for the samples prepared at 140 and 150 °C. For the sample synthesized at 160 °C, the opposite behavior is observed, that is, a reduction of the PL emission. These results are consistent with the XRD data and the literature data.[118] However, the UV-vis analysis and PL experimental measurements indicate that significant changes in the band gap states occur when the system becomes more ordered (see Table 3 and Fig. 10).

The phenomenon of reduced luminescence intensity can be attributed to an increase in the number of superficial defects and non-radiative electron–hole recombination rates, consequently leading to the appearance of intermediate levels between the VB and CB.[52] Moreover, a variety of factors can influence the luminescence intensity and appearance of intermediate levels within the forbidden band, such as the morphology, particle size, synthesis method, calcination temperature,[52] and number of oxygen vacancies,[122] among other.

After analyzing our experimental results, we concluded that the PL emission behavior is directly associated to structural defects (oxygen vacancies), as confirmed by the XRD and MR analyses (see Fig. 1 and Table SI2, respectively). Thus, the oxygen vacancies induce luminescence quenching, and this fact is explained due to the increase in the concentration of defects causing lattice distortions and facilitating the expansion of the phonon spectrum, thereby increasing the non-radiative recombination due to electron–phonon interactions.[120, 122]

For better understanding of the PL properties and temperature dependence in the $ZnWO_4$ lattice, the PL spectrum peak were deconvoluted using the PickFit program with the Voigt area function, as shown in Fig. ESI-4.

Fig. ESI-4 (A) shows the deconvolution of the PL spectra, which exhibit three curves in the blue (maximum at λ = 448 nm), green (maximum at λ = 503 nm), and yellow-red regions (maximum at λ = 574 nm), thus covering the visible electromagnetic spectrum. The features extracted from the deconvoluted curves and from the area under the respective transition curves are illustrated in Fig. ESI-4 (B), confirming that the red component is the largest one.

To understand the PL emission, one must remember what was discussed in Previous Section. The structure of the $ZnWO_4$ nanocrystals became more stable upon increasing the synthesis temperature to 150 °C, affording wide-band PL emission. However, when the $ZnWO_4$ structure reached the temperature saturation (160 °C), a decline of the PL intensity was observed (see Fig. 10) induced by the stabilization of the (010) and (011) surfaces and, consequently, favoring the emission in the yellow-red region.[118] This type of emission is related to oxygen vacancies located in the $[ZnO_4 \cdot 2V_O^x]$ and $[WO_5 \cdot V_O^x]$ clusters present in the (010) and (011) surfaces, inducing a new energy band gap region (higher wavelengths) at lower energies. According to Longo et al.,[118] the oxygen vacancies inducing yellow and red emission are caused by deep defects in the lattice.

In this way, the reduced PL intensity of the $ZnWO_4$ nanocrystals obtained at 160 °C is related to the oxygen vacancies present on the top of the surface of the structure and, consequently, the electronic levels are localized in the forbidden band gap and the E_{gap} value decreases (see Table 3). Moreover, the PL behavior is related to the formation of oxygen vacancies, as illustrated in the following Scheme 1.

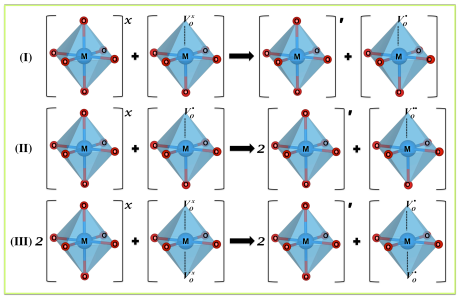

SCHEME 1 – Formation of oxygen vacancy from clusters interactions. M = Zn and/or W atoms; V_O^x = neutral oxygen vacancy; $V_O^{\cdot}$ = positive oxygen vacancy.

Oxygen vacancies can appear in different charge states in the disordered lattice, such as $[WO_5 \cdot V_O^x]$ and $[ZnO_5 \cdot V_O^x]$ or $[WO_4 \cdot 2V_O^x]$ and $[ZnO_4 \cdot 2V_O^x]$, where the vacancies donate electrons and are neutral in relation to the lattice (part (I) and (III) in the Scheme 1). $[WO_5 \cdot V_O^{\cdot}]$ and $[ZnO_5 \cdot V_O^{\cdot}]$ are singly ionized states and donate/capture electrons, and $[WO_5 \cdot V_O^{\cdot\cdot}]$ and $[ZnO_5 \cdot V_O^{\cdot\cdot}]$ are double-positively charged states in the lattice and capture electrons (part (II) in the Scheme 1). These oxygen vacancies induce the generation of new energy states in the band gap attributed to the $[WO_6]$ and $[ZnO_6]$ complex clusters.

Photocatalytic measurements. The promising photocatalytic activity of $ZnWO_4$ nanocrystals for the degradation of RhB was recently reported.[46, 123–126] Montine et al.[127] compared the activity of tungstates of divalent transition metals ($M^{II}WO_4$, M = Co^{II}, Ni^{II}, Cu^{II}, Zn^{II}) for the degradation of methylene blue (MB) and methyl orange (MO).

It was observed that the $ZnWO_4$ photocatalytic activity was highly superior to that of the other investigated tungstates. The full d-orbitals hybridized (d^{10} configuration) with the W 4d states present in $ZnWO_4$ affect the trapping of excitons, thus preventing electron–hole recombination and strongly enhancing the ability of this material to generate the radical species involved in organic compound mineralization processes.

The PCA of the $ZnWO_4$ nanocrystals synthesized at 140, 150, and 160 °C via the MH method was evaluated for RhB degradation in aqueous solution under UV irradiation. RhB absorbs light in the range of 200–600 nm, with a maximum at 554 nm. The temporal evolution of the absorption spectrum of the RhB aqueous solution in the presence of $ZnWO_4$ nanocrystals synthesized at different temperatures is shown in Fig. 11. It can be seen that the absorbance of RhB decreased quickly under UV irradiation with the irradiation time, and the absorption peak at 554 nm completely disappeared after irradiation in the presence of the $ZnWO_4$ catalysts (see Fig. 11 (A)). This decay occurs because the conjugated chromophore of RhB (a xanthene ring) undergoes a gradual de-ethylation process of the *N*,*N*'-diethylammonium functional groups, causing a hypochromic displacement of the absoprtion.[128]

Fig. 11 (B) compares the changes in the relative concentration of RhB with the irradiation time using the $ZnWO_4$ nanocrystals prepared at different temperatures. No obvious degradation of pure RhB was observed, indicating that the dye practically is barely degraded by UV light. The degradation efficiency of RhB increased with the increasing synthesis temperature; the efficiency reached 100% after 40 min of irradiation for the $ZnWO_4$ nanocrystals prepared at 160 °C. In contrast, the photocatalytic activity of the samples obtained at 150 and 140 °C was 100% after 50 and 70 min of irradiation, respectively.

This indicates that the crystallinity of the $ZnWO_4$ nanocrystal semiconductors plays an important role in the RhB photodegradation efficiency.

Generally, the dependence of the photocatalytic reaction rate on the concentration of an organic dye is well described by the Langmuir–Hinshelwood (L–H) model:[129, 130]

$$r = \frac{dC}{dt} = \frac{kKC}{1+KC} \quad (3)$$

where *r* is the reaction rate (mg/L min), *k* is the specific reaction rate constant (mg/L min), *K* is the adsorption coefficient (L/mg), and *C* is the concentration of the dye at time *t* (mg/L). When the initial dye concentration is low (C_0 is small), the above equation can be simplified to a pseudo-first-order equation:

$$\ln(C_0/C) = kKt = K_{app}t \quad (4)$$

To understand the reaction kinetics of RhB degradation in our experiments, plots of -ln(C_0/C) versus irradiation time for the $ZnWO_4$ nanocrystals synthesized at 140, 150, and 160 °C were constructed, as shown in Fig. 11 (C). The rate constants obtained from the regression lines are shown also in Fig. 11 (C). A fairly good correlation to the pseudo-first-order equation was observed, indicating that this reaction follows pseudo-first-order kinetics. The $ZnWO_4$ sample synthesized at 160 °C showed the highest *k* value, corresponding to the best photocatalytic activity.

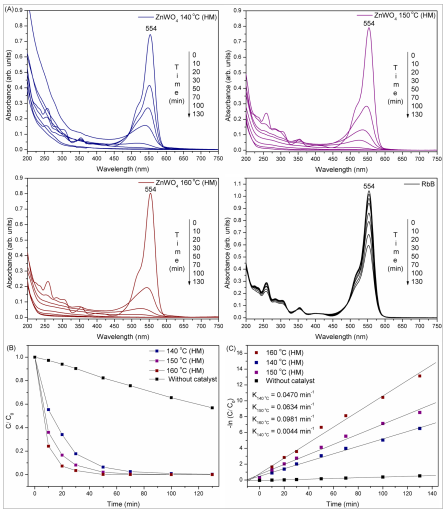

FIGURE 11 – (A) UV-vis absorption spectra of the RhB aqueous solution in the presence of $ZnWO_4$ nanocrystals, obtained by the MH method at 140, 150 and 160 °C for 1 h and in the presence of pure RhB. (B) Relative concentration of RhB dye (C/C_0) versus time (min) of $ZnWO_4$ nanocrystals, prepared at different temperatures. (C) Reaction kinetics of RhB degradation -ln(C_0/C) versus time (min) for the $ZnWO_4$ nanocrystals prepared at different temperatures.

As discussed in the PL, in the $ZnWO_4$ there are two differences of clusters into the structure $[MO_x \cdot xV_O^x]$ and the $[MO_6]$ clusters (where M = Zn and/or W) that formed the electron-hole pair, as shown in Scheme 1. In the photodegradation of RhB by $ZnWO_4$, it was proposed the following photo-oxidation mechanism, in which the $[MO_x \cdot xV_O^{\bullet}]$ clusters (hole specie) located on the top of the surface of the nanocrystals interact with the water forming the hydroxyl radical (OH^*) and proton ($H^{\bullet}$), reactive species, while the $[MO_6]'_0$ clusters (electron species) located inside the structure interact with O_2 generating the superoxide (O'_2). The $H^{\bullet}$ species are unstable, and quickly interact with O'_2 forming the perhydroxyl radicals (O_2H^*). Next, RhB is degraded by OH^* and O_2H^* radicals producing colorless compounds organic (CCO), carbon dioxide (CO_2), and water (H_2O), as shown in Scheme 2.

How as proposed in the literature, the active species are: holes, electrons, OH^*, O_2H^* and O'_2 and their corresponding activities were investigated using different types of active species scavengers.[131-134] Fig. 12 shows the percentage of degradation of RhB after 60 min of exposure to UV-vis radiation in function of the scavengers action of reactive species.

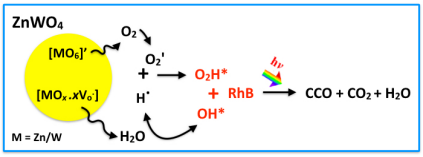

SCHEME 2 – Proposed mechanism of photodegradation of RhB dye in CCO, CO_2 and H_2O, in the presence of $ZnWO_4$ nanocrystals.

As shown in Fig. 12, when $AgNO_3$ it was added to the reaction mixture, that is an electron scavenger, the degradation reached 100% after 20 min of irradiation. By preventing the recombination using $AgNO_3$, the highly oxidizing VB holes are able to oxidize water, making available a higher quantity of holes for this oxidation.[135]

When the hydroxyl radical scavenger tetrabutylammonium (TBA) was added, the rate of degradation of RhB was considerably reduced. This suggests that OH^* radicals participate in the degradation of RhB along with other oxidative radical species. Addition of the superoxide radical scavenger benzoquinone (BQ) also decrease the degradation rate of RhB. This shows that some O'_2 species are also present in the equilibrium.[136]

When ammonium oxalate (AO), often used as a holes capturer, was added to the reaction system, the degradation process was inhibited once that the $ZnWO_4$ holes can not interact with the water to generate the active species. Thus, it was concluded that the presence of holes is a limited factor in the photocatalytic activity as well in the degradation rate.

According to the DOS analysis (see Fig. 9 (B)), the differences in the hybridization of the W, Zn, and O atoms and the different coordination numbers of the Zn and W clusters can generate intermediary energy levels (or "defects") located between the VB and CB. When these defects polarize the lattice, transitions between the clusters can occur. Therefore, the UV light is absorbed and polarization processes occur.

In an ideal structure, each atom is perfectly located in a site; however, this does not happen in nature. Thus, it is possible to find $[\mathrm{MO}_x \cdot x\mathrm{V}_\mathrm{O}^x]$ clusters located on the top of the surface and $[\mathrm{MO}_6]_\mathrm{o}'$ located inside the nanocrystals.

According to the proposed photocatalytic mechanism, the defects play a crucial role in the production of OH^* and O_2H^* radicals, which are the main active species for the degradation of RhB.

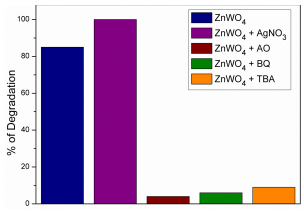

FIGURE 12 – Percentage of degradation (%) of RhB dye under exposure to UV-vis radiation, in the presence of $ZnWO_4$ nanocrystals and different scavenger.

The sample prepared at 160 °C exhibited the best photocatalytic activity, and thus we propose that the formation of the active species OH^*, $H^\bullet$, and O_2' must be associated to the type of surface stabilized in the material. As shown previously, at 160 °C, (010) and (011) surfaces were observed containing vacancies associated with clusters of $[\mathrm{ZnO}_4 \cdot 2\mathrm{V}_\mathrm{O}^x]$ and $[\mathrm{ZnO}_4 \cdot 2\mathrm{V}_\mathrm{O}^x]$ / $[\mathrm{WO}_5 \cdot \mathrm{V}_\mathrm{O}^x]$, respectively. As only the structure obtained at 160 °C contains $[\mathrm{ZnO}_4 \cdot 2\mathrm{V}_\mathrm{O}^x]$ clusters in the top of the surface, this type of clusters must be the most efficient for the generation of active species for RhB photodegradation, making it a superior catalyst than the samples synthesized at lower temperatures.

Conclusions

In summary, $ZnWO_4$ nanocrystals were successfully synthesized by an MH method and, for first time, the effect of the temperature on the crystal structure, morphology, and optical properties was investigated. First-principles calculations at the density functional theory level provided in-depth understanding of the electronic and structural properties of $ZnWO_4$. The main conclusions can be summarized as follows: i) The XRD patterns and Rietveld refinement data showed that $ZnWO_4$ nanocrystals are monophasic with a monoclinic structure of wolframite type. ii) MR and FT-IR spectroscopies were employed to verify the vibrational modes and the results confirmed that all vibrational modes are characteristic of a monoclinic structure. The theoretical values of the Raman spectra are consistent with previously reported experimental values. iii) The FE-SEM images revealed that the synthesis temperature influences the shape and size of the $ZnWO_4$ nanocrystals, showing undefined morphology at 140 °C, while defined polyhedral (e.g., nanorods), rectangular, and hexagonal plates were observed in the sample prepared at 160 °C. iv) The Wulff construction method was employed to obtained the morphologies and their transformations. The surface energy of each facet depended on the temperature; thus, less energetic surfaces were stabilized with the increasing temperature. v) The UV-vis spectra revealed direct transitions between the VB and CB. The theoretical values of the UV-vis spectra are in agreement with the experimental results. vi) The PL behavior of the $ZnWO_4$ samples is associated with oxygen vacancies (V_O^x), which cause a red shift related to an increase of deep defects. vii) Finally, it was conclude that the photocatalytic activity of the ZnWO4 nanoparticles are controlled by the amount of holes in the structure and the sample prepared at 160 °C exhibits the best photocatalytic activity.

This experimental and theoretical work provides insight into the fine effects of the synthesis temperature on the morphology and photoluminescence properties of $ZnWO_4$ nanocrystals, as well as the role of the electronic structure on their photocatalytic activity.

Conflicts of interest

There are no conflicts to declare.

Acknowledgements

This work was financially supported by Fundação de Amparo à Pesquisa do Estado de São Paulo (FAPESP 2012/14004-5, 2013/07296-2, 2013/26671-9, 2013/23995-8, 2014/14171-4, 2017/13008-0 and 2017/07240-8), Conselho Nacional de Desenvolvimento Científico e Tecnológico (CNPq; 479644/2012-8, 350711/2012-7, 304531/2013-8 and 151136/2013-0). Coordenação de Aperfeiçoamento de Pessoal de Nível Superior. J.A. is grateful to GeneralitatValenciana for *PrometeoII*/2014/022, ACOMP/2014/270, and ACOMP/2015/1202 projects, Ministerio de Economia y Competitividad (Spain), for CTQ2015-65207-P project, and Programa de Cooperación Científica con Iberoamerica (Brasil) of Ministerio de Educación (Spanish Brazilian program PHBP14-00020), J.A. acknowledges Ministerio de Economia y Competitividad, "Salvador Madariaga" program, PRX15/00261.

References

1 R. Kumar, D. Rana, A. Umar, P. Sharma, S. Chauhan and M. S. Chauhan, *Talanta*, 2015, **137**, 204-213.
2 J. Sima and P. Hasal, *Chem. Eng. Trans.*, 2013, **32**, 79-84.
3 J. F. Wang, T. Tsuzuki, B. Tang, X. L. Hou, L. Sun and X. G. Wang, *ACS Appl. Mater. Interfaces*, 2012, **4**, 3084-3090.
4 M. Wang, Y. F. Gao, L. Dai, C. X. Cao, Z. Chen and X. H. Guo, *Sci. Adv. Mater.*, 2013, **5**, 1867-1876.
5 S. K. Kansal and N. Kaur, *Energy Environ. Focus* 2013, **2**, 163-167.
6 D. P. Mohapatra, S. K. Brar, P. Picard and R. D. Tyagi, *Sci. Adv. Mater.*, 2013, **5**, 57-63.
7 M. A. Gondal, M. A. Dastageer, S. G. Rashid, S. M. Zubair, M. A. Ali, D. H. Anjum, J. H. Lienhard, G. H. McKinley and K. Varanasi, *Sci. Adv. Mater.*, 2013, **5**, 2007-2014.

8 J. Wang, J. Liu, H. Xu, S. Ji, J. Wang and X. Tian, *Energy Environ. Focus*, 2013, **2**, 79-84.
9 L. Jin, X. Zeng, M. Liu and N. Y. He, *Sci. Adv. Mater.*, 2013, **5**, 2053-2057.
10 P. Singhal, S. Rawalekar, S. Kaniyankandy and H. N. Ghosh, *Sci. Adv. Mater.*, 2013, **5**, 1354-1363.
11 J. Liu, H. Yu, L. Zhang, G. Zhang, J. Qu and H. Lv, *Sens. Lett.*, 2013, **11**, 1293-1297.
12 H. Li, S. Yin, Y. Wang, Q. Dong, C. Guo and T. Sato, *Energy Environ. Focus*, 2012, **1**, 39-44.
13 S. R. Collinson and O. D. Garcia, *Sci. Adv. Mater.*, 2013, **5**, 1427-1435.
14 D. Jiang, B. Tang, H. Y. Guo, W. Q. Xu and S. P. Xu, *Sci. Adv. Mater.*, 2013, **5**, 1105-1110.
15 C. H. Wang, C. L. Shao, Y. C. Liu and X. H. Li, *Inorg. Chem.*, 2009, **48**, 1105-1113.
16 J. Ren, W. Z. Wang, M. Shang, S. M. Sun and E. P. Gao, *Acs Appl. Mater. Interfaces*, 2011, **3**, 2529-2533.
17 X. Zhang, C. L. Shao, Z. Y. Zhang, J. H. Li, P. Zhang, M. Y. Zhang, J. B. Mu, Z. C. Guo, P. P. Liang and Y. C. Liu, *ACS Appl. Mater. Interfaces*, 2012, **4**, 785-790.
18 P. N. Zhu, A. S. Nair, P. Shengjie, Y. Shengyuan and S. Ramakrishna, *ACS Appl. Mater. Interfaces*, 2012, **4**, 581-585.
19 W. J. Li, D. Z. Li, W. J. Zhang, Y. Hu, Y. H. He and X. Z. Fu, *J. Phys. Chem. C*, 2010, **114**, 2154-2159.
20 N. Kawasaki, F. Ogata and H. Tominaga, *J. Hazard. Mater.*, 2010, **181**, 574-579.
21 L. M. Camacho, A. Torres, D. Saha and S. G. Deng, *J. Colloid Interface Sc.*, 2010, **349**, 307-313.
22 T. Madrakian, A. Afkhami, M. A. Zolfigol, M. Ahmadi and N. Koukabi, *Nano-Micro Lett.*, 2012, **4**, 57-63.
23 A. Kubacka, M. Fernandez-Garcia and G. Colon, *Chem. Rev.*, 2012, **112**, 1555-1614.
24 A. L. M. Reddy, S. R. Gowda, M. M. Shaijumon and P. M. Ajayan, *Adv. Mater.*, 2012, **24**, 5045-5064.
25 Z. L. Wang and W. Z. Wu, *Angew. Chem. Int. Ed.*, 2012, **51**, 11700-11721.
26 X. Chen and S. S. Mao, *Chem. Rev.*, 2007, **107**, 2891-2959.
27 W. Li, L. Y. Cao, X. G. Kong, J. F. Huang, C. Y. Yao, J. Fei and J. Y. Li, *Rsc Adv.*, 2016, **6**, 23783-23789.
28 C. L. Zhang, H. L. Zhang, K. Y. Zhang, X. Y. Li, Q. Leng and C. G. Hu, *Acs Appl. Mater. Interfaces*, 2014, **6**, 14423-14432.
29 M. Rahimi-Nasrabadi, S. M. Pourmortazavi, M. R. Ganjali, S. S. Hajimirsadeghi and M. M. Zahedi, *J. Mol. Struct.*, 2013, **1047**, 31-36.
30 S. H. Yu, B. Liu, M. S. Mo, J. H. Huang, X. M. Liu and Y. T. Qian, *Adv. Funct. Mater.*, 2003, **13**, 639-647.
31 X. Zhao, W. Q. Yao, Y. Wu, S. C. Zhang, H. P. Yang and Y. F. Zhu, *J. Solid State Chem.*, 2006, **179**, 2562-2570.
32 A. L. M. de Oliveira, J. M. Ferreira, M. R. S. Silva, S. C. de Souza, F. T. G. Vieira, E. Longo, A. G. Souza and I. M. G. Santos, *J. Therm. Anal. Calorim.*, 2009, **97**, 167-172.
33 H. B. Fu, J. Lin, L. W. Zhang and Y. F. Zhu, *Appl. Catal., A*, 2006, **306**, 58-67.
34 O. Y. Khyzhun, V. L. Bekenev, V. V. Atuchin, E. N. Galashov and V. N. Shlegel, *Mater. Chem. Phys.*, 2013, **140**, 588-595.
35 R. Shi, Y. J. Wang, D. Li, J. Xu and Y. F. Zhu, *Appl. Catal., B*, 2010, **100**, 173-178.
36 A. Thomas, C. Janaky, G. F. Samu, M. N. Huda, P. Sarker, J. P. Liu, V. N. Vuong, E. H. Wang, K. A. Schug and K. Rajeshwar, *Chemsuschem*, 2015, **8**, 1652-1663.
37 Y. Wang, L. Liping and G. Li, *Appl. Surf. Sci.*, 2017, **393**, 159-167.
38 N. Shi, S. Xiong, F. Wu, J. Bai, Y. Chu, H. Mao, J. Feng and B. Xi, *Eur. J. Inorg. Chem.*, 2017, **2017**, 734-740.
39 X. Wang, Z. Fan, H. H. Yu, H. J. Zhang and J. Y. Wang, *Opt. Mater. Express*, 2017, **7**, 1732-1744.
40 S. Zhan, F. Zhou, N. Huang, Y. Liu, Q. He, Y. Tian, Y. Yang and F. Ye, *Appl. Surf. Sci.*, 2017, **391**, 609-616.
41 G. B. Kumar, K. Sivaiah and S. Buddhudu, *Ceram. Int.*, 2010, **36**, 199-202.
42 E. N. Galashov, V. A. Gusev, V. N. Shlegel and Y. V. Vasiliev, *Crystallogr. Rep.*, 2009, **54**, 689-691.
43 C. S. Lim, *J. Ceram. Process. Res.*, 2011, **12**, 140-145.
44 M. Bonanni, L. Spanhel, M. Lerch, E. Fuglein, G. Muller and F. Jermann, *Chem. Mater.*, 1998, **10**, 304-310.
45 C. Q. Ge, C. S. Xie, D. W. Zeng and S. Z. Caiy, *J. Am. Ceram. Soc.*, 2007, **90**, 3263-3267.
46 K. M. Garadkar, L. A. Ghule, K. B. Sapnar and S. D. Dhole, *Mater. Res. Bull.*, 2013, **48**, 1105-1109.
47 M. Mancheva, R. Iordanova and Y. Dimitriev, *J. Alloys Compd.*, 2011, **509**, 15-20.
48 U. M. Garcia-Perez, A. Martinez-de La Cruz and J. Peral, *Electrochim. Acta*, 2012, **81**, 227-232.
49 T. Dong, Z. Li, Z. Ding, L. Wu, X. Wang and X. Fu, *Mater. Res. Bull.*, 2008, **43**, 1694-1701.
50 J. Lin, J. Lin and Y. Zhu, *Inorg. Chem.*, 2007, **46**, 8372−8378.
51 D. Li, R. Shi, C. S. Pan, Y. F. Zhu and H. J. Zhao, *Crystengcomm*, 2011, **13**, 4695-4700.
52 Z. Amouzegar, R. Naghizadeh, H. R. Rezaie, M. Ghahari and M. Aminzare, *Ceram. Int.*, 2015, **41**, 8352-8359.
53 E. D. Bojesen, K. M. O. Jensen, C. Tyrsted, A. Mamakhel, H. L. Andersen, H. Reardon, J. Chevalier, A. C. Dippel and B. B. Iversen, *Chem. Sci.*, 2016, **7**, 6394-6406.
54 T. Yamada, Y. Sukegawa, H. Wagata, K. Yubuta and K. Teshima, *Crystengcomm*, 2016, **18**, 8608-8613.
55 J. Bi, L. Wu, Z. Li, Z. Ding, X. Wang and X. Fu, *J. Alloys Compd.*, 2009, **480**, 684-688.
56 D. W. Kim, I. S. Cho, S. S. Shin, S. Lee, T. H. Noh, D. H. Kim, H. S. Jung and K. S. Hong, *J. Solid State Chem.*, 2011, **184**, 2103-2107.
57 Y. J. Wang, Z. X. Wang, S. Muhammad and J. He, *Crystengcomm*, 2012, **14**, 5065-5070.
58 W. X. Zhao, B. Sun, Y. H. Liu, L. J. Wei, H. W. Li and P. Chen, *Aip Advances*, 2014, **4**.
59 G. Q. Tan, L. L. Zhang, S. S. Wei, A. Xia and H. J. Ren, *Cryst. Res. Technol.*, 2012, **47**, 1279-1283.
60 P. Yadav, S. K. Rout and E. Sinha, *J. Alloys Compd.*, 2017, In Press.
61 J. Andres, L. Gracia, P. Gonzalez-Navarrete, V. M. Longo, W. Avansi, Jr., D. P. Volanti, M. M. Ferrer, P. S. Lemos, F. A. La Porta, A. C. Hernandes and E. Longo, *Sci. Rep.*, 2014, **4**, 5391-5397.
62 V. V. Atuchin, E. N. Galashov, O. Y. Khyzhun, V. L. Bekenev, L. D. Pokrovsky, Y. A. Borovlev and V. N. Zhdankov, *J. Solid State Chem.*, 2016, **236**, 24-31.
63 C. X. Li, P. A. Ma, P. P. Yang, Z. H. Xu, G. G. Li, D. M. Yang, C. Peng and J. Lin, *Crystengcomm*, 2011, **13**, 1003-1013.
64 L.-Y. Meng, B. Wang, M.-G. Ma and K.-L. Lin, *Mater. Chem. Today*, 2016, **1–2**, 63-83.
65 Y. J. Zhu and F. Chen, *Chem. Rev.*, 2014, **114**, 6462-6555.
66 D. Stuerga, in *Microwaves in Organic Synthesis*, eds. A. d. l. Hoz and A. Loupy, Wiley-VCH Verlag GmbH & Co. KGaA, Weinheim, Germany, 2012, vol. 1, pp. - 56.
67 C. O. Kappe, B. Pieber and D. Dallinger, *Angew. Chem. Int. Ed.*, 2013, **52**, 1088-1094.
68 C. O. Kappe, *Chem. Soc. Rev.*, 2013, **42**, 4977-4990.
69 G. Kresse and J. Furthmuller, *Comput. Mater. Sci.*, 1996, **6**, 15-50.
70 G. Kresse and J. Hafner, *Phys. Rev. B: Condens. Matter Mater. Phys.*, 1994, **49**, 14251-14269.
71 J. P. Perdew, K. Burke and M. Ernzerhof, *Phys. Rev. Lett.*, 1996, **77**, 3865-3868.
72 G. Kresse and D. Joubert, *Phys. Rev. B: Condens. Matter Mater. Phys.* , 1999, **59**, 1758-1775.
73 J. Andrés, L. Gracia, A. F. Gouveia, M. M. Ferrer and E. Longo, *Nanotechnology* 2015, **26**, 405703-405713.
74 Y. Huang, Y. Gao, Q. Zhang, J.-j. Cao, R.-j. Huang, W. Ho and S. C. Lee, *Appl. Catal., A*, 2016, **515**, 170-178.
75 H. Fu, J. Lin, L. Zhang and Y. Zhu, *Appl. Catal., A*, 2006, **306**, 58-67.
76 Y. Keereeta, S. Thongtem and T. Thongtem, *Powder Technol.*, 2015, **284**, 85-94.
77 Z. Amouzegar, R. Naghizadeh, H. R. Rezaie, M. Ghahari and M. Aminzare, *Ceram. Int.*, 2015, **41**, 1743-1747.
78 A. F. Gouveia, J. C. Sczancoski, M. M. Ferrer, A. S. Lima, M. R. Santos, M. S. Li, R. S. Santos, E. Longo and L. S. Cavalcante, *Inorg. Chem.*, 2014, **53**, 5589-5599.
79 I. M. Pinatti, I. C. Nogueira, W. S. Pereira, P. F. S. Pereira, R. F. Gonçalves, J. A. Varela, E. Longo and I. L. V. Rosa, *Dalton Trans.*, 2015, **44**, 17673-17685.

80 Z. Lin, J. Li, Z. Zheng, J. Yan, P. Liu, C. Wang and G. Yang, *ACS Nano*, 2015, **9**, 7256–7265.
81 R. A. Roca, J. C. Sczancoski, I. C. Nogueira, M. T. Fabbro, H. C. Alves, L. Gracia, L. P. S. Santos, C. P. de Sousa, J. Andres, G. E. Luz, Jr., E. Longo and L. S. Cavalcante, *Catal. Sci. Techn.*, 2015, **5**, 4091-4107.
82 E. Longo, L. S. Cavalcante, D. P. Volanti, A. F. Gouveia, V. M. Longo, J. A. Varela, M. O. Orlandi and J. Andres, *Sci. Rep.*, 2013, **3**, 1676.
83 P. F. Schofield, K. S. Knight, S. A. T. Redfern and G. Cresse, *Acta Cryst.*, 1997, **B53**, 102-112.
84 P. F. S. Pereira, A. P. de Moura, I. C. Nogueira, M. V. S. Lima, E. Longo, P. C. de Sousa Filho, O. A. Serra, E. J. Nassar and I. L. V. Rosa, *J. Alloys Compd.*, 2012, **526**, 11-21.
85 H. M. Rietveld, *J. Appl. Crystallogr.*, 1969, **2**, 65-71.
86 A. C. Larson and R. B. Von Dreele, *Gem. Struc. Anal. Syst.*, 2004, 1-224.
87 P. F. S. Pereira, C. C. Santos, A. F. Gouveia, M. M. Ferrer, I. M. Pinatti, G. Botelho, J. R. Sambrano, I. L. V. Rosa, J. Andres and E. Longo, *Inorg. Chem.*, 2017, **56**, 7360-7372.
88 K. Wang, W. Feng, X. Feng, Y. Li, P. Mi and S. Shi, *Spectrochim. Acta, Part A*, 2016, **154**, 72-75.
89 L. S. Cavalcante, E. Moraes, M. A. P. Almeida, C. J. Dalmaschio, N. C. Batista, J. A. Varela, E. Longo, M. S. Li, J. Andres and A. Beltran, *Polyhedron*, 2013, **54**, 13-25.
90 K. Momma and F. Izumi, *J. Appl. Cryst.*, 2011, **44**, 1272-1276.
91 P. Siriwong, T. Thongtem, A. Phuruangrat and S. Thongtem, *Crystengcomm*, 2011, **13**, 1564-1569.
92 A. Kuzmin and J. Purans, *Radiation Measurements*, 2001, **33**, 583-586.
93 M. G. Brik, V. Nagirnyi and M. Kirm, *Mater. Chem. Phys.*, 2013, **137**, 977-983.
94 S. R. Ede, A. Ramadoss, U. Nithiyanantham, S. Anantharaj and S. Kundu, *Inorg.Chem.*, 2015, **54**, 3851-3863.
95 R. C. Dai, Z. P. Wang, Z. M. Zhang and Z. J. Ding, *Surf. Interface Anal.*, 2014, **46**, 1151-1155.
96 Tasoltan T Basiev, Aleksandr Ya Karasik, A A Sobol, D. S. Chunaev and V. E. Shukshin, *Quantum Electron.*, 2011, **41**, 370-372.
97 H.-W. Shim, I.-S. Cho, K. S. Hong, A.-H. Lim and D.-W. Kim, *J. Phys. Chem., C*, 2011, **115**, 16228-16233.
98 D. Errandonea, F. J. Manjón, N. Garro, P. Rodríguez-Hernández, S. Radescu, A. Mujica, A. Muñoz and C. Y. Tu, *Phys. Rev. B*, 2008, **78**.
99 L. H. Hoang, N. T. M. Hien, W. S. Choi, Y. S. Lee, K. Taniguchi, T. Arima, S. Yoon, X. B. Chen and I.-S. Yang, *J. Raman Spectrosc.*, 2010, **41**, 1005-1010.
100 Y. Zhai, M. Wang, Q. Zhao, J. Yu and X. Li, *J. Lumin.*, 2016, **172**, 161-167.
101 V. V. Fomichev and I. Kondratov, *Spectrochim. Acta*, 1994, **50A**, 1113-1120.
102 C. Yu and J. C. Yu, *Mater. Sci. Eng., B*, 2009, **164**, 16-22.
103 Y. X. Zhou, L. Tong, X. B. Chen and X. H. Zeng, *Appl. Phys. A*, 2014, **117**, 673-679.
104 J. Yan, Y. H. Shen, F. Li and T. H. Li, *Sci. World J.*, 2013, DOI: 10.1155/2013/458106.
105 A. F. Gouveia, M. M. Ferrer, J. R. Sambrano, J. Andres and E. Longo, *Chem. Phys. Lett.*, 2016, **660**, 87-92.
106 M. M. Ferrer, A. F. Gouveia, L. Gracia, E. Longo and J. Andres, *Modell. Simul. Mater. Sci. Eng.*, 2016, **24**, 025007-025016.
107 D. L. Wood and J. Tauc, *Phys. Rev. B*, 1972, **5**, 3144-3151.
108 P. Kubelka and F. Munk, *Zeit. Fur. Tech. Physik*, 1931, **12**, 593-601.
109 R. Lacomba-Perales, J. Ruiz-Fuertes, D. Errandonea, D. Martínez-García and A. Segura, *EPL (Europhysics Letters)*, 2008, **83**, 37002.
110 I. L. Validžić, T. D. Savić, R. M. Krsmanović, D. J. Jovanović, M. M. Novaković, M. Č. Popović and M. I. Čomor, *Mater. Sci. Eng., B*, 2012, **177**, 645-651.
111 J. Ruiz-Fuertes, S. López-Moreno, J. López-Solano, D. Errandonea, A. Segura, R. Lacomba-Perales, A. Muñoz, S. Radescu, P. Rodríguez-Hernández, M. Gospodinov, L. L. Nagornaya and C. Y. Tu, *Phys. Rev. B*, 2012, **86**.
112 H. Huang, Y. He, Z. Lin, L. Kang and Y. Zhang, *J. Phys. Chem. C*, 2013, **117**, 22986-22994.
113 H. Huang, Y. He, X. Du, P. K. Chu and Y. Zhang, *ACS Sus. Chem. Eng.*, 2015, **3**, 3262-3273.
114 C. Li, Y. Liang, J. Mao, L. Ling, Z. Cui, X. Yang, S. Zhu and Z. Li, *Anal Chim. Acta*, 2016, **927**, 107-116.
115 V. M. Longo, C. C. De Foggi, M. M. Ferrer, A. F. Gouveia, R. S. Andre, W. Avansi, C. E. Vergani, A. L. Machado, J. Andres, L. S. Cavalcante, A. C. Hernandes and E. Longo, *J. Phys. Chem. A*, 2014, **118**, 5769-5778.
116 E. Longo, D. P. Volanti, V. M. Longo, L. Gracia, I. C. Nogueira, M. A. P. Almeida, A. N. Pinheiro, M. M. Ferrer, L. S. Cavalcante and J. Andres, *J. Phys. Chem. C*, 2014, **118**, 1229-1239.
117 L. S. Cavalcante, M. A. Almeida, W. Avansi, Jr., R. L. Tranquilin, E. Longo, N. C. Batista, V. R. Mastelaro and M. S. Li, *Inorg. Chem.*, 2012, **51**, 10675-10687.
118 V. M. Longo, E. Orhan, L. S. Cavalcante, S. L. Porto, J. W. M. Espinosa, J. A. Varela and E. Longo, *Chemical Physics*, 2007, **334**, 180-188.
119 M. Hojamberdiev, G. Zhu and Y. Xu, *Mater. Res. Bull.*, 2010, **45**, 1934-1940.
120 G. He, H. Fan, L. Ma, K. Wang, D. Ding, C. Liu and Z. Wang, *Mater. Sci. Semicond. Process.*, 2016, **41**, 404-410.
121 Fang Lei, Bing Yan, Hao-Hong Chen, Qiang Zhang and J.-T. Zhao, *Crys. Growth. Des.*, 2009, **9**, 3730–3736.
122 A. A. Blistanov, B. I. Zadneprovski, M. A. Ivanov, V. V. Kochurikhin, V. S. Petrakov and I. O. Yakimova, *Crystallogr. Rep.*, 2005, **50**, 284–290.
123 Shaohua Chen, Sixiu Sun, Honggang Sun, Weiliu Fan, Xian Zhao and X. Sun, *J. Phys. Chem. C*, 2010, **114**, 7680–7688.
124 L. Zhang, Z. Wang, L. Wang, Y. Xing, X. Li and Y. Zhang, *Appl. Surf. Sci.*, 2014, **305**, 179-185.
125 D. He, X. Zhang, T. Xie, J. Zhai, H. Li, L. Chen, L. Peng, Y. Zhang and T. Jiang, *Appl. Surf. Sci.*, 2011, **257**, 2327-2331.
126 R. Shi, Y. Wang, D. Li, J. Xu and Y. Zhu, *Appl. Catal., B*, 2010, **100**, 173-178.
127 T. Montini, V. Gombac, A. Hameed, L. Felisari, G. Adami and P. Fornasiero, *Chem. Phys. Lett.*, 2010, **498**, 113-119.
128 X. Zhao and Y. F. Zhu, *Environ. Sci. Technol.*, 2006, **40**, 3367-3372.
129 H. Farsi, Z. Barzgari and S. Z. Askari, *Res. Chem. Intermed.*, 2014, **41**, 5463-5474.
130 Antonio Eduardo H. Machado, Jacques A. de Miranda, Renato F. de Freitas, Edward Thomas F.M. Duarte, Lucas F. Ferreira, Yaico D.T. Albuquerque, Reinaldo Ruggiero, Christian Sattler and L. d. Oliveira, *J. Photochem. Photobiol., A*, 2003, **155**, 231–241.
131 Y. Zhang, N. Zhang, Z.-R. Tang and Y.-J. Xu, *ACS Nano*, 2012, **6**, 9777-9789.
132 H. Huang, X. Han, X. Li, S. Wang, P. K. Chu and Y. Zhang, *ACS Appl. Mater. Interfaces*, 2015, **7**, 482-492.
133 H. Huang, X. Li, J. Wang, F. Dong, P. K. Chu, T. Zhang and Y. Zhang, *ACS Catal.*, 2015, **5**, 4094-4103.
134 H. Huang, S. Tu, C. Zeng, T. Zhang, A. H. Reshak and Y. Zhang, *Angew. Chem. Int. Ed.*, 2017, **56**, 11860-11864.
135 D. J. Martin, G. Liu, S. J. Moniz, Y. Bi, A. M. Beale, J. Ye and J. Tang, *Chem. Soc. Rev.*, 2015, **44**, 7808-7828.
136 P. Raja, A. Bozzi, H. Mansilla and J. Kiwi, *J. Photochem. Photobiol., A*, 2005, **169**, 271-278.

2.2 – Effects of surface stability on the morphological transformation of metals and metal oxides as investigated by first-principles calculations

IOP Publishing Nanotechnology
Nanotechnology 26 (2015) 405703 (11pp) doi:10.1088/0957-4484/26/40/405703

Effects of surface stability on the morphological transformation of metals and metal oxides as investigated by first-principles calculations

Juan Andrés[1], Lourdes Gracia[1], Amanda Fernandes Gouveia[2], Mateus Meneghetti Ferrer[2] and Elson Longo[3]

[1] Department of Analytical and Physical Chemistry, University Jaume I (UJI), Castelló E-12071, Spain
[2] INCTMN-UFSCar, Universidade Federal de São Carlos, PO Box 676, 13565-905 são Carlos, SP, Brazil
[3] INCTMN-UNESP, Universidade Estadual Paulista, PO Box 355, CEP 14801-907 Araraquara, SP, Brazil

E-mail: andres@qfa.uji.es

Received 30 June 2015, revised 13 August 2015
Accepted for publication 14 August 2015
Published 17 September 2015

Abstract

Morphology is a key property of materials. Owing to their precise structure and morphology, crystals and nanocrystals provide excellent model systems for joint experimental and theoretical investigations into surface-related properties. Faceted polyhedral crystals and nanocrystals expose well-defined crystallographic planes depending on the synthesis method, which allow for thoughtful investigations into structure–reactivity relationships under practical conditions. This feature article introduces recent work, based on the combined use of experimental findings and first-principles calculations, to provide deeper knowledge of the electronic, structural, and energetic properties controlling the morphology and the transformation mechanisms of different metals and metal oxides: Ag, anatase TiO_2, $BaZrO_3$, and α-Ag_2WO_4. According to the Wulff theorem, the equilibrium shapes of these systems are obtained from the values of their respective surface energies. These investigations are useful to gain further understanding of how to achieve morphological control of complex three-dimensional crystals by tuning the ratio of the surface energy values of the different facets. This strategy allows the prediction of possible morphologies for a crystal and/or nanocrystal by controlling the relative values of surface energies.

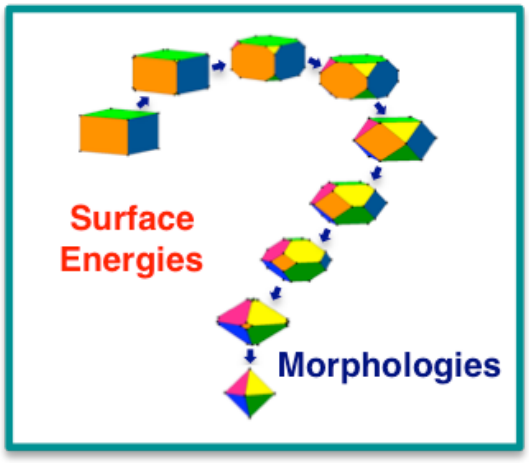

Effects of surface stability on the morphological transformation of metals and metal oxides as investigated by first-principles calculations

Juan Andrés[1]*, Lourdes Gracia[1], Amanda Fernandes Gouveia[2], Mateus Meneghetti Ferrer[2], and Elson Longo[3].
[1]Department of Analytical and Physical Chemistry, University Jaume I (UJI), Castelló 12071, Spain.
[2]INCTMN-UFSCar, Universidade Federal de São Carlos, P.O. Box 676, 13565-905 São Carlos, SP, Brazil.
[3]INCTMN-UNESP, Universidade Estadual Paulista, P.O. Box 355, CEP 14801-907 Araraquara, SP, Brazil.

Morphology is a key property of materials. Owing to their precise structure and morphology, crystals and nanocrystals provide excellent model systems for joint experimental and theoretical investigations into surface-related properties. Faceted polyhedral crystals and nanocrystals expose well-defined crystallographic planes depending on the synthesis method, which allow for thoughtful investigations into structure–reactivity relationships under practical conditions. This feature article introduces recent work, based on the combined use of experimental findings and first-principles calculations, to provide deeper knowledge of the electronic, structural, and energetic properties controlling the morphology and the transformation mechanisms of different metals and metal oxides: Ag, anatase TiO_2, $BaZrO_3$, and α-Ag_2WO_4. According to the Wulff theorem, the equilibrium shapes of these systems are obtained from the values of their respective surface energies. These investigations are useful to gain further understanding of how to achieve morphological control of complex three-dimensional crystals by tuning the ratio of the surface energy values of the different facets. This strategy allows the prediction of possible morphologies for a crystal and/or nanocrystal by controlling the relative values of surface energies.

Introduction

The ability to prepare nano- and microstructures with a well-defined morphology and excellent monodispersity at the nano- and bulk scale is an essential requirement for materials applications [1, 2]. It is generally accepted that the morphology, dimensionality, and crystal structure of the materials all play important roles in the electronic, optical, magnetic, catalytic, chemical, and other physical properties [3, 4]. Crystal morphology is governed by anisotropic surface properties, i.e., the presence of face-specific molecular arrangements, and is a critical determinant of the physical and chemical properties of crystalline materials. These molecular arrangements stem from the crystal structure and possess a symmetry that allows a group of faces, known as a family, to share identical arrangements. The anisotropic surface properties control the surface energies, growth rates, dissolution rates, wettability, cohesion, adhesion, etc. Because of the presence of surface energy anisotropy, unstable surfaces try to stabilize through the creation of low-energy surfaces; this is commonly called faceting [5]. The control of crystal morphology is a complex and difficult process, which depends both on the crystal internal structures and external growth conditions such as the synthesis process, the solvents used, and the process additives. In this context, Xue *et al* have developed a chemical bonding theory of single crystal growth [6, 7]. Very recently [8], these authors have reported the morphology engineering of electrode materials that can increase the performance of electrochemical energy storage devices such as Cu_2O- and MnO_2-based systems.

The relative growth rate of crystal faces, which depends on environmental conditions, evokes transformations in crystal morphology because of the appearance and/or dis- appearance of faces. These transformations are due to the geometric constraints imposed by the crystal structure and are associated with the relative surface energy values of each face. The observed crystal shapes are often interpreted in terms of Wulff construction [9, 10] offers a simple method to determine the equilibrium crystal shape, and different numerical implementations of this procedure are available in the literature [11–13]. Such a description is appropriate at the thermodynamic equilibrium.

This study reports results from theoretical and computational chemistry, in particular, the combination of first- principles calculations with an algorithm based on the Wulff construction, to find suitable morphological structure candidates. This perspective presents a comprehensive framework to rationalize crystal morphology and morphology evolution in crystalline materials, and summarizes our research efforts, which target the determination of the morphology in a set of materials ranging from metals to both simple and complex metal oxides: Ag, anatase TiO_2, $BaZrO_3$, and α-Ag_2WO_4. The following discussion is divided into three sections. The first section focuses on the state-of-the-art developments in this research field. The theoretical procedure and computational method are presented in section two. The third section presents the results and a process of how to create a mapping of all shape crystal possibilities to evaluate the methods to simulate suitable morphological structural candidates in order to obtain the experimental morphology of the as-synthesized samples.

State-of-the-art developments

For a crystalline material, different surfaces may have different geometric and electronic structures, and exhibit different physical and chemical properties. Accordingly, their morphology is dependent on the surface energies of the different exposed surfaces, and one may expect to tune the properties of materials by simply controlling the morphology of the crystalline materials. At the nanoscale, the ability to control the size and shape of nanocrystals (NCs) in order to tune functional properties is an important goal. The precise fabrication of NCs with specific shapes at the nanoscale level is crucial for enhancing performance in many applications [14–16]. The techniques for nanomaterial synthesis are the pillars of nanoscience and nanotechnology [17, 18]. Nano- material syntheses can be fine-tuned to tailor the shape of the nanomaterials, which enables the application of nanomaterials in various fields, such as catalysis [19–21] electronics [22], optics [23], and magnetism [24] etc. Hence, developing a methodology for shape-controlled NC growth is a major current research direction.

It is well established that structural changes at surfaces, including atomic relaxation and reconstruction, are a manifestation of the driving force to minimize the surface energy [25, 26]. Such shape effects result inherently from the atomic arrangement of different exposed crystal facets, and the growth mode of an NC is determined by the ratio between the growth rates of different facets [27]. Recent studies have shown that the use of capping agents is a typical and efficient strategy to control morphology and size. The functional groups on these capping agents can preferentially adsorb onto the crystal facet and modulate the kinetics of crystal growth [28–30]. Maneuvering the surface energies and growth rates of different facets determines the shape of a NC [19, 31]. Shape control of crystal growth has been reported for various types of oxide materials by modulating the reactive conditions in the liquid phase [32, 33]. In particular, surface charges and polarization have been discussed in previous reports on the synthesis of nanomaterials with some novel morphologies [34, 35]. However, the synthesis of crystals with the desired morphologies requires an understanding of the thermo-dynamic and kinetic mechanisms of the formation of NCs and a framework to guide the selection of environmental conditions.

Even at the nanoscale, fine control over nanoparticle (NP) morphology (surface structure) has also been shown to induce superior catalytic reactivity and selectivity [36, 37]. It is also possible to discover new and potentially useful com- positions of matter on the nanoscale, because mixtures of elements that are thermodynamically unstable in the bulk may actually become stable (or metastable) as a result of quantum size-confinement effects [38, 39]. As Pauli said ‘God made the bulk; surfaces were invented by the devil’.

Identifying the mechanism of the morphological trans- formation of both nano- and micro-crystals is crucial to gain better control of the growth of materials because the surface structure can strongly affect the crystal quality and properties. The conventional understanding of the surface atomic structure of a crystal is that facets with a higher percentage of under-coordinated atoms are usually more reactive. Modulation of morphology is a commonly employed strategy to optimize the performance of various crystalline catalysts from noble metals to semiconductors [40–42]. The synthesis of highly active facets has been considered as an important procedure to significantly promote the catalytic activity of noble metals, metal oxides, and semiconductors [43–46]. In particular, the peculiar particle morphological structures of metals and their oxides, such as cube, flower-like, octahedron, and rod, have attracted wide attention in the field of electro- chemical device applications [47–49]. The basis of this strategy is that the surface atomic configuration and coordination control the reactivity and can be finely tuned by morphological control [50, 51]. The chemistry of diverse energy facets and the differences in the binding properties of the intermediates and/or products with such facets are additional determining factors in deciding the overall catalytic activity of the materials under operating conditions. However, many questions still remain because of the lack of conclusive evidence about the mechanisms that govern crystal facet modulation at the atomic level; as such, there is considerable scope for research. In this strategy, insights from theoretical calculations and experimental evidence can be integrated with each other to develop a simple model that can be used to better understand crystal facet modulation mechanisms at the atomic level.

First-principles investigations have been recognized as effective for studying the morphology and surface properties of a wide variety of crystals and NCs [52–54]. Our group has developed a working methodology, which has been applied to the study of different morphologies in different metal oxides such as SnO_2 [55–57], $PbMoO_4$ [58], and $CaWO_4$ [59]. The relative growth rates of crystal faces, which depend on

environmental conditions, cause transformations in crystal morphology because of the appearance and/or disappearance of faces. These transformations are due to the geometric constraints imposed by the crystal structure and are associated with the relative values of the surface energy of each face. In this context, Roca et al published some results about our simple way to use the theoretical morphology modulation in TiO_2 and α-Ag_2WO_4 [60, 61] nanocrystals in order to explain the surface energy changes observed in experimental conditions.

The main practical challenges of the present work can be summarized as follows: (i) prediction of different morphologies possible for a crystalline material, (ii) screening of relative values of surface energies to obtain desired morphologies, and (iii) target and control of crystal morphologies.

Theoretical procedures and computational methods

The task of predicting the morphology of crystals can be partially tackled if interest is limited to general knowledge about trends regarding bulk and surface energies (values and variations). The energetic interplay between surface energy and morphology can be identified. This section briefly presents the definition of surface energy and the Wulff construction, which are the most basic parameters and methods for predicting the equilibrium morphology of a crystal.

From the thermodynamic point of view, the equilibrium shape of a crystal is determined by the free energies of various facets, and can be calculated by the classic Wulff construction that minimizes the total surface free energy at a fixed volume [9]. The Wulff theorem provides a simple relationship between the surface energy, E_{surf}, of the (hkl) plane and its distance, rhkl, in the normal direction from the center of the crystallite. Later, the thermodynamic stability of the faceted and rounded shapes was revisited by Herring [10]. In the case when the morphology of a NC is known from microscopic observations, E_{surf} can be assessed iteratively by using the Wulff construction in the inverse fashion until the resulting shape matches the observed shape [11].

First-principles calculations were carried out using the density functional theory and implemented in the Vienna *ab initio* simulation package in order to find an ideal structure in vacuum [62, 63]. The Kohn–Sham equations were solved by means of the Perdew–Burke–Ernzerhof exchange-correlation functional [64] and the electron–ion interaction was described by the projector-augmented-wave pseudo potentials [62, 65]. The plane-wave expansion was truncated at a cut-off energy of 520eV, and the Brillouin zones were sampled through the Monkhorst-Pack special k-points grids. The calculations were done by considering slabs with thickness of up to ~20 Å. They are sufficient to reproduce bulk-like proper- ties at the center of the slabs, to obtain a careful description of the surfaces and to reach convergence on the corresponding energy surface values. A vacuum spacing of 15 Å is introduced in the z-direction so that the surfaces will not interact with each other. The positions of all atoms of the slab were allowed to relax, and the conjugated gradient energy minimization method was used to obtain relaxed systems, accomplished by requiring the forces experienced by each atom to be smaller than 0.01 eV $Å^{-1}$. E_{surf} is defined as the total energy per repeating cell of the slab (E_{slab}) minus the total energy of the perfect crystal per molecular unit (E_{bulk}) multiplied by the number of molecular units of the surface (n), divided by the surface area per repeating cell of the two sides of the slab, as following:

$$E_{Surf} = \frac{E_{slab} - nE_{bulk}}{2A}$$

The total-energy calculations are strictly valid only at zero temperature, and the entropic contribution can be taken into account by adding the computed full phonon density of states [66] or alternatively, in a simplified treatment, by inclusion of the most relevant vibration modes [67]. The crystal habits are principally determined by relative energies of the exposed planes, and entropy terms normally do not affect this ordering [68]. The entropic and pV contributions to the free energies change slightly throughout the condensed-phase species and in this type of calculation the entropic term is neglected [68–73]. Therefore, the difference between the Gibbs free energies can be approximated by the difference between the total energies from first-principles calculations [74–76].

Crystallite shape of any kind of materials can, in turn, be determined using the Wulff theorem and construction [9, 77] taking into accounts the surface energy values, implemented in the SOWOS program [13]. In this paper, this methodology was used for the morphology mapping of Ag, anatase TiO_2, $BaZrO_3$, and α-Ag_2WO_4 systems.

Several insightful review papers have reported experimental and theoretical calculations on the important aspects that govern crystal shape modulation in semiconductor and metal NPs [78–80]. In addition to the thermodynamic driving forces, kinetics also plays an important role in the

determination of the morphology under real growth conditions. In such a case, the approach developed by Chernov can be applied to predict the steady-state shapes of NCs [81], and different authors have developed strategies to calculate the velocity of facet growth [82, 83]. It was necessary, therefore, to develop a novel strategy to construct polyhedral structures and to especially address such structural issues.

Results and discussion

Ag. Noble metal NPs with defined structures and novel compositions are of great interest because of their potential applications in a broad range of industrially important processes [14, 84, 85]. Over the past decade, Ag NCs with a myriad of shapes (e.g., spheres, cubes, octahedrons, right bipyramids, bars, plates, rods, and wires) have been synthesized using various methods [86–88].

Recently, our research group reported the unprecedented real-time in situ observation of the growth process of silver metallic Ag filaments from an unstable α-Ag_2WO_4 crystal matrix when the crystal was subjected to electron irradiation from a transmission electron microscope (TEM) [89]. This is a striking result and the mechanism associated with the early events of the nucleation process of Ag has been studied in detail [90]. The crystal growth mechanism under electron beam irradiation observed in our work is completely free of additional agents, and the in situ TEM enables the visualization of growth of Ag NPs with planar resolution. However, an investigation of the reactions and crystal growth mechanism under electron beam irradiation can be very complicated and demands new studies [91].

An expanded image of the region around the electron driven Ag filament is illustrated in figure 1, where it is possible to identify the morphology of the Ag NC formed during the experiments. In addition, the observed NCs tend to aggregate into clusters that interact in close proximity, which implies the possible existence of an attractive force among the NCs [92, 93].

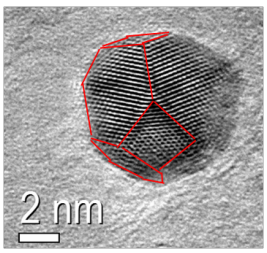

FIGURE 1 – TEM image of Ag NC formed under electron beam irradiation.

Thermodynamic calculations predict that single crystals of face-centered cubic materials such as Pt or Ag will form truncated octahedral shapes, with the ratio of their (111) [49], and (100) type surfaces predicted through consideration of the ratio of their two respective surface energies [94]. This ratio can be significantly and controllably modified through the use of surfactants, and it has been demonstrated to have a substantial effect on catalytic selectivity [36]. Particle morphology also dictates the nearest-neighbor coordinations of the exposed surface atoms, broadly affecting the catalytic activity [95].

The morphological characterization of Ag NPs has shown strong correlations between properties such as average particle size, shape, and dispersity with observed and inherently tunable physiochemical behavior [96, 97]. In this con- text, Barnard et al [98] have presented detailed structure/ property maps, showing that faceted near-spherical shapes and spheres are the predominant morphologies in Ag NPs colloidal samples at low and high temperatures. The production of well-defined NPs with reproducible size and shape distributions remains challenging [99], although different studies report clarification of stability, probability, and population in NP ensembles [100]. The (100), (110), and (111) surfaces were modeled by unreconstructed (truncated bulk) slab models by using a calculated equilibrium geometry and using a (6 × 6 × 1) Monkhorst-Pack special k-points grid to ensure geometrical and energetic convergence for the Ag structures considered. Slab models containing 15 Ag atoms placed in 3 five-atomic layers were selected, with areas of 8.77 $Å^2$, 12.4 $Å^2$, and 7.59 $Å^2$ for the (100), (110), and (111) surfaces, respectively. Figure 2 depicts the slab representation for Ag.

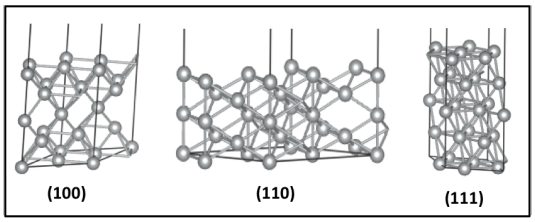

FIGURE 2 – Surface models of (100), (110), and (111) for Ag.

An analysis of figure 3 shows that the calculated energy surface values (center of figure 3) generate a morphology very similar to that of synthesized Ag NCs, generated by matching the corresponding TEM image (see figure 1). When the difference in the stability of the facets is reduced, more than one type of facet will appear, and the resulting polyhedron should gradually appear rounder, with truncated edges and corners.

When the ratio of the energy surface is varied by increasing the value of the (111) surface more than 22% because of some perturbation, the resulting morphology is a double truncated octahedron. The same morphology is obtained by decreasing the value of the (110) and (011) surfaces more than 24% with respect to the computed initial value. On the other hand, a truncated cube or a truncated octahedron can be achieved when the value of the (100) and (001) surfaces is decreased by around 42% or is increased by around 20%, respectively. In addition, using the different morphologies displayed in figure 3, we can rationalize some experimental results reported very recently by Wang et al [101] such as the formation of Ag nanocubes and octahedra.

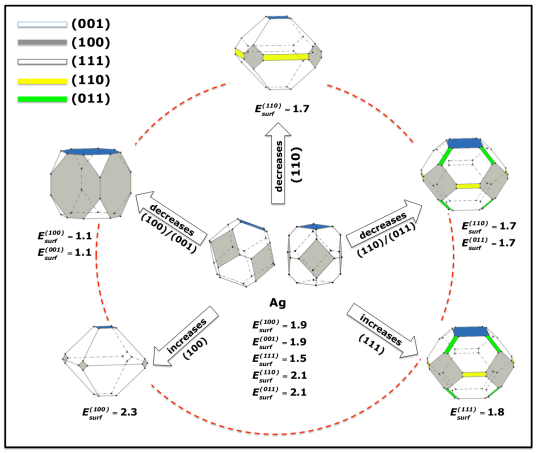

FIGURE 3 – Crystallographic structure and map of morphologies of Ag NC with (100), (001), (111), (110), and (011) crystal planes. Surface energy is in joule per·square meter. Theoretical (experimental) [102] lattice parameter, a = 4.188 Å (4.086 Å).

Anatase TiO_2. The morphology as well as the crystal-facet-controlled synthesis of titanium dioxide (TiO_2) has attracted interest because of its scientific and technological applications, including in photocatalysts and self-cleaning agents [103].

TiO_2 is a common multifunctional material, which has been used in a wide variety of applications in many fields, such as in ceramics, cosmetics, medicine, food, and catalysts [104]. For TiO_2, three polymorphs are stable at atmospheric pressure: the thermodynamically favored rutile phase that can be grown in bulk, and the less common anatase and brookite phases. The polymorphs have significantly different chemical reactivities with anatase and brookite typically being believed to be the most reactive. Hence, many researchers have pursued polymorph-specific syntheses of high-reactivity NCs [105]. Anatase TiO_2 was proven to be more active than the other two main TiO_2 crystal polymorphs, i.e., rutile and brookite, especially when TiO_2 is employed as a catalyst and photocatalyst [50, 106].

Under equilibrium conditions, natural and synthetic anatase TiO_2 single crystals mainly exist in an octahedral bipyramidal morphology in which a majority of the surface is normally enclosed by energetically favorable (101) facets rather than the more reactive (001) facets [107–109]. Thus, it has long been a great challenge to synthesize anatase TiO_2 with a large fraction of exposed (001) facets. However, recently, many studies have reported the synthesis of high-energy anatase surfaces [42, 110, 111].

Despite intense investigations into the preparation of specific facets, the inherent photoactivities of TiO_2 facets are still ambiguous. The (001) facet was initially expected to be the most active because of its high surface energy [42, 112– 115], whereas later research suggested that the clean (010) facet with 100% five-coordinate Ti was more active in photo- oxidation and photoreduction reactions [116]. In particular, Liu *et al* reported that the photoreactivity of (010) facets of TiO_2 is higher than that of the (101) facets, while the (001) facets showed the lowest photoreactivity [116]. However, more recent research has suggested that different facets may play different roles in photoreaction [117, 118].

Based on first-principles calculations, the E_{surf} values for (101), (001), (110), and (100) facets of anatase TiO_2 were determined, using a (4 × 4 × 1) Monkhorst-Pack special k-points grid. Slab models containing 12, 14, 24, and 16 molecular units with areas of 14.5 $Å^2$, 19.4 $Å^2$, 35.9 $Å^2$ and 25.4 $Å^2$ for the (001), (101), (100), and (110) surfaces, respectively. It is worth noting that the (001) and (101) surfaces are O-terminated, while the (100) and (110) surfaces are Ti and O-terminated. Figure 4 depicts the slab representation for anatase TiO_2. Each surface has been modeled using stoichiometric systems [119].

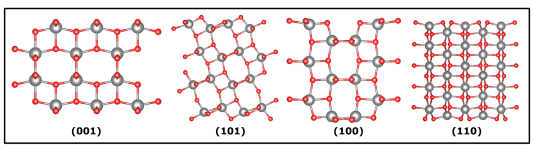

FIGURE 4 – Surface models of (001), (101), (100), and (110) for anatase TiO_2. The red and gray atoms represent O and Ti atoms, respectively.

The E_{surf} values and the Wulff construction of the ideal structure for anatase TiO_2 in vacuum are shown in figure 5. It is possible to determine which structure should be present in anatase TiO_2 by calculating the mathematical relationships with the E_{surf} values if a few facets are more stable than others. The Wulff

constructions of those structures are also shown in figure 5.

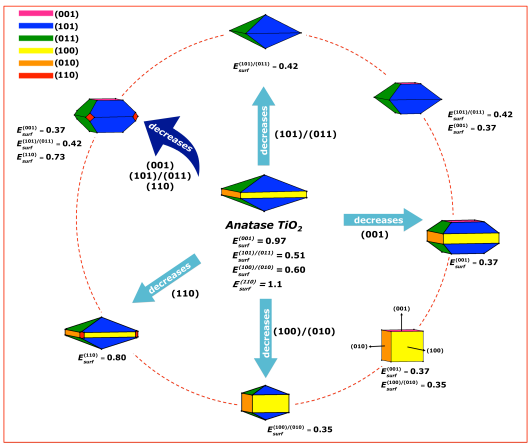

FIGURE 5 – Crystallographic structure and map of morphologies of anatase TiO_2 with crystal planes (001), (101), (011), (100), (010), and (110). Surface energy is in joule per·square meter. Theoretical (experimental) [120] lattice parameters, a = 3.806 Å (3.78 Å), c = 9.722 Å (9.51 Å).

Figure 5 can be used as a tool to verify the relative value of E_{surf} that is necessary to obtain a particular morphology. Many research groups have studied anatase TiO_2 with various shapes, such as single particle, nanosheet, cube, film, and flowerlike shapes [112–114].

Theoretical results reported by Barnard *et al* [121] point out the effect of water on the morphology of anatase and rutile TiO_2. For anatase TiO_2, the presence of water resulted in a variation in the size of the (001) facets. In another paper, Barnard and Curtiss [107] show the influence of acidic and alkaline conditions on the morphology of TiO_2. The morphology shows a high occurrence of (100)/(010) facets that predominantly occur in hydrogen-poor and oxygenated conditions. We obtained the surface energies of these shape- decreasing (100)/(010) facets.

Some experimental results reported recently by Pan et al show an elongated, truncated tetragonal bipyramid anatase with highly exposed (010) facets that was also synthesized by tuning the Ti/F ratio [116]. This morphology was obtained by decreasing the (100)/(010) surface energy of the initial Wulff construction on the map.

The cube shape is obtained by decreasing the (001) and (100)/(010) surface energy and was synthetized solvothermally by Zhao *et al* [111]. A scanning electron microscopy (SEM) image of anatase TiO_2 particle synthesized by microwave-assisted hydrothermal method and its respective Wulff crystal is shown in figure 6.

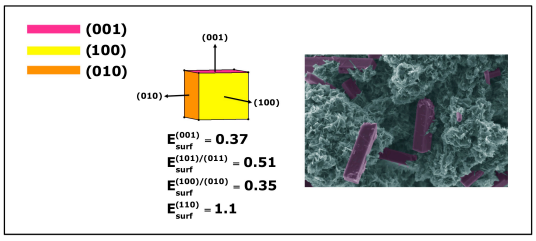

FIGURE 6. SEM image of cubic anatase TiO_2 particle and its Wulff crystal representation. Surface energy is in joule per·square meter.

Even that the TiO_2 particles showed in figure 6 have the same surfaces of the cubic morphology, they present a more elongated shape. This represents lower values of (100)/ (010) in relation of (001) surface. According to the Wulff theorem, the larger the difference is, the higher is this elongation.

Decreasing the (101)/(011) and (001) surface energy, we obtained the morphology synthesized by Yang et al that shows a breakthrough in synthesizing a truncated tetragonal bipyramid anatase TiO_2 by fluorine capping, resulting in highly exposed (001) facets [42].

The octahedral structure was obtained by Amano et al using the hydrothermal reaction to synthetize a morphology with (101) facet [122]. The morphology with (001), (101), and (110) facets, as seen in the map, was obtained by Liu et al, which was synthesized using a modified hydrothermal technique in the presence of hydrogen peroxide and hydro- fluoric acid solution [123].

$BaZrO_3$. Barium zirconate ($BaZrO_3$) is a cubic perovskite at normal conditions, exhibiting a unique set of properties such as a high melting point, a small thermal expansion coefficient, small thermal conductivity, and excellent thermal and chemical stability [124]. These properties lead to the use of $BaZrO_3$ in structural applications such as crucibles [125], thermal barrier coatings [126], components in wireless communication systems, the supersonic aircraft industry, and field emission displays, and it is also used as a green photocatalyst [127].

E_{surf} of a plane is highly sensitive to the surface composition, impurities, and distortions/defects of a crystal. When an atom or foreign species becomes adsorbed on one surface or plane, it can decrease/increase the surface energy of that plane and may even stabilize/destabilize it with respect to other planes. Because of this adsorption, anisotropy is created in the surface energies, and this may be responsible for a change in the overall shape of the crystal with the original surface energy plane

appearing/disappearing at the surface of the crystal. Traditionally, KOH (as a mineralizer) has often been used to provide an OH^- environment in the hydrothermal crystallization process of ABO_3 perovskite [128]. Morphology changes can also be accomplished by adding impurities/dopants to the system. The dopants act in a different way with respect to the changes in the energy order of the facets, according to the impurity species and their quantity [129].

Calculations for $BaZrO_3$ bulk and surfaces were performed using Monkhorst-Pack special k-points grids (3 × 3 × 1) to ensure geometrical and energetic convergence for the $BaZrO_3$ structures considered in this work. The (001), (011), and (111) facets are modeled using stoichiometric systems. Slab models containing 6, 8, and 9 molecular units for (001), (011), and (111) surfaces, respectively, were considered, with areas of 18.1 $Å_2$, 25.5 $Å^2$, and 31.3 $Å^2$, respectively. It is worth noting that the stoichiometric (001), (011), and (111) surfaces are BaO and ZrO_2 terminated, O_2 and BaZrO-terminated, and BaO_3 and Zr-terminated, respectively, as illustrated in figure 7.

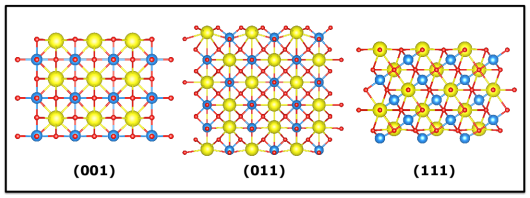

FIGURE 7 – Surface models of (001), (011), and (111) surfaces for $BaZrO_3$. The Ba, Zr, and O atoms are shown in yellow, blue, and red, respectively.

Figure 8 presents the Wulff´s crystal of the obtained $BaZrO_3$ results. Figure 8 also shows all the possible morphologies that can be obtained by varying the ratio between the E_{surf}, taking into account the (001), (011), and (111) surfaces.

The variation in surface energy using the Wulff construction can be used as a powerful tool to evaluate the morphology of particles because of the difficulty in simulating all the details in a reaction system that interacts with the surface. A SEM image of a $BaZrO_3$ particle synthesized by microwave-assisted hydrothermal method and its respective Wulff crystal is shown in figure 9.

Based on this result, it is possible to determine the relative energy values of each surface in order to obtain the experimental results. Besides the deca-octahedral morphology, Nakashime *et al* [131] reported cubic particles of $BaZrO_3$ synthesized by a composite-hydroxide-mediated approach at low temperature. Moreira et al [132] also showed a coexistence of cubic and deca-octahedral $BaZrO_3$ particles obtained by the microwave assisted hydrothermal method. These cases of cubic particles are in agreement with the ideal state (see figure 8).

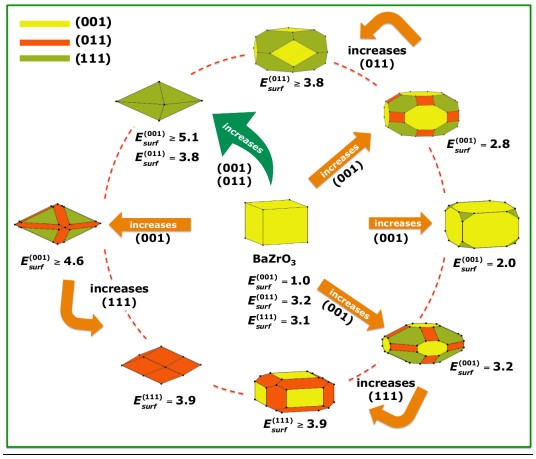

FIGURE 8 – Crystallographic structure and map of morphologies of $BaZrO_3$ with (001), (011), and (111) crystal planes. Surface energy is in joule per·square meter. Theoretical (experimental) [130] lattice parameter, a = 4.251 Å (4.18 Å).

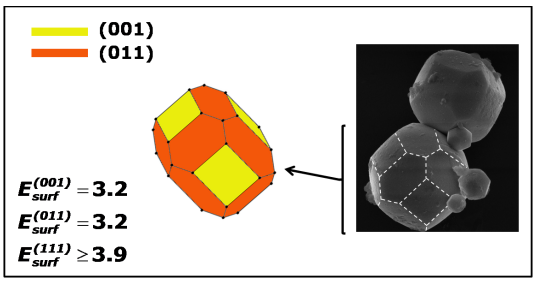

FIGURE 9 – SEM image of deca-octahedral $BaZrO_3$ crystals and its Wulff crystal representation. Surface energy is in joule per·square meter.

α-Ag_2WO_4. Transition metal tungstates are important inorganic materials that are studied and applied widely in many fields [133]. Among these, Ag_2WO_4 has attracted considerable attention because of their potential applications in fields as ionic conductivity [134], photocatalysis [135], sensors [136], microbial agents [137], photoluminescence properties [137, 138].

Ag_2WO_4 has three different crystallographic forms, α-, β-, and γ-Ag_2WO_4, among which α-Ag_2WO_4 is the thermodynamically stable phase that has been investigated [138]. To date, various methods of synthesis such as controlled precipitation [139], hydrothermal [140], and microwave- assisted method [89] have been reported in literature to obtain different Ag_2WO_4 nanostructures.

The (100), (010), (001), (110), (101), and (011) surfaces of α-Ag_2WO_4 were modeled by

unreconstructed slab models using a calculated equilibrium geometry and using a (3 × 3 × 1) Monkhorst-Pack special k-points grid. Slab models containing 8, 8, 16, 10, 9, and 16 molecular units for (100), (010), (001), (110), (101), and (011) surfaces, respectively, were considered, with areas of 68.6 $Å^2$, 64.1 $Å^2$, 132.5 $Å^2$, 93.9 $Å^2$, 149.2 $Å^2$, and 147.2 $Å^2$, respectively. It is worth noting that the (010), (100), (101), and (011) surfaces are O and Ag-terminated, while the (001) and (110) surfaces are O, W, and Ag-terminated. The slab representations are shown in figure 10.

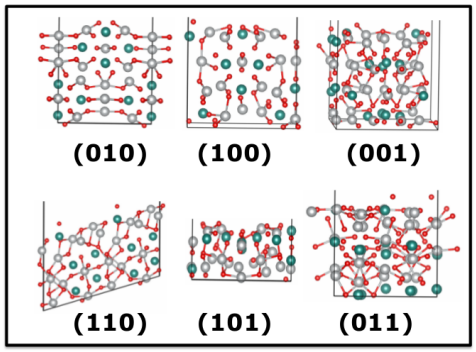

FIGURE 10 – Surface models of (010), (100), (001), (110), (101), and (011) for α-Ag_2WO_4. The Ag, W, and O atoms appear in grey, blue, and red, respectively.

Figure 11 presents the Wulff's crystal of the optimized α-Ag_2WO_4 and the different morphologies that would be obtained assuming different surface energy ratios. An analysis of figure 11 shows that the calculated energy surface values (ideal) generate a prism shape. The ratio of the energy surface has been varied by increasing the value of the more stable surfaces (left in figure 11) and by decreasing the value of the less stable surfaces (right in figure 11).

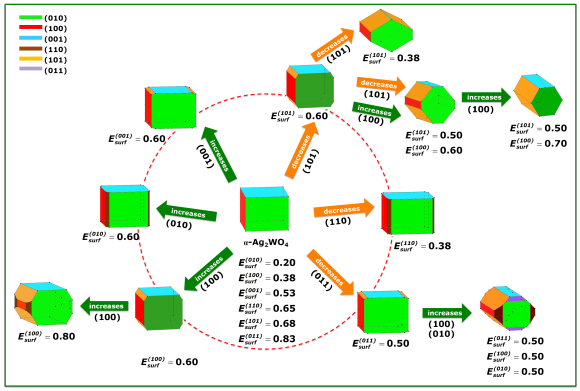

FIGURE 11 – Crystallographic structure and map of morphologies of α-Ag_2WO_4 with crystal planes (010), (100), (001), (110), (101), and (011). Surface energy is in joule per·square meter. Theoretical (experimental) [138] lattice parameters, *a* = 11.126 Å (10.87 Å), *b* = 11.907 Å (12.01 Å), *c* = 5.761 Å (5.89 Å).

A SEM image of α-Ag_2WO_4 particle synthesized by microwave-assisted hydrothermal method and its respective Wulff crystal is shown in figure 12. Besides this image, experimental results reported recently by Roca *et al* [60] show the same hexagonal rod-like shape under certain condition. Assuming the ideal structure as a starting-point, this morphology can be theoretically obtained increasing (101) and (100) surface energy to 0.5 J/m^2 and 0.7 J/m^2, respectively.

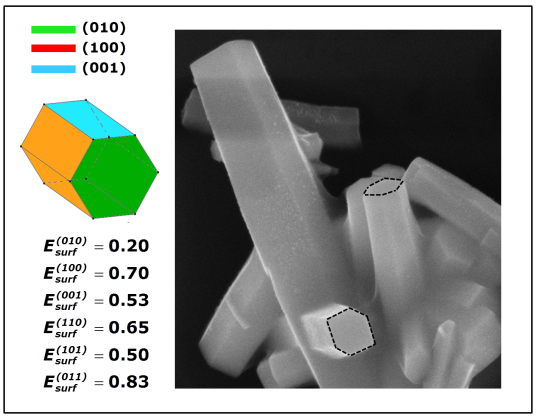

FIGURE 12 – SEM image of α-Ag_2WO_4 crystals and its Wulff crystal representation. Surface energy is in joule per·square meter.

In summary, the mechanism of the morphology transformation of α-Ag_2WO_4 crystals controlled by surface chemistry has been investigated experimentally and theoretically. The selection of surfaces to investigate was limited to low-index surfaces and surfaces with experimental observations were preferred.

Conclusions

The surface is a key component of a solid-state material, as many physical and chemical processes take place on surfaces. A series of materials that includes metal (Ag), simple (anatase TiO_2), and complex ($BaZrO_3$ and α-Ag_2WO_4) metal oxides with fascinating polyhedral morphologies such as octahedral, cuboctahedral, and truncated cubic structures were obtained. A controlled structural transformation between polyhedra is an essential goal of crystal engineering strategies. This framework is envisaged to provide guidelines for the synthesis of crystals of desired morphologies. The main conclusions can be summarized as follows: (i) We successfully demonstrate the morphological modulation of three-dimensional NCs. (ii) Based on the reverse Wulff theorem, we demonstrated that the structural transformations among different morphologies were easily controlled by the relative values of surface energies. (iii) By a proper adjustment of the ratio of the values for the surface energy of

different facets, we are capable of finding a given morphology. This strategy will contribute to a better understanding of the control of morphological characteristics in nano- and micro-crystals. (iv) In the case of Ag and $BaZrO_3$, it was applied a combination of experimental data, obtained from images taken by high- resolution TEM and SEM, respectively, and the calculated surface energies for the three-dimensional Wulff construction. (v) This research will lay the foundations of not only unequivocal shape determination, but also an in-depth understanding of the observed features during the synthesis at the atomic level to help facilitate further breakthroughs in the control of crystal morphology.

Results presented here are an illustration of how first-principles calculations are capable of rationalizing the mechanisms stabilizing the morphology of micro- and nano-particles at the atomic level. Using the present method, a 3D platform for the morphology modulation of materials with a complete array of accessible morphologies is obtained. We believe that our work has both predictive and explanatory capabilities, and it can be of help in the refinement of both research and technological developments to gain further understanding of how to achieve morphological control of complex three-dimensional crystals from metals to metal oxides.

Acknowledgment

The authors are grateful to FAPESP (2013/07296-2, 2012/ 14468-1, 2013/26671-9 and 2014/04350-9), CAPES (process A104/2013 and 99999.002998/2014-09), CNPq INCTMN 573636/2008-7, PrometeoII/2014/022 and ACOMP/2014/270 projects (Generalitat Valenciana), Ministerio de Economia y Competitividad (Spain), CTQ2012-36253-C03-02 and the Spanish Brazilian program (PHB2009-0065-PC) for financially supporting this research. We also acknowledge the Servei Informática, Universitat Jaume I for a generous allotment of computer time.

References

[1] Kong X Y, Ding Y, Yang R and Wang Z L 2004 Science 303 1348–51
[2] Huang S et al 2012 Dalton Trans. 41 5634–42
[3] Wang L and Li Y 2007 Chem. Mater. 19 727–34
[4] Zhai T et al 2009 Adv. Funct. Mater. 19 2423–30
[5] Flytzani-Stephanopoulos M and Schmidt L D 1979 Prog. Surf. Sci. 9 83–111
[6] Zhao X et al 2008 Funct. Mater. Lett. 01 167–72
[7] Sun C and Xue D 2014 Cryst. Growth Des. 14 2282–7
[8] Chen K, Sun C and Xue D 2015 Phys. Chem. Chem. Phys. 17 732–50
[9] Wulff G 1901 Z. Kristallogr. 34 449–530
[10] Herring C 1951 Phys. Rev. 82 87–93
[11] Roosen A R, McCormack R P and Carter W C 1998 Comput. Mater. Sci. 11 16–26
[12] Zucker R V, Chatain D, Dahmen U, Hagege S and Carter W C 2012 J. Mater. Sci. 47 8290–302
[13] Scopece D 2013 J. Appl. Crystallogr. 46 811–6
[14] Burda C, Chen X, Narayanan R and El-Sayed M A 2005 Chem. Rev. 105 1025–102
[15] Dahl J A, Maddux B L S and Hutchison J E 2007 Chem. Rev. 107 2228–69
[16] Lu A-H, Salabas E L and Schüth F 2007 Angew. Chem., Int. Ed. 46 1222–44
[17] Murray C B, Kagan C R and Bawendi M G 2000 Annu. Rev. Mater. Sci. 30 545–610
[18] Sun S, Murray C B, Weller D, Folks L and Moser A 2000 Science 287 1989–92
[19] Xia Y, Xiong Y, Lim B and Skrabalak S E 2009 Angew. Chem., Int. Ed. 48 60–103
[20] KangY,PyoJB,YeX,GordonTRandMurrayCB2012 ACS Nano 6 5642–7
[21] Kang Y et al 2012 ACS Nano 7 645–53
[22] Peng X et al 2000 Nature 404 59–61
[23] Ye X et al 2010 Proc. Natl Acad. Sci. USA 107 22430–5
[24] Song Q, Ding Y, Wang Z L and Zhang Z J 2006 J. Phys. Chem. B 110 25547–50
[25] Somorjai G A 1981 Chemistry in Two Dimensions: Surfaces (Ithaca, NY: Cornell University Press)
[26] ZangwillA1988PhysicsatSurfaces(Cambridge:Cambridge University Press)
[27] Wang Z L 2000 J. Phys. Chem. B 104 1153–75
[28] Zhang G et al 2010 Appl. Surf. Sci. 257 302–5
[29] Di W, Willinger M-G, Ferreira R A S, Ren X, Lu S and Pinna N 2008 J. Phys. Chem. C 112 18815–20
[30] Yajuan S et al 2007 Nanotechnology 18 275609
[31] Xia Y, Xiong Y, Lim B and Skrabalak S E 2009 Angew. Chem. 121 62–108
[32] Wen H et al 2008 J. Phys. Chem. C 112 15948–55
[33] LiZ, LaiX, Wang H, Mao D, Xing Cand Wang D 2009 Nanotechnology 20 245603
[34] Jian J K et al 2007 J. Cryst. Growth 303 427–32
[35] Wang H et al 2010 J. Am. Chem. Soc. 132 15875–7
[36] Bratlie K M, Lee H, Komvopoulos K, Yang P and Somorjai G A 2007 Nano Lett. 7 3097–101
[37] Narayanan R and El-Sayed M A 2004 Nano Lett. 4 1343–8
[38] FerrandoR,JellinekJandJohnstonRL2008Chem.Rev.108 845–910
[39] Buhro W E and Colvin V L 2003 Nat. Mater. 2 138–9
[40] Lim B et al 2009 Science 324 1302–5
[41] Xie X, Li Y, Liu Z-Q, Haruta M and Shen W 2009 Nature 458 746–9
[42] Yang H G et al 2008 Nature 453 638–41
[43] Joo J, Chow B Y, Prakash M, Boyden E S and Jacobson J M 2011 Nat. Mater. 10 596–601
[44] Jiang H B et al 2011 Angew. Chem., Int. Ed. 50 3764–8
[45] Dong J J et al 2011 ACS Appl. Mater. Interfaces 3 4388–95
[46] Kiatkittipong K, Scott J and Amal R 2011 ACS Appl. Mater. Interfaces 3 3988–96
[47] Maiyalagan T, Chemelewski K R and Manthiram A 2013 ACS Catal. 4 421–5
[48] Duan J, Chen S, Dai S and Qiao S Z 2014 Adv. Funct. Mater. 24 2072–8
[49] Yang W et al 2013 Electrochem. Commun. 28 13–6
[50] De Angelis F, Di Valentin C, Fantacci S, Vittadini A and Selloni A 2014 Chem. Rev. 114 9708–53
[51] Mudunkotuwa I A and Grassian V H 2011 J. Environ. Monit. 13 1135–44
[52] Karim A, Fosse S and Persson K A 2013 Phys. Rev. B 87 075322
[53] Kanaki E, Gohr S, Mueller C and Paulus B 2015 Surf.

Sci. 632 158–63
[54] Barmparis G D, Lodziana Z, Lopez N and Remediakis I N 2015 Beilstein J. Nanotechnol. 6 361–8
[55] Beltrán A, Andrés J, Longo E and Leite E R 2003 Appl. Phys. Lett. 83 635–7
[56] Leite E R, Giraldi T R, Pontes F M, Longo E, Beltrán A and Andrés J 2003 Appl. Phys. Lett. 83 1566–8
[57] Stroppa D G et al 2014 Phys. Chem. Chem. Phys. 16 1089–94 [58] Bomio M R D et al 2013 J. Phys. Chem. C 117 21382–95
[59] Longo V M et al 2011 J. Phys. Chem. C 115 20113–9
[60] Roca R A et al 2015 Catal. Sci. Technol. 5 4091–107
[61] Roca R A and Leite E R 2013 J. Am. Ceram. Soc. 96 96–102
[62] Kresse G and Furthmuller J 1996 Comput. Mater. Sci. 6 15–50
[63] Kresse G and Hafner J 1994 Phys. Rev. B 49 14251–69
[64] Perdew J P, Burke K and Ernzerhof M 1996 Phys. Rev. Lett. 77 3865–8
[65] Kresse G and Joubert D 1999 Phys. Rev. B 59 1758–75
[66] Heid R, Pintschovius L, Reichardt W and Bohnen K P 2000 Phys. Rev. B 61 12059–62
[67] McBride J R, Hass K C and Weber W H 1991 Phys. Rev. B 44 5016–28
[68] Baetzold R C and Yang H 2003 J. Phys. Chem. B 107 14357–64
[69] Barnard A S and Zapol P 2004 J. Chem. Phys. 121 4276–83
[70] Chizallet C et al 2008 J. Phys. Chem. C 112 16629–37
[71] Zasada F et al 2011 J. Phys. Chem. C 115 6423–32
[72] Vittadini A, Casarin M and Selloni A 2009 J. Phys. Chem. C 113 18973–7
[73] Rogal J, Reuter K and Scheffler M 2004 Phys. Rev. B 69 075421
[74] Lodziana Z, Topsoe N-Y and Norskov J K 2004 Nat. Mater. 3 289–93
[75] Selçuk S and Selloni A 2013 J. Phys. Chem. C 117 6358–62
[76] Wang Y et al 2014 Phys. Rev. B 90 045304
[77] Rusanov A I 2005 Surf. Sci. Rep. 58 111–239
[78] Seyed-Razavi A, Snook I K and Barnard A S 2010 J. Mater. Chem. 20 416–21
[79] Jiang Z-Y, Kuang Q, Xie Z-X and Zheng L-S 2010 Adv. Funct. Mater. 20 3634–45
[80] Lee K, Kim M and Kim H 2010 J. Mater. Chem. 20 3791–8
[81] Chernov A A 1963 Sov. Phys. Crystallogr. 7 728–30
[82] Sun Q, Yerino C D, Leung B, Han J and Coltrin M E 2011 J. Appl. Phys. 110 053517
[83] Romanyuk K, Cherepanov V and Voigtländer B 2007 Phys. Rev. Lett. 99 126103
[84] Gross E, LiuJack H-C, Toste F D and Somorjai G A 2012 Nat. Chem. 4 947–52
[85] Heveling J 2012 J. Chem. Educ. 89 1530–6
[86] Rycenga M et al 2011 Chem. Rev. 111 3669–712
[87] Zhang J, Li S, Wu J, Schatz G Cand Mirkin C A 2009 Angew. Chem., Int. Ed. 48 7787–91
[88] Xia X, Zeng J, Zhang Q, Moran C H and Xia Y 2012 J. Phys. Chem. C 116 21647–56
[89] Longo E et al 2013 Sci. Rep. 3 1676
[90] Andrés J et al 2014 Sci. Rep. 4 5391
[91] Woehl T J, Park C, Evans J E, Arslan I, Ristenpart W D and Browning N D 2013 Nano Lett. 14 373–8
[92] Li D, Nielsen M H, Lee J R I, Frandsen C, Banfield J F and De Yoreo J J 2012 Science 336 1014–8
[93] Batson P E, Reyes-Coronado A, Barrera R G, Rivacoba A, Echenique P M and Aizpurua J 2011 Nano Lett. 11 3388–93
[94] Elechiguerra J L, Reyes-Gasga J and Yacaman M J 2006 J. Mater. Chem. 16 3906–19
[95] Rashkeev S N, Lupini A R, Overbury S H, Pennycook S J and Pantelides S T 2007 Phys. Rev. B 76 035438
[96] Arumugam S K, Sastry T P, Sreedhar B and Mandal A B 2007 J. Biomed. Mater. Res. A 80A 391–8
[97] Yu A K, Kudrinskiy A A, Olenin A Y and Lisichkin G V 2008 Russ. Chem. Rev. 77 233
[98] González A L, Noguez C, Beránek J and Barnard A S 2014 J. Phys. Chem. C 118 9128–36
[99] Sau T K and Rogach A L 2012 Complex-Shaped Metal Nanoparticles: Bottom-Up Syntheses and Applications (Weinheim: Wiley)
[100] Barnard A S 2014 Nanoscale 6 9983–90
[101] Wang Y, He J, Liu C, Chong W H and Chen H 2014 Angew. Chem., Int. Ed. 53 2–32
[102] Spreadborough J and Christian J W 1959 J. Sci. Instrum. 36 116–8
[103] Chen D and Caruso R A 2013 Adv. Funct. Mater. 23 1356–74
[104] Liu L and Chen X 2014 Chem. Rev. 114 9890–918
[105] Bourikas K, Kordulis C and Lycourghiotis A 2014 Chem. Rev. 114 9754–823
[106] Diebold U 2003 Surf. Sci. Rep. 48 53–229
[107] Barnard A S and Curtiss L A 2005 Nano Lett. 5 1261–6
[108] Yang H G and Zeng H C 2004 J. Phys. Chem. B 108 3492–5 [109] Gong X-Q and Selloni A 2005 J. Phys. Chem. B 109 19560–2
[110] WenCZ,ZhouJZ,JiangHB,HuQH,QiaoSZand Yang H G 2011 Chem. Commun. 47 4400–2
[111] Zhao X et al 2011 Adv. Funct. Mater. 21 3554–63
[112] Wang Y, Zhang H, Han Y, Liu P, Yao X and Zhao H 2011 Chem. Commun. 47 2829–31
[113] Dinh C-T, Nguyen T-D, Kleitz F and Do T-O 2009 ACS Nano 3 3737–43
[114] WenCZ,HuQH,GuoYN,GongXQ,QiaoSZand Yang H G 2011 Chem. Commun. 47 6138–40
[115] Xiang Q, Yu J, Wang W and Jaroniec M 2011 Chem. Commun. 47 6906–8
[116] Pan J, Liu G, Lu G Q and Cheng H-M 2011 Angew. Chem., Int. Ed. 50 2133–7
[117] D'Arienzo M et al 2011 J. Am. Chem. Soc. 133 17652–61
[118] Tachikawa T, Yamashita S and Majima T 2011 J. Am. Chem. Soc. 133 7197–204
[119] Bandura A V, Evarestov R A and Kuruch D D 2010 Surf. Sci. 604 1591–7
[120] Moura K F et al 2014 J. Solid State Chem. 210 171–7
[121] Barnard A S, Zapol P and Curtiss L A 2005 J. Chem. Theory Comput. 1 107–16
[122] Amano F, Yasumoto T, Prieto-Mahaney O-O, Uchida S, Shibayama T and Ohtani B 2009 Chem. Commun. 17 2311–3
[123] Liu M et al 2010 Chem. Commun. 46 1664–6
[124] Kumar H P et al 2008 J. Alloys Compd. 458 528–31
[125] Dierickx D, Houben I, Lapin J, Delannay F and Van Der Biest O 1996 J. Mater. Sci. Lett. 15 1573–6
[126] Pan L, Li L and Chen Y 2013 J. Sol-Gel Sci. Technol. 66 330–6
[127] Yuan Y et al 2008 Int. J. Hydrogen Energy 33 5941–6
[128] Wang D et al 2002 Solid State Ion. 151 329–33
[129] Alfredsson M et al 2007 Surf. Sci. 601 4793–800
[130] Moreira M L, Andres J, Varela J A and Longo E 2009 Cryst. Growth Des. 9 833–9

[131] Nakashima K, Fujii I and Wada S 2011 J. Ceram. Soc. Japan 119 532–4
[132] Moreira M L et al 2011 Scr. Mater. 64 118–21
[133] YuSH,LiuB,MoMS,HuangJH,LiuXMandQianYT 2003 Adv. Funct. Mater. 13 639–47
[134] Suthanthiraraj S A and Sarojini S 2012 Chem. Sci. Trans. 1 13–22
[135] Tang J and Ye J 2005 J. Mater. Chem. 15 4246–51
[136] da Silva L F et al 2014 Nanoscale 6 4058–62
[137] Longo V M et al 2014 J. Phys. Chem. A 118 5769–78
[138] Cavalcante L S et al 2012 Inorg. Chem. 51 10675–87
[139] WangX,LiS,YuHandYuJ2011J.Mol.Catal.A33452–9
[140] Liu X et al 2013 Mater. Lett. 91 129–32

2.3 – Modeling the atomic-scale structure, stability, and morphological transformations in the tetragonal phase of $LaVO_4$

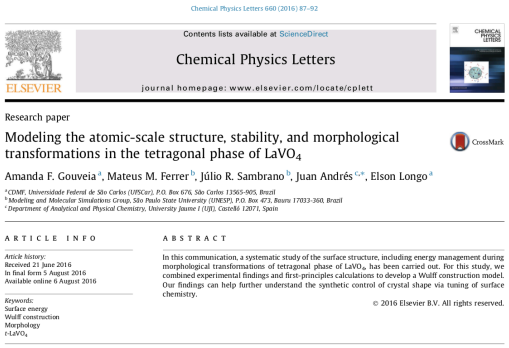

Chemical Physics Letters 660 (2016) 87–92

Contents lists available at ScienceDirect

Chemical Physics Letters

journal homepage: www.elsevier.com/locate/cplett

Research paper

Modeling the atomic-scale structure, stability, and morphological transformations in the tetragonal phase of $LaVO_4$

Amanda F. Gouveia [a], Mateus M. Ferrer [b], Júlio R. Sambrano [b], Juan Andrés [c,*], Elson Longo [a]

[a] CDMF, Universidade Federal de São Carlos (UFSCar), P.O. Box 676, São Carlos 13565-905, Brazil
[b] Modeling and Molecular Simulations Group, São Paulo State University (UNESP), P.O. Box 473, Bauru 17033-360, Brazil
[c] Department of Analytical and Physical Chemistry, University Jaume I (UJI), Castelló 12071, Spain

ARTICLE INFO

Article history:
Received 21 June 2016
In final form 5 August 2016
Available online 6 August 2016

Keywords:
Surface energy
Wulff construction
Morphology
t-$LaVO_4$

ABSTRACT

In this communication, a systematic study of the surface structure, including energy management during morphological transformations of tetragonal phase of $LaVO_4$ has been carried out. For this study, we combined experimental findings and first-principles calculations to develop a Wulff construction model. Our findings can help further understand the synthetic control of crystal shape via tuning of surface chemistry.

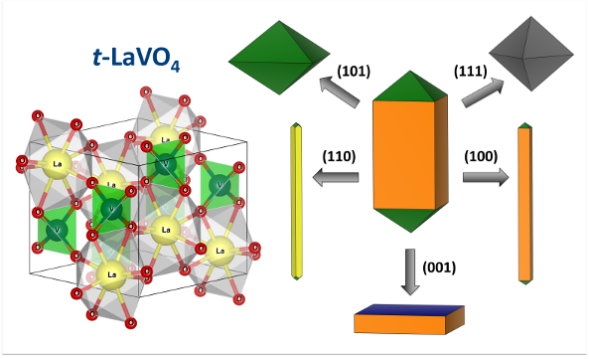

Modeling the atomic-scale structure, stability, and morphological transformations in the tetragonal phase of $LaVO_4$

Amanda F. Gouveia[a], Mateus M. Ferrer [b], Júlio R. Sambrano[b], Juan Andrés[c]*, and Elson Longo[a]

[a]*CDMF, Universidade Federal de São Carlos (UFSCar), P.O. Box 676, São Carlos 13565-905, Brazil.*

[b]*Modeling and Molecular Simulations Group, São Paulo State University (UNESP), P.O. Box 473, Bauru 17033-360, Brazil.*

[c]*Department of Analytical and Physical Chemistry, University Jaume I (UJI), Castelló 12071, Spain.*

In this communication, a systematic study of the surface structure, including energy management during morphological transformations of tetragonal phase of $LaVO_4$, has been carried out. For this study, we combined experimental findings and first-principles calculations to develop a Wulff construction model. Our findings can help further understand the synthetic control of crystal shape via tuning of surface chemistry.

Introduction

The phrase ‘‘structure dictates function” is an established dictum from the field of biology that is now recognized in materials science [1]. In particular, the interplay between the surface structure and morphology of materials and nanomaterials plays a key role in improving the materials’ properties and performance, especially for applications in chemistry and chemical engineering fields [2]. There is considerable interest in the effects of the shapes and facets of crystalline materials; it is well known that the atomic configuration of the exposed crystal plane plays an important role in these materials’ performance. This is due mainly to the arrangement of the surface atoms and the number of dangling bonds on different crystal planes [3–5].

Anisotropy is a basic property of single crystals, which show different physical and chemical properties on various facets in directions. Usually, these properties can be correlated with the surface energy associated with each facet and can be finely tuned by tailoring the facets to have a specific surface atomic arrangement and coordination, i.e. by tailoring the fraction of surface atoms with unsaturated coordination shells and the number of under- coordinated surface atoms. Measuring the geometries and energies of these surface facets is extremely challenging [6]. Surface energy considerations are crucial in understanding and predicting the morphologies of noble metal nanocrystals. Surface energy is defined as the excess free energy per unit area for a particular crystallographic face. It largely determines the faceting and crystal growth observed with particles at both the nanoscale and mesoscale. Therefore, optimizing the surface-driven attributes of these materials requires a detailed understanding of the structure and chemical composition of their surfaces. With this understanding, one can tailor the surface atomic structure and control which facets of a given material are exposed. Consequently, substantial effort has been devoted to understanding and predicting the structure and stability of complex materials, utilizing state-of-the-art experimental techniques and advanced theoretical approaches [7,8].

Using experimentation to identify the atomistic details involved in a typical crystal growth process is not easy. Computational simulations via density functional theory (DFT) are real alternatives that can provide fresh insight at the atomic scale and thereby specify the important individual atomistic processes taking place during crystal growth. These processes control the final morphology, surface structure, and stability of the end-product materials [9–29]. In addition, there are good reviews on theoretical methods for surface chemistry [30] and the modeling of nanoparticles [31].

By means of experimental and theoretical calculation methods, Li et al. [24] investigated the mechanisms of morphology of tetragonal lanthanum orthovanadate (*t*-$LaVO_4$) nanocrystals controlled by surface chemistry. Some *t*-$LaVO_4$ nanocrystals with different morphologies were prepared via the hydrothermal method by tuning the pH of the growth solution. The authors perform first- principles calculations to examine the relaxed surface structures and to calculate the surface energies and surface tensions of all surfaces under different passivated conditions. Their results showed that the aspect ratio and the exposed facets of the nanocrystals changed as the acidity of the surface conditions changed. This was in good agreement with their experimental findings.

In this communication, we describe the development of a model based on the Wulff construction [32], which can be used to explicitly predict the evolution of morphologies in different environments, as recently developed by our research group [28,29,33]. This model includes a detailed configurational analysis of the different facets and allows us to explain and rationalize the experimental

results of Li et al. [24]. By carrying out atomistic simulations elucidating the diverse atomic-scale structures of a set of low-index surfaces (110), (100), (111), (001) and (101) of *t*-$LaVO_4$, we show that it is possible to achieve the same final results without doing many quantum calculations with high computational demand. A correlation was found between the broken bonding density (D_b) and the surface energy. The relaxed structures and surface energies were used to obtain a complete array of accessible morphologies. This method provides an approach with both predictive and explanatory capabilities. The calculated diagrams relate the crystal growth conditions with the observed morphologies in an attempt to rationalize the morphologies obtained under different experimental conditions.

Theoretical Method and Computational Procedure

Calculations related to *t*-$LaVO_4$ were performed using DFT and implemented in the Vienna *ab initio* simulation package (VASP) in order to find an ideal structure in vacuum [34,35]. The Kohn-Sham equations were solved by means of the Perdew–Burke–Ernzerhof (PBE) exchange-correlation functional [36] and the electron-ion interaction was described by the projector- augmented-wave method [34,37]. The plane-wave expansion was truncated at a cut-off energy of 520 eV. For bulk and surfaces calculations, a (4 × 4 × 4) and (4 × 4 × 1) Monkhorst-Pack special k- points grid was used, respectively. The positions of all atoms, both in the bulk and on the surfaces, were allowed to relax. The conjugated gradient energy minimization method was used to obtain relaxed systems; this was accomplished by requiring the forces experienced by each atom to be smaller than 0.01 eV $Å^{-1}$. Surface calculations were done by considering slabs with thicknesses of up to ~20 Å. This was done to obtain careful descriptions of the surfaces and to reach convergence on the corresponding energy surface values. A vacuum spacing of 15 Å was introduced in the z-direction so that the surfaces would not interact with each other. Surface models containing 6, 4, 4, 6 and 9 molecular units for the (001), (101), (110), (100) and (111) surfaces, respectively, were used in the calculations. These represent all low index surfaces and were modeled using stoichiometric systems. It is worth noting that the (110), and (100) surfaces are O_2-terminated, and the (111) surface is O-terminated, while (001) is LaV and O_2-terminated, and the (101) surface is La-terminated. Fig. 1 depicts the surface representation of the *t*-$LaVO_4$ used in the calculations.

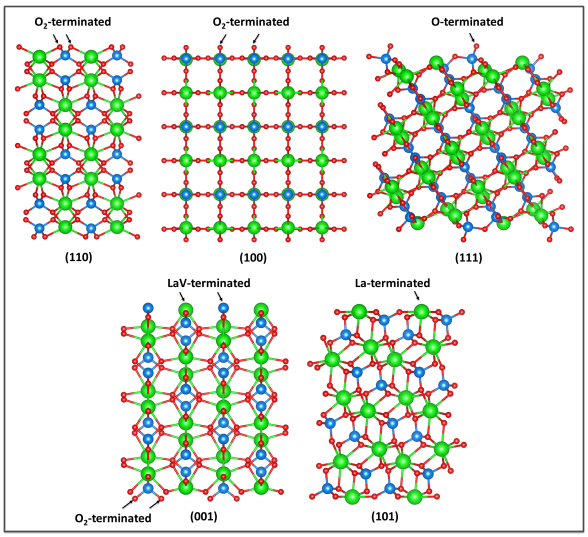

FIGURE 1 – Surface models of (110), (100), (111), (001) and (101) for *t*-$LaVO_4$. The green, blue and red represent La, V and O atoms, respectively.

The conventional approach to the quantitative study of surface morphological properties is based on the classical work of Georg Wulff in the beginning of the 20th century [32]. The Wulff construction has been successfully used in materials science to obtain the shapes of materials, including nanomaterials [38–40]. The surface energy (E_{surf}) is defined as the total energy per repeating cell of the slab (E_{slab}) minus the total energy of the perfect crystal per molecular unit (E_{bulk}) multiplied by the number of molecular units of the surface (n), divided by the surface area per repeating cell of the two sides of the slab, as follows:

$$E_{Surf} = \frac{E_{slab} - nE_{bulk}}{2A}$$

The broken bonding density (D_b) index proposed by Gao et al. [41] was used. By means of D_b values it is possible to verify the surface stability and analyze the number of broken bonds per area of the surface. In the D_b equation, N_b is the number of broken bonds per unit cell area on a particular surface and A is the surface area of the unit cell.

$$D_b = \frac{N_b}{A}$$

Results and Discussion

Table 1 lists the values of the surface energies as well as the broken bonding density (D_b) of the faces used in the Wulff construction. According to the DFT calculations, the order of stability of the surfaces is (100)>(110)>(101)>(111)>(001).

TABLE 1 – Values of E_{surf}, number of broken bonds, area, and broken bonding density (D_b) calculated for *t*-$LaVO_4$.

Surface	E_{surf} (J m^{-2})	Broken bonds	Area (nm^2)	D_b (nm^{-2})
(100)	0.39	8	0.50	16.0
(110)	0.59	8	0.35	22.9
(101)	0.76	12	0.38	31.6
(111)	1.04	28	0.91	30.8
(001)	2.87	20	0.57	35.1

The D_b method has shown certain value due to its simplicity and accuracy in basic systems [29,41]. These results can be directly related to the order and disorder of surface stability; higher D_b values represent the presence of a larger quantity of defects on the surface (broken bonds), indicating an unstable surface. For *t*-$LaVO_4$, the D_b results indicate the following order (100)>(110) >(111)>(101)>(001). Therefore, these results are the inverse of those found for the (101) and (111) surfaces energy. This can be attributed to the complexity of this structure which involves different kinds of bonds with different energies and this method just take into account the number of broken bonds, independent of the type. In this way, a higher number of broken bonds increase the quantitative accuracy of the method in this structure.

Nevertheless, the method showed a fast way to start the surfaces studies.

It is known that morphologies can undergo changes because of differences in the environments in which they are synthesized. These differences may include the presence of surfactants and impurities, and differences in solvents, temperature, and synthetic routes. From the E_{surf} values and the Wulff construction, it is possible to obtain the morphologies of *t*-$LaVO_4$ in *vacuum*.

By assuming the ideal morphology in vacuum as a starting point (see the center of Fig. 2), it was possible to create all of the morphological routing changes caused by surface energy variation that take into account the (110), (100), (111), (001) and (101) surfaces. This simple strategy is based on the modulation of the relationship between the surface stabilities of the different faces and the areas of those parts which are exposed in the final shape. The map of available morphologies of *t*-$LaVO_4$ is displayed in Fig. 2. Fine-tuning of the desired morphologies can be achieved by con- trolling the values of the E_{surf} of the different surfaces. This can be a powerful tool to evaluate the morphologies of materials because of the difficulty in simulating all the details in a reaction system that interacts with each surface [28,29,33].

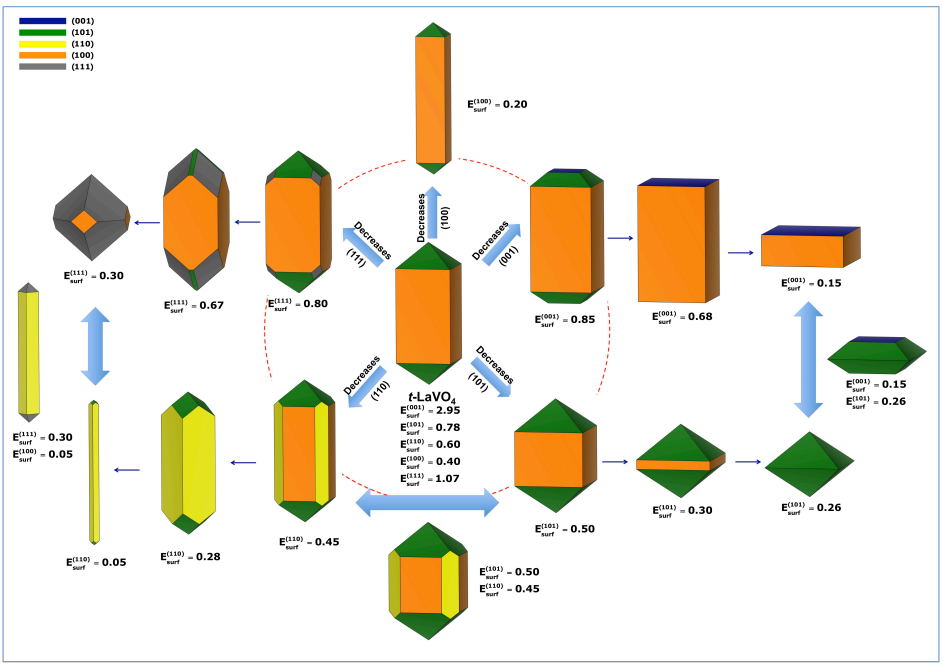

FIGURE 2 – Ideal morphology (in the center) and map of a few morphologies of *t*-$LaVO_4$. Surface energy is in Jm^{-2}.

Fig. 3 depicts a group of morphologies obtained by decreasing the surface energy in small amounts of the (001), (111), (110), (101) and (100).

As was mentioned earlier, the effect of solution acidity on the morphology of as-synthetized *t*-$LaVO_4$ nanocrystals was reported by Li et al. [24]. In their study, the authors prepared nanocrystals using a hydrothermal method in conditions of several different

levels of acidity: most-acidic, highly-acidic, moderately acidic and weakly acidic. To compare the resulting morphologies, they simulated these conditions using a 2 × 1 supercell for all surface passivation. Li et al. [24] demonstrated that the (001) surface is the most affected by the pH shift; its E_{surf} decreased as the fraction of hydrogen in the adsorbates decreased, while the E_{surf} of the (100) and (101) surfaces first increased and then decreased. The difference of the values for the surface energies of (100), (101) and (001) calculated and those obtained by Li et al. [24] may be due to the different functional used in the calculation. Nevertheless the order of stability is the same.

However, here we show that it is possible to achieve the same final results, with the exception of the advantage to predict, with- out doing many quantum calculations with high computational demand (such as supercell and adsorption of atoms or molecules). Starting with the ideal morphology we decreased the (001) surface energy, as shown in Fig. 3a, and found it possible to observe not only morphologies similar to those synthetized by Li el at. [24], but also more possibilities. To adjust the elongation of the particle, it is necessary to change the (1 0 1) energy surface, which is respon- sible for this part of the structure. When the (101) surface energy decreases, the exposed area of the surface increases and the rela- tive area of (100) decreases causing the structure to become com- pressed, or less elongated (see Fig. 3d). Therefore, the morphologies of *t*-$LaVO_4$ are controlled by (001), (101) and (100) surface energies.

Material mapping can be used as a guide for experimental researchers in order to evaluate where synthetic modifications interact in a more pronounced way. Some published papers regarding *t*-$LaVO_4$ report various experimental morphologies [42–46].

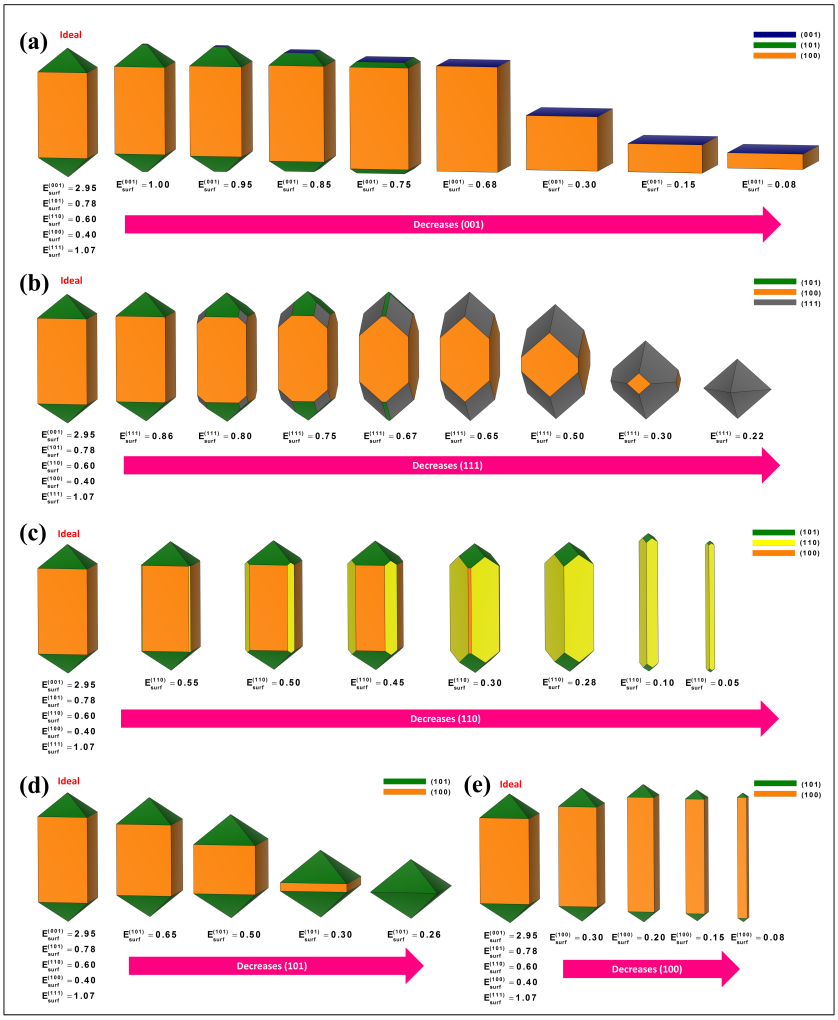

FIGURE 3 – Morphologies of *t*-$LaVO_4$ when the values of E_{surf} decrease for (a) the (001) surface; (b) the (111) surface; (c) the (110) surface; (d) the (101) surface and (e) the (100) surface. Surface energy is in Jm^{-2}.

In these papers, it is possible to find similarities between particles of the same phase when compared to the morphology map. For an accurate comparison, it is necessary to perform a more systematic study of the

morphology. This is because the size of the particles makes precise determinations regarding the exposed planes difficult from an experimental perspective. It is worth noting that the simulation does not take into account the formation of particles via any secondary process such as aggregation and coalescence of primarily particles.

Conclusions

The study of a material's morphological changes based on theoretical calculation can be used to gain a better understanding of the control of its growth and to provide a more reasonable explanation about its mechanisms of transformation. In this communication, tetragonal phase $LaVO_4$ is investigated by performing theoretical calculations on the mechanism of the morphology transformation. The present strategy provides a perspective for further studying the surface structure and other physical and chemical related applications. The calculated morphology maps must be used as guide for experimentalists to analyze and discuss the results that they obtain by means of Field Emission Gun-Scanning Electron Microscopy (FEG-SEM) and/or Transmission Electron Microscopy (TEM). This methodology clearly show the exposed faces and are capable of explaining the formation of complex morphologies, such as pipes, and hollow spheres. We used this guide with experimental morphologies of different binary oxides such as: Co_3O_4, α-Fe_2O_3, and In_2O_3, as well as metals and metal oxides such as: Ag, anatase TiO_2, $BaZrO_3$, and α-Ag_2WO_4, and $BaWO_4$. However, one must recognize that the results presented here are for ideal systems in vacuum. There are important factors involved in a synthesis process that affect the final shape of the end product, including the precursor, solvent, reducing agent, ligand agent, and capping agent. In addition, the presence of defects and impurities may change growth paths and energetics. Both factors can change the morphology of the final product. Further calculations which include these effects will help to improve our understanding of the atomic nature of the observed growth modes and put our understanding of the final morphology on a firmer footing.

Acknowledgments

This work was financially supported by the following Spanish and Brazilian research funding institutions: PrometeoII/2014/022 and ACOMP/2014/270 projects (Generalitat-Valenciana), Ministe- rio de Economia y Competitividad (CTQ2012-36253-C03-02), FAPESP (2013/07296-2 and 2013/26671-9), CNPq (479644/2012- 8, 350711/2012-7, 304531/2013-8 and 151136/2013-0). CAPES and Programa de Cooperación Científica con Iberoamerica (Brasil) of Ministerio de Educación (PHBP14-00020). J.A. acknowledges to Ministerio de Economia y Competitividad, 'Salvador Madariaga' program, PRX15/00261. M.M.F. acknowledges CAPES for PNPD scholarship.

References

[1] A.R. Tao, S. Habas, P. Yang, Shape control of colloidal metal nanocrystals, Small 4 (2008) 310-325.

[2] C. Burda, X. Chen, R. Narayanan, M.A. El-Sayed, Chemistry and Properties of Nanocrystals of Different Shapes, Chem. Rev. 105 (2005) 1025-1102.

[3] J. Wang, C. Xu, G. Lv, Formation processes of CuCl and regenerated Cu crystals on bronze surfaces in neutral and acidic media, Appl. Surf. Sci. 252 (2006) 6294-6303.

[4] F. Zaera, New Challenges in Heterogeneous Catalysis for the 21st Century, Catal. Lett. 142 (2012) 501-516.

[5] Y. Xia, X. Xia, H.-C. Peng, Shape-Controlled Synthesis of Colloidal Metal Nanocrystals: Thermodynamic versus Kinetic Products, J. Amer. Chem. Soc. 137 (2015) 7947-7966.

[6] S.J.L. Billinge, I. Levin, The problem with determining atomic structure at the nanoscale, Science 316 (2007) 561-565.

[7] J. Goniakowski, F. Finocchi, C. Noguera, Polarity of oxide surfaces and nanostructures, Rep. Prog. Phys. 71 (2008) 016501.

[8] C. Noguera, J. Goniakowski, Polarity in Oxide Nano-objects, Chem. Rev. 113 (2013) 4073-4105.

[9] D.A. Tompsett, S.C. Parker, P.G. Bruce, M.S. Islam, Nanostructuring of β-MnO2: The Important Role of Surface to Bulk Ion Migration, Chem. Mater. 25 (2013) 536-541.

[10] A. Karim, S. Fosse, K.A. Persson, Surface structure and equilibrium particle shape of the LiMn2O4 spinel from first-principles calculations, Phys. Rev. B 87 (2013) 075322.

[11] N. Li, H. Dong, H. Dong, J. Li, W. Li, G. Niu, X. Guo, Z. Wu, L. Wang, Multifunctional perovskite capping layers in hybrid solar cells, J. Mater. Chem. A 2 (2014) 14973-14978.

[12] A.S. Barnard, Direct Comparison of Kinetic and Thermodynamic Influences on Gold Nanomorphology, Acc. Chem. Res. 45 (2012) 1688-1697.

[13] A. Seyed-Razavi, I.K. Snook, A.S. Barnard, Origin of nanomorphology: does a complete theory of nanoparticle evolution exist?, J. Mater. Chem. 20 (2010) 416-421.

[14] F. Zasada, W. Piskorz, P. Stelmachowski, A. Kotarba, J.-F.o. Paul, T. Płociński, K.J. Kurzydłowski, Z. Sojka, Periodic DFT and HR-STEM Studies of Surface Structure and Morphology of Cobalt Spinel Nanocrystals. Retrieving 3D Shapes from 2D Images, J. Phys. Chem. C 115 (2011) 6423-6432.

[15] D.G. Stroppa, L.A. Montoro, A. Beltrán, T.G. Conti, R.O. da Silva, J. Andrés, E.R. Leite, A.J. Ramirez, Dopant Segregation Analysis on Sb:SnO2 Nanocrystals, Chem. – Eur. J. 17 (2011) 11515-11519.

[16] A. Beltrán, J. Andrés, E. Longo, E.R. Leite, Thermodynamic argument about SnO2 nanoribbon growth, Appl. Phys. Lett. 83 (2003) 635-637.

[17] E.R. Leite, T.R. Giraldi, F.M. Pontes, E. Longo, A. Beltrán, J. Andrés, Crystal growth in colloidal tin oxide nanocrystals induced by coalescence at room temperature, Appl. Phys. Lett. 83 (2003) 1566-1568.

[18] D.G. Stroppa, L.A. Montoro, A. Campello, L. Gracia, A. Beltran, J. Andres, E.R. Leite, A.J. Ramirez, Prediction of dopant atom distribution on nanocrystals using thermodynamic arguments, Phys. Chem. Chem. Phys. 16 (2014) 1089-1094.

[19] M.R.D. Bomio, R.L. Tranquilin, F.V. Motta, C.A. Paskocimas, R.M. Nascimento, L. Gracia, J. Andres, E. Longo, Toward Understanding the Photocatalytic Activity of PbMoO4 Powders with Predominant (111), (100), (011), and (110) Facets. A Combined Experimental and Theoretical Study, J. Phys. Chem. C 117 (2013) 21382-21395.

[20] V.M. Longo, L. Gracia, D.G. Stroppa, L.S. Cavalcante, M. Orlandi, A.J. Ramirez, E.R. Leite, J. Andrés, A. Beltrán, J.A. Varela, E. Longo, A joint experimental and theoretical study on the nanomorphology of CaWO 4 crystals, J. Phys. Chem. C 115 (2011) 20113-20119.

[21] K. Qi, D. Li, J. Fu, L. Zhu, X. Duan, Q. Qin, G. Wang, W. Zheng, Elucidating Ionic Liquid Environments That Affect the Morphology of TiO2 Nanocrystals: A DFT+D Study, J. Phys. Chem. C 118 (2014) 23320-23327.

[22] W. Piskorz, J. Gryboś, F. Zasada, P. Zapała, S. Cristol, J.-F. Paul, Z. Sojka, Periodic DFT Study of the Tetragonal

ZrO2 Nanocrystals: Equilibrium Morphology Modeling and Atomistic Surface Hydration Thermodynamics, J. Phys. Chem. C 116 (2012) 19307-19320.

[23] A. Whiteside, C.A.J. Fisher, S.C. Parker, M. Saiful Islam, Particle shapes and surface structures of olivine NaFePO4 in comparison to LiFePO4, Phys. Chem. Chem. Phys. 16 (2014) 21788-21794.

[24] P. Li, X. Zhao, C.-J. Jia, H. Sun, Y. Li, L. Sun, X. Cheng, L. Liu, W. Fan, Mechanism of Morphology Transformation of Tetragonal Phase LaVO4 Nanocrystals Controlled by Surface Chemistry: Experimental and Theoretical Insights, Cryst. Growth Des. 12 (2012) 5042-5050.

[25] E. Kanaki, S. Gohr, C. Mueller, B. Paulus, Theoretical study on the morphology of MgF2 nanocrystals at finite temperature and pressure, Surf. Sci. 632 (2015) 158-163.

[26] Y. Li, J. Zhang, F. Yang, J. Liang, H. Sun, S. Tang, R. Wang, Morphology and surface properties of LiVOPO4: a first principles study, Phys. Chem. Chem. Phys. 16 (2014) 24604-24609.

[27] V.L. Deringer, R. Dronskowski, From Atomistic Surface Chemistry to Nanocrystals of Functional Chalcogenides, Angew. Chem. Int. Ed. 54 (2015) 15334-15340.

[28] J. Andrés, L. Gracia, A.F. Gouveia, M.M. Ferrer, E. Longo, Effects of surface stability on the morphological transformation of metals and metal oxides as investigated by first-principles calculations, Nanotechnology 26 (2015) 405703-405713.

[29] M.M. Ferrer, A.F. Gouveia, L. Gracia, E. Longo, J. Andres, A 3D platform for the morphology modulation of materials: First principles calculations on the thermodynamic stability and surface structure of metal oxides: Co3O4, α-Fe2O3, and In2O3, Modell. Simul. Mater. Sci. Eng. 24 (2016) 025007-025016.

[30] A. Groß, Theoretical Surface Science: A Microscopic Perspective, Springer, Berlin, 2009.

[31] A.S. Barnard, Modelling of nanoparticles: approaches to morphology and evolution, Rep. Prog. Phys. 73 (2010) 086502.

[32] G. Wulff, On the question of speed of growth and dissolution of crystal surfaces, Z. Kristallogr. 34 (1901) 449-530.

[33] M.C. Oliveira, L. Gracia, I.C. Nogueira, M.F.d. Carmo Gurgel, J.M.R. Mercury, E. Longo, J. Andrés, Synthesis and morphological transformation of BaWO4 crystals: Experimental and theoretical insights, Ceram. Int. 42 (2016) 10913-10921.

[34] G. Kresse, J. Furthmuller, Efficiency of ab-initio total energy calculations for metals and semiconductors using a plane-wave basis set, Comput. Mater. Sci. 6 (1996) 15-50.

[35] G. Kresse, J. Hafner, Ab-initio Molecular-Dynamics Simulation of the Liquid-Metal Amorphous-Semiconductor Transition in Germanium, Phys. Rev. B: Condens. Matter Mater. Phys. 49 (1994) 14251-14269.

[36] J.P. Perdew, K. Burke, M. Ernzerhof, Generalized gradient approximation made simple, Phys. Rev. Lett. 77 (1996) 3865-3868.

[37] G. Kresse, D. Joubert, From ultrasoft pseudopotentials to the projector augmented-wave method, Phys. Rev. B: Condens. Matter Mater. Phys. 59 (1999) 1758-1775.

[38] A. Gurlo, Nanosensors: towards morphological control of gas sensing activity. SnO2, In2O3, ZnO and WO3 case studies, Nanoscale 3 (2011) 154-165.

[39] G.D. Barmparis, Z. Lodziana, N. Lopez, I.N. Remediakis, Nanoparticle shapes by using Wulff constructions and first-principles calculations, Beilstein J. Nanotechnol. 6 (2015) 361-368.

[40] A. Hellman, K. Honkala, I.N. Remediakis, A. Logadottir, A. Carlsson, S. Dahl, C.H. Christensen, J.K. Norskov, Ammonia synthesis and decomposition on a Ru-based catalyst modeled by first-principles, Surf. Sci. 603 (2009) 1731-1739.

[41] Z.-Y. Gao, W. Sun, Y.-H. Hu, Mineral cleavage nature and surface energy: Anisotropic surface broken bonds consideration, T. Nonferr. Metal. Soc. 24 (2014) 2930-2937.

[42] J. Ma, Q. Wu, Y. Ding, Selective synthesis of monoclinic and tetragonal phase LaVO(4) nanorods via oxides-hydrothermal route, J. Nanopart. Res. 10 (2008) 775-786.

[43] J. Zhang, J. Shi, J. Tan, X. Wang, M. Gong, Morphology-controllable synthesis of tetragonal LaVO4 nanostructures, Crystengcomm 12 (2010) 1079-1085.

[44] Z. Xu, C. Li, Z. Hou, C. Peng, J. Lin, Morphological control and luminescence properties of lanthanide orthovanadate LnVO(4) (Ln = La to Lu) nano-/microcrystals via hydrothermal process, Crystengcomm 13 (2011) 474-482.

[45] L.-P. Wang, L.-M. Chen, Controllable synthesis and luminescent properties of LaVO4:Eu nanocrystals, Mater. Charact. 69 (2012) 108-114.

[46] B. Xie, G. Lu, Y. Wang, Y. Guo, Y. Guo, Selective synthesis of tetragonal LaVO4 with different vanadium sources and its luminescence performance, J. Alloys Compd. 544 (2012) 173-180.

2.4 – Surfactant-mediated morphology and photocatalytic activity of α-Ag_2WO_4 material

THE JOURNAL OF PHYSICAL CHEMISTRY C

Article

Cite This: J. Phys. Chem. C 2018, 122, 8667−8679

pubs.acs.org/JPCC

Surfactant-Mediated Morphology and Photocatalytic Activity of α-Ag_2WO_4 Material

Published as part of The Journal of Physical Chemistry virtual special issue "Manuel Yáñez and Otilia Mó Festschrift".

Nadia G. Macedo,[†] Amanda F. Gouveia,[†] Roman A. Roca,[†] Marcelo Assis,[†] Lourdes Gracia,[‡] Juan Andrés,[*,§] Edson R. Leite,[⊥] and Elson Longo[†]

[†]CDMF, LIEC, Federal University of São Carlos, P.O. Box 676, 13565-905 São Carlos, SP, Brazil

[‡]Department of Physical Chemistry, University of Valencia, Burjassot 46100, Spain

[§]Department of Analytical and Physical Chemistry, University Jaume I, Castelló 12071, Spain

[⊥]Brazilian Nanotechnology National Laboratory (LNNano), Brazilian Center for Research in Energy and Materials (CNPEM), 13083-970 Campinas, SP, Brazil

Supporting Information

ABSTRACT: In the present work, the morphology (hexagonal rod-like vs cuboid-like) of an α-Ag_2WO_4 solid-state material is manipulated by a simple controlled-precipitation method, with and without the presence of the anionic surfactant sodium dodecyl sulfate (SDS), respectively, over short reaction times. Characterization techniques, such as X-ray diffraction analysis, Rietveld refinement analysis, Fourier-transform (FT) infrared spectroscopy, FT Raman spectroscopy, UV−vis spectroscopy, transmission electron microscopy (TEM), high-resolution TEM, selected area electron diffraction, energy-dispersive X-ray spectroscopy, field emission-scanning electron microscopy (FE-SEM), and photoluminescence emission, are employed to disclose the structural and electronic properties of the α-Ag_2WO_4 material. First-principles calculations were performed to (i) obtain the relative stability of the six low-index surfaces of α-Ag_2WO_4; (ii) rationalize the crystal morphologies observed in FE-SEM images (using the Wulff construction); and (iii) determine the energy profiles associated with the transformation process between both morphologies induced by the presence of SDS. Finally, we demonstrate a relationship between morphology and photocatalytic activity, evaluated by photodegradation of Rhodamine B dye under UV light, based on the different numbers of unsaturated superficial Ag and W cations (local coordination, i.e., clusters) of each surface.

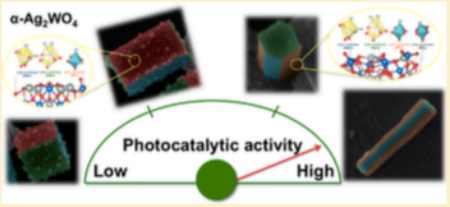

Surfactant-Mediated Morphology and Photocatalytic Activity of α-Ag_2WO_4 Material

Nadia G. Macedo[1], Amanda F. Gouveia[1], Roman A. Roca[1], Marcelo Assis[1], Lourdes Gracia[2], Juan Andrés*[3], Edson R. Leite[1] and Elson Longo[1]

[1]CDMF, LIEC, Federal University of São Carlos (UFSCar), P.O. Box 676, 13565-905 São Carlos, SP, Brazil
[2]Department of Physical Chemistry, University of Valencia (UV), Burjassot 46100, Spain
[3]Department of Analytical and Physical Chemistry, University Jaume I (UJI), Castelló 12071, Spain

In the present work, the morphology (hexagonal rod-like vs cuboid-like) of an α-Ag_2WO_4 solid-state material is manipulated by a simple controlled-precipitation method, with and without the presence of the anionic surfactant sodium dodecyl sulfate (SDS), respectively, over short reaction times. Characterization techniques, such as X-ray diffraction analysis, Rietveld refinement analysis, Fourier-transform (FT) infrared spectroscopy, FT Raman spectroscopy, UV−vis spectroscopy, transmission electron microscopy (TEM), high-resolution TEM, selected area electron diffraction, energy-dispersive X-ray spectroscopy, field emission-scanning electron microscopy (FE-SEM), and photoluminescence emission, are employed to disclose the structural and electronic properties of the α-Ag_2WO_4 material. First-principles calculations were performed to (i) obtain the relative stability of the six low-index surfaces α-Ag_2WO_4; (ii) rationalize the crystal morphologies observed in FE-SEM images (using the Wulff construction); and (iii) determine the energy profiles associated with the transformation process between both morphologies induced by the presence of SDS. Finally, we demonstrate a relationship between morphology and photocatalytic activity, evaluated by photodegradation of Rhodamine B dye under UV light, based on the different numbers of unsaturated superficial Ag and W cations (local coordination, i.e., clusters) of each surface.

This work aims to be a tribute to the Prof. Otilia Mó and Manuel Yañéz, in recognition of their excellent careers both personal and professional in the field of theoretical and computational chemistry.

Introduction

Organic chemicals are still largely employed by the textile industries and play a critical role in the pollution of river water, causing chemical and biological changes in aquatic systems, which can kill animals and plants.[1] This problem makes the improvement and elucidation of processes like the gas sensing[2] capabilities and photocatalytic degradation of these dyes a priority.[3] Ag_2WO_4 appears to be a good alternative to the extensively researched materials currently used as photocatalysts (e.g. TiO_{24}, ZnO5, WO_3[6]) and should thus be further studied and understood. Recent research reported the photocatalytic activity of α-[7] and β-[8] Ag_2WO_4 under UV light.[9] Orthorhombic α-Ag_2WO_4,[10] which also presents good luminescent,[11] antimicrobial,[12] and gas-sensing[13] properties, offers new opportunities to further optimize the facet- dependent photocatalytic performance of semiconductors. The structure of α-Ag_2WO_4 was resolved by our research group.[14] It is composed of octahedral [WO_6] and [AgO_n] clusters (n = 7, deltahedral [AgO_7]; n = 6, octahedral [AgO_6]; n = 4, tetrahedral [AgO_4] and n = 2, angular [AgO_2]), as depicted in Figure 1. Because of the particular orthorhombic geometry, structural and electronic distortions and the corresponding variations in Ag−O and W−O bond lengths and O−W−O and O−Ag−O bond angles may be sensed.[15] The properties of this semiconductor change according to the crystallographic phase, size, and morphology, and these variables are all dependent on the synthesis procedure. Each surface of a crystal can possess a particular surface energy, atomic distribution, local coordination (clusters) of exposed metals, vacancies, etc. These results tend to confirm the hypothesis that the properties observed for this material result from a compromise between the presence of local defects (short-range disorder) and crystal lattice ordering (long-range order). Therefore, finding a synthesis method to control these characteristics is crucial to determine the properties and subsequent technological applications of this material.

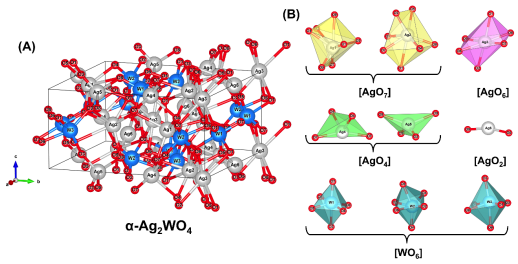

FIGURE 1 – (A) The crystal structure of orthorhombic α-Ag_2WO_4 with the space group *Pn2n* and (B) the different clusters of Ag and W atoms that compose the structure.

α-Ag_2WO_4 materials, at nano- and microscale, can be obtained by traditional synthesis methods,[16] or, more recently, by conventional hydrothermal (CH)[17] and microwave hydrothermal (MH)[18] methods. However, there are limitations related to these methods, such as the difficulties of large-scale reproduction, the necessity of specific equipment, the small quantities of product obtained, and safety concerns. Therefore, achieving precise control over the

synthesis, morphology, and properties of α-Ag_2WO_4 has become a hot research subject. In this context, controlled-precipitation (CP)[19] is a simple and facile method that is widely employed in the production of α-Ag_2WO_4, which has good bactericide properties and photo- catalytic activity. By varying some synthetic parameters of the CP method, such as temperature, stirring time, solvents, or use of capping agents,[20] one can obtain significant changes in the morphology and size of the final samples and, consequently, in some highly surface-dependent properties like photocatalytic activity.[7]

The properties of nanoscale materials and the changes in these properties along with size or shape is a hot research field.[21] Unraveling the relationship between the atomic structure and the functional properties can be a crucial step, especially in complex materials, where short-range interactions, rather than the average structure, can define the actual properties and behavior of the material. One of the main factors determining functionality is the crystal morphology, because the number of active sites is clearly surface-dependent. The variation of reaction conditions can produce different morphologies and, consequently, modify their properties dramatically. However, the control of a crystal morphology is a complex process depending on several factors. Surfactants are particularly important due to their influence on the (nano) particle structure and other physical and chemical properties, having the remarkable ability to control crystal growth and direct it in a morphology- and size-controlled manner.[22] Achieving a detailed understanding of mechanisms by which surfactants can control the morphology of as-synthesized material is of paramount importance, given the effects on the photocatalytic activity of the material.

In this study, we seek to fulfill a threefold objective. The first is to report the novel formation of α-Ag_2WO_4 by a simple CP method, with short reaction time, with and without the presence of an anionic surfactant (sodium dodecyl sulfate, SDS), to evaluate the influence of this surfactant on crystal formation and the resultant structure and morphology. Second, the photocatalytic degradation of Rhodamine B (RhB) will be investigated as a function of the obtained morphology. The third aim is to determine the relationship between morphology and photocatalytic activity.

This paper is organized as follows: Section 2 presents the experimental procedures and computational methods; Section 3 contains the results and discussion; and, finally, Section 4 provides a summary of conclusions.

Methods

Synthesis. The α-Ag_2WO_4 crystals were prepared by a simple CP method at 90 °C in the presence of the anionic SDS ($C_{12}H_{25}SO_4Na$; 90% purity, Synth) as follows: 1×10^{-3} mol of dihydrate sodium tungstate ($Na_2WO_4 \cdot 2H_2O$; 99% purity, Sigma-Aldrich;) and 2×10^{-3} mol of silver nitrate ($AgNO_3$; 98.80% purity, Cennabras) were dissolved separately in 50 mL of deionized water each. SDS (1 g) was added to the sodium tungstate solution, and the solutions were heated under continuous stirring. After the two solutions reached 90 °C, the silver nitrate solution was poured into the sodium tungstate solution and allowed to stir for 5 min. The precipitate was then decanted and washed several times with distilled water. Washing of the precipitate was necessary to eliminate the Na^+, NO^{3-}, or SO_4^{2-} ions and residual organic compounds. Finally, the precipitate was dried with acetone at room temperature and collected after an overnight period. The reaction was also performed under the same conditions but without the presence of SDS. The precipitates obtained from the reaction without and with SDS are light beige and light brown, respectively.

Characterization. The α-Ag_2WO_4 crystals were structurally characterized by X-ray diffraction (XRD) using a D/Max-2500PC diffractometer (Rigaku, Japan) with Cu Kα radiation (λ = 1.5406 Å) in the 2θ range from 5° to 75°, with a scanning velocity of 2° min^{-1}, in the normal routine, and from 10° to 110° with a scanning velocity of 1°/min in the Rietveld routine. The shapes and sizes of the products obtained were observed with a field-emission scanning electron microscope (FE-SEM), operated at 5−10 kV (Supra 35-VP, Carl Zeiss, Germany). Transmission electron microscopy (TEM) analysis was performed to verify additional morphology details inside a Jeol JEM 2100F with a field emission gun (FEG) operating at 200 kV. Some crystallographic aspects of the samples were also verified with selected area electron diffraction (SAED) analysis and high-resolution transmission electron microscopy (HR- TEM) in the same equipment. Additionally, energy dispersive X-ray spectroscopy (EDS) was also employed to obtain a local elementary composition with EDAX equipment. To verify the complete elimination of the surfactant, thermogravimetric analysis (TGA) was performed with a NETZSCH TG 209 F1 instrument, within the temperature range from 22 to 900 °C, and with a rate of 10k/min, under an atmosphere of synthetic air. Fourier-transform infrared (FT-IR) spectroscopy was

performed in a Bomem-Michelson spectrophotometer in transmittance mode (model MB102), in the range from 250 to 1000 cm^{-1}, using KBr pellets as a reference. Raman spectra were recorded using the iHR550 spectrometer Horiba Jobin- Yvon coupled to a CCD detector and an argon-ion laser (Melles Griot) operating at 514.5 nm with a maximum power of 200 mW and a fiber microscope. UV−Vis diffuse reflectance measurements were obtained using a Varian Cary spectrometer model 5G on the diffuse reflectance mode, with a wavelength range from 200 to 800 nm, and a scan speed of 600 nm min^{-1}. Photoluminescence (PL) measurements were obtained at room temperature with a monochromator (Thermal Jarrel-Ash Monospect-27) linked to a photomultiplier model R446 (Hamatsu Photonics) and a double monochromator (Jobin- Yvon-U1000) directly linked to a system of photon counting. A Krypton laser (Coherent Innova 90k) with a wavelength of 350 nm was used as the excitation source, with a maximum exit power rate of 500 mW. After the passage of the laser beam through the optical chopper, the power was reduced and maintained at 40 mW on the samples. In addition, the surface areas of the samples were obtained by physiosorption of N_2 at 77 K in a Micromeritics equipment (ASAP 2420). Before the analysis the samples were heated to 120 °C for 10 h under vacuum to eliminate water and physically adsorbed. The surface area was calculated with the Brunauer−Emmet−Teller (BET) equation[23].

Photocatalysis assays. To perform the photocatalysis experiments, 50 mL of RhB (95%, Mallinckrodt) solution (1×10^{-5} mol L^{-1}) with a pH of 4.0 was mixed with 50 mg of α-Ag_2WO_4.The mixture, consisting of the dye and photocatalyst, was irradiated in a dark box using six UV lamps (Phillips TL-D, 15 W). Before UV illumination, the suspensions were sonicated for 10 min in an ultrasonic bath (42 kHz, model 1510) to allow saturated absorption of RhB onto the catalyst. Subsequently, the dispersion containing the catalyst and the dye was transferred to a vessel inside the photoreactor, with the temperature maintained at 20 °C via a thermostatic bath and vigorous stirring. At 0, 5, 10, 20, 30, 50, 70, 90, and 120 min, a 2 mL aliquot of the suspension was removed from the photocatalytic system and placed in a plastic tube, which was centrifuged at 13 000 rpm for 10 min to separate the solid catalyst from the liquid phase. Finally, the kinetics of the dye photodegradation process were monitored in a commercial cuvette via UV−vis spectroscopy (JASCO V-660) at 554 nm. This procedure was subsequently performed for each synthesized α-Ag_2WO_4 sample.

Computational Details. From the calculated surface energy (E_{surf}) values for the six low-index crystals facets reported by Andreś et al.,[24] it is possible to determine the equilibrium shape and ideal morphology, by using the Wulff construction. Furthermore, by changing the relative surface energy values of each facet, we found a map of available morphologies for α-Ag_2WO_4, as well as the pathways linking the ideal and given morphologies, including both hexagonal rod-like and cuboid-like morphologies.[24]

This methodology provides a simple relationship between E_{surf} and the distance of the planes and has been used in materials science to predict experimental crystal shapes.[25]

In this study, we go further by calculating the energy profiles of the paths connecting different morphologies from the values of the polyhedron energy ($E_{\text{polyhedron}}$) by a function of the form

$$E_{polyhedron} = \sum_i C_i \times E^i_{surf} \quad (1)$$

where C_i is the percentage contribution of the surface area to the total surface area of the polyhedron, $C_i = A^i / A^{polyhedron}$, and E^i_{surf} is the surface energy of the corresponding surface. The energy profiles were calculated by decreasing and/or increasing the E_{surf} values of a given surface of the polyhedron.

Results and discussion

X-ray diffraction analysis. Figure 2 shows the XRD patterns of the synthesized α-Ag_2WO_4 crystals. According to the Inorganic Crystal Structure Database, ICSD card 34-61, these crystals have an orthorhombic structure, without any deleterious phases, with the space group *Pn*2*n* and point group symmetry (C_{2v}^{10}).[26] Therefore, the samples synthesized by the CP method with and without anionic surfactant SDS present a pure α-phase structure. Both crystals have sharp and well-defined diffraction peaks, which indicate a good degree of long-range structural order in the lattice, and they are all in good agreement with the respective databases. There are also no significant variations in peak intensity or position between both samples.

Rietveld refinement analysis. The structural refinement using the Rietveld method[27] was performed using GSAS program, version 1. The refinement plots for the α-Ag_2WO_4 crystals synthesized by the CP method at 90 °C without and with the presence of SDS, respectively, were depicted in Figure 3A,B. The Rietveld refinement confirms the orthorhombic structure, with only a small variation between the

values obtained in the refinement and the literature.[14]

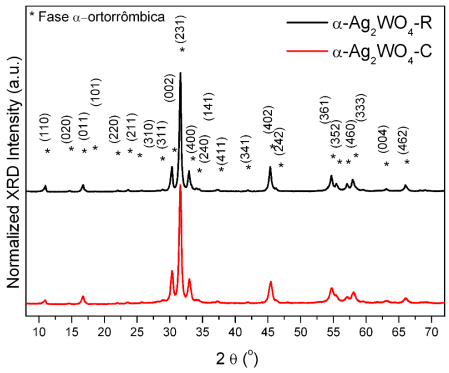

FIGURE 2 – Normalized XRD patterns of the α-Ag_2WO_4 crystals synthesized by the CP method at 90 ºC without (black line color) and with (red line color) the presence of anionic surfactant SDS.

The structural results (a, b, c cell parameters and volume) with the statistical reliability parameters (R_{wp} and GOF) are shown in Table 1. The statistical reliability of the parameters indicates a high agreement between the calculated and observed X-ray patterns for both samples.

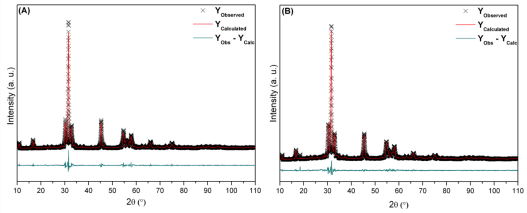

FIGURE 3 – Rietveld refinement plots of α-Ag_2WO_4 crystals synthesized by the CP method at 90 ºC without (A) and with (B) the presence of anionic surfactant SDS.

Morphological analysis. FE-SEM analysis is a very powerful tool to provide morphological information, such as the arrangement of atoms in the structure and the degree of structural and electronic order/disorder.

TABLE 1 – Rietveld refinement results for α-Ag_2WO_4 crystals synthesized by the CP method at 90 ºC without (A) and with (B) the presence of anionic surfactant SDS.

Sample	a (Å)	b (Å)	c (Å)	Volume	$R_{wp(\%)}$	GOF
A	10.897	12.033	5.904	773.430	9.8	1.91
B	10.851	12.036	5.889	769.636	7.4	1.64
Ref[14]	10.878	12.009	5.895	770.09	12.3	1.88

Figure 4 shows the FE-SEM images of the experimentally obtained products. Figure 4A is an image of α-Ag_2WO_4 crystals obtained from the short period stirring synthesis without surfactant under 90 °C. The observed morphology is hexagonal rod-like, in accordance with previous studies found in literature,[7] and is depicted in Figure 4B. The hexagonal rod-like α-Ag_2WO_4 crystals usually have a length of nearly 2 μm. In this case, probably due to the short time of stirring (5 min), the crystals are smaller (see Figure 5).

Figure 4C displays the morphology of the product obtained when the anionic surfactant SDS is included in the CP method, maintaining the other conditions constant. It is possible to observe several cuboid-like crystals, depicted in Figure 4D. Although there are some reports in the literature of rectangular nanorod crystals of Ag_2WO_4 combined with hexagonal rods,[28] this is the first report in which the predominance of cuboid-like morphology is observed. The samples synthesized without and with anionic surfactant SDS are designated, according to their morphology, as α-Ag_2WO_4-R (α-Ag_2WO_4 hexagonal rod-like crystals) and α-Ag_2WO_4-C (α-Ag_2WO_4 cuboid-like crystals), respectively.

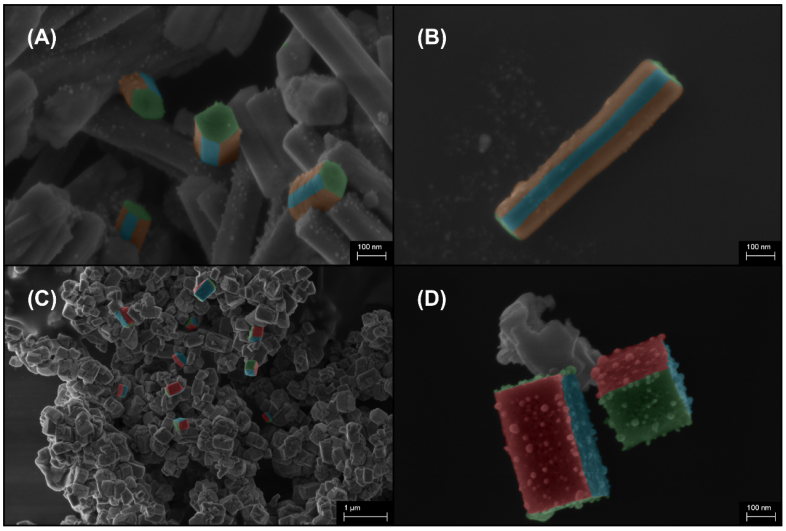

FIGURE 4 – FE-SEM images of α-Ag_2WO_4 obtained by the CP method: (A) and (B) α-Ag_2WO_4-R crystals, and (C) and (D) α-Ag_2WO_4-C crystals.

The FE-SEM image (Figure 4D) also shows two crystals, one possessing a cubic shape, α-Ag_2WO_4-C, and the other being exactly twice the length of the first one. An analysis of the histogram in Figure 5 renders a

length distribution ranging from 100 to 300 nm, in the case of the cuboid crystals, with an average of nearly 200 nm. These results seem to indicate that the basic cubic blocks link to each other by coalescence in such a way that the theoretical cubes become elongated cuboid-like particles.

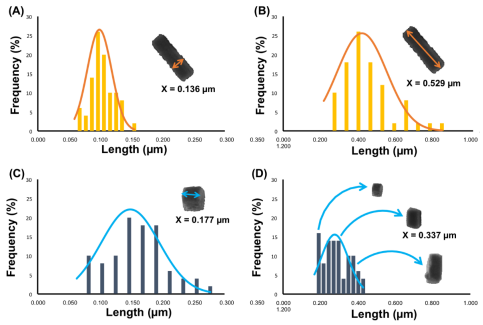

FIGURE 5 – Average height and width distribution of α-Ag_2WO_4-R crystals (A) and (B) and α-Ag_2WO_4-C crystals (C) and (D).

As studied before by our work group,[15,29] the irradiation of α-Ag_2WO_4 by an electron beam generates the formation of metallic Ag nanoparticles on their surface.[30] Figure 6A,B displays the TEM images of the α-Ag_2WO_4-R and α-Ag_2WO_4-C samples, respectively. Figure 6C,D displays the SAED analysis by HR-TEM. The patterns are diffuse halo rings typical from amorphous materials. The presence of these diffuse rings indicates the changes in interatomic spacing induced by the deformation process.[29] The formation of Ag nanoparticles at some regions on the surface α-Ag_2WO_4 are confirmed by HR- TEM analysis as it is shown in Figure 6E,G, as the interplanar distances between (111) planes, 2.35 Å, of the Ag cubic structure, according to ICSD No. 064706. The local elementary analysis EDS shown in Figure 6F,H also confirms the presence of metallic Ag, Cu, and C shown in the elementary analysis EDS.

FT-IR and FT-Raman spectroscopies. Analysis of the FT-IR and FT-Raman data provides information about the local coordination of Ag and W cations that form the crystalline structure. Figure 7A presents the FT-IR spectra for both materials. The intense bands localized at 829 and 860 cm^{-1} for both samples are due to the asymmetric vibrations of the O−W−O moiety in [WO_6] distorted clusters. The bands identified at 320 and 294 cm^{-1} are related to the symmetric vibrations and torsional motions in [WO_6] distorted clusters. Present data are in good agreement with previous results reported in the literature.[31]

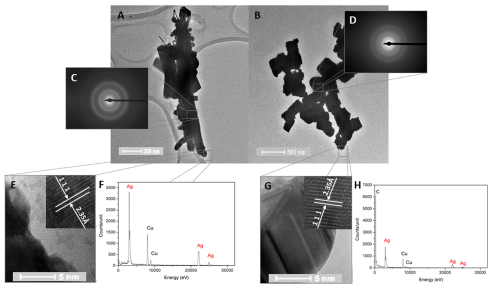

FIGURE 6 – TEM images for (A) α-Ag_2WO_4-R and (B) α-Ag_2WO_4-C samples. SAED analysis for (C) α-Ag_2WO_4-R and (D) α-Ag_2WO_4-C samples. HR-TEM images: (E) α-Ag_2WO_4-R and (G) α-Ag_2WO_4-C. EDS local elementary analysis: (F) α-Ag_2WO_4-R and (H) α-Ag_2WO_4-C. The inset in (E) and (G) present the calculated interplanar distance corresponding to cubic Ag metal at the α-Ag_2WO_4-R, and α-Ag_2WO_4-C samples, respectively.

Figure 7B presents the Raman scattering spectra and the vibrational modes in the range of 50−1200 cm^{-1} at room temperature. Although there are 21 known vibrational modes for α-Ag_2WO_4 ($6A_{1g}$, $5A_{2g}$, $5B_{1g}$, and $5B_{2g}$)[32] it is possible to detect 12 of them for both samples. According to Turkovic et al.,[32] there are two active A_{1g} external modes within the region of smaller wavenumbers, at 44 and 60 cm^{-1}, that are due to the translational movements of Ag cations in a rigid molecular unit. In our spectra, it is possible to observe, for both materials, an intense band at ~58 cm^{-1}. This peak is identical in intensity and definition for both samples. The active modes between 500 to 100 cm^{-1} are related to external vibrational modes of [AgO_n] (n = 7, 6, 4, 2).[28] Although this region presents lower-intensity bands, it seems to indicate some slight differences between the spectra. There is an intense band at 878 cm^{-1}, attributed to the symmetric stretching of the W−O bond in [WO_6] octahedral clusters. The active modes, between 500 and 1000 cm^{-1}, can be assigned to the vibrations in [WO_6] clusters. This result confirms that the Raman spectra are the result of the presence of short-range order at the [AgO_n] clusters within the crystal lattice.

UV-Vis Optical Spectroscopy Analysis. The optical band-gap energy (E_{gap}) values for both α-Ag_2WO_4 samples were determined by UV-Vis spectroscopy. With the utilization of the Wood and Tauc method[33] we could estimate the energy gaps of the materials. The spectra obtained were converted to the Kubelka-Munk function, by the method proposed by Kubelka and Munk-Aussig[34], which is a reliable method to estimate E_{gap} values with good accuracy within the limits of assumptions in three dimensions.

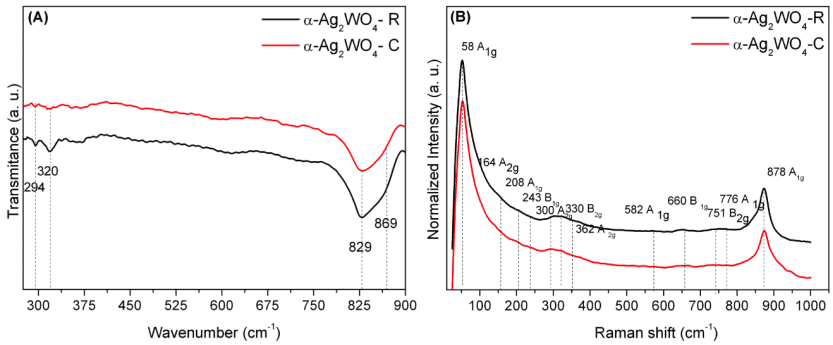

FIGURE 7 – (A): FT-IR spectra of α-Ag_2WO_4 microcrystals prepared by the CP method at 90 ºC without (black line color) and with (red line color) the presence of SDS. The vertical dashed lines indicate the position of the IR peaks and IR-active modes. (B): Raman spectroscopy of α-Ag_2WO_4 microcrystals prepared by the CP method at 90 ºC without (black line color) and with (red line color) the presence of SDS. The vertical dashed lines indicate the position of the Raman peaks and active modes.

According to Kim *et al.*[35] and Tang *et al.*[36], Ag_2WO_4 crystals exhibit an optical absorption spectrum governed by direct electronic transitions between the valence band (VB) and conduction band (CB). Based on this information, the E_{gap} values of our α-Ag_2WO_4 crystals were calculated using n = 0.5.

UV-vis spectroscopy provides structural information in terms of the structure of electronic bands and the level of organization at both short- and medium-range. A characteristic behavior of UV-Vis absorbance curves is the formation of an exponential decay within the regions of lesser energies known as Urbach Tail.[33] This decay is associated with the presence of an intermediate-energy band gap. The gradient of the linear extrapolation on this "tail" correlates with the amount of disorder in the material: the less steep the linear extrapolation on this "tail", the more disordered is the material. Because Ag_2WO_4 is composed of several different clusters ([WO_6], [AgO_7], [AgO_6], [AgO_4], [AgO_2]), with weak interactions between the O−W and O−Ag bonds, the relative positions of the atoms (W, O, Ag) can vary. These variations can affect both bond lengths and angles, which causes a redistribution of the electronic density and the energy band structure, thus changing the band gap value. Reported experimental values are in the range of 3.09 eV and 3.23 eV,[11,14] depending on the synthesis method employed. We obtained a E_{gap} value of 3.20 eV for the α-Ag_2WO_4-R and 3.13 eV for the α-Ag_2WO_4-C (Figure 8). Both values fall within the range of values previously reported. Although the differences in value might be small, it could be related to the individual band gaps of each surface given that the E_{gap} value is the result of bulk and surface contributions. Moreover, one might consider the influence of some possible defects, such as structural distortions, associated with changes in bond lengths and angles, atomic dislocation, local coordination changes, oxygen vacancies, etc.[37]

The presence of such defects is very dependent on the synthesis parameters, such as solvent, time, temperature, pressure, surfactants or contaminants. From an electronic point of view, these defects generate intermediate energy states in the forbidden region between the VB and CB, while an increase of the E_{gap} values can be attributed to a reduction in the number of defects and, subsequently, in the number of electronic levels within the forbidden band gap.

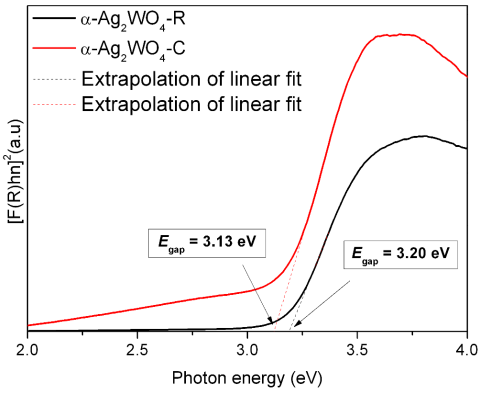

FIGURE 8 – UV-vis spectra of α-Ag_2WO_4-R (black line color) and α-Ag_2WO_4-C (red line color).

Photoluminescence emissions. PL is an optical property that conveys information about the electronic states and about the level of structural organization in the intermediate range. PL emissions are dependent on the synthesis conditions, and on the presence of impurities, distortions and deformations of the clusters, etc.[37] For this reason, PL measurements can be used as a complementary tool to X-Ray diffraction, FT-Raman, and UV-Vis spectroscopy to obtain information about the level of order-disorder and defect density of the material. It can also help to explain the appearance of intermediate states between the VB and CB.

α-Ag_2WO_4 has PL emission at room temperature with a broadband character.[38] This is typical of materials where the relaxation step occurs in several paths, with the participation of several energy states within the band gap, according to the broadband model. This broadband is generally composed of blue and green light components, which indicates a high level of mainly shallow defects. This emission is attributed to intrinsic transitions of the $[WO_4]^{2-}$ clusters, as well as charge transfer processes between distorted $[WO_6]$ to undistorted $[WO_6]$ clusters,[39] which generates shallow defects adjacent to the bands.

Figure 9 presents the PL spectra at room temperature. Both samples show PL emissions from 380 to 800 nm. We can observe that the PL behavior of α-Ag_2WO_4-R presents a broadband with maximum emission at 452 nm, corresponding to the blue region of the electromagnetic spectrum. Though the α-Ag_2WO_4-C also presents emission in the blue region (456 nm), this band is much less intense, and the curve is much more shifted into the whole spectrum, with emission in the red region (640 nm) with almost the same intensity of the blue emission peak. This behavior can be associated with the decreasing number of distorted $[WO_6]$ clusters and increasing presence of distorted $[AgO_n]$ (n = 7,6, 4 and 2) clusters, that can be attributed to oxygen vacancies, which induce more disorder to the material and more deep defects in the forbidden region.

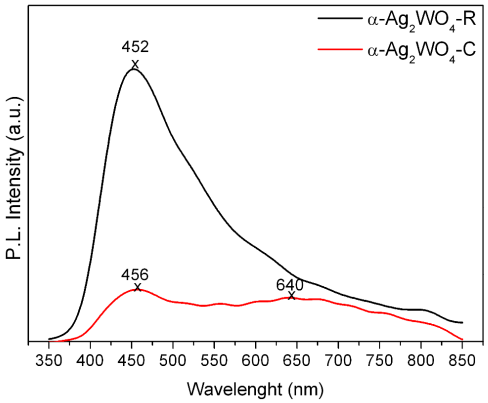

FIGURE 9 – PL spectra of α-Ag_2WO_4-R (black line color) and α-Ag_2WO_4-C (red line color).

Morphology control. Surface energy does not only dictate the surface structure and stability, but is also a fingerprint to measure the catalytic activity and selectivity, as well as to follow the degradation process and the crystallization pathway. The surface energy value provides insight into the resistance of a given material to sintering, ripening, and in dissolution processes. Surface energy is not a constant material property and may depend on the environment that surrounds the surface, such as the adsorption of a reactant, surfactant or any species present in the solution, which can promote the stability of a particular surface, structure, or facet. Therefore, the control of the crystal morphology is a complex process depending on several factors related to crystal internal structures and external agents. Hence, the synthesis process can have a strong influence on the final product. In our study, when the anionic surfactant SDS is included in the synthesis of α-Ag_2WO_4, the result indicates that SDS works as a morphology-controlling agent.

It is well established that, during crystal growth, the shape evolution is controlled by the surface energy of each face. Under equilibrium conditions, faces with high surface energies tend to grow rapidly so that they usually disappear in order to minimize the total surface energy.[40] In a given environment, driven by the experimental conditions, the surface energies of different surfaces can be effectively decreased by the selective adsorption of appropriate inorganic or organic agents.[41]

Bakshi[22] showed that the adsorption of a surfactant in aqueous media takes place through bilayer formation. The polar heads of surfactant molecules adhere to the charged nanoparticle surfaces, exposing the organic surfactant tails to the bulk solution, where they are insoluble. A second surfactant layer adsorbs to the first one, making a bilayer. This kind of adsorption is usually selective to a specific crystal plane, which leads to an ordered shape evolution. Hydrophobicity is a very important characteristic in surfactant action and has a strong correlation with the final morphology. The cubic shape is usually generated in the presence of a highly hydrophobic medium.

In this way, the surface plays an important role in the material growth process and it is fundamental to study the atomic arrangement on each surface. Table 2 presents the surface energy values for each surface.[24] By employing the Wulff construction we can obtain the ideal morphology of α-Ag_2WO_4, as well as the experimentally observed hexagonal rod-like, α-Ag_2WO_4-R (see Figure 4B), and the cuboid-like α-Ag_2WO_4-C (see Figure 4D) morphologies. The E_{surf} values show the following stability order: (010) < (100) < (001) < (110) < (101) < (011).

Figure 10 displays the six low-index surfaces of α-Ag_2WO_4. At the top of each surface, there are different kinds of under-coordinated Ag and/or W cations with respect to the bulk. These local coordinations, associated to incomplete $[AgO_n]$ and $[WO_6]$ clusters,

allows us to find the number of broken Ag−O and W−O bonds. Then, the Kröger-Vink notation[42] can be employed to assign the number and type of oxygen vacancies, $[V_O^x]$.

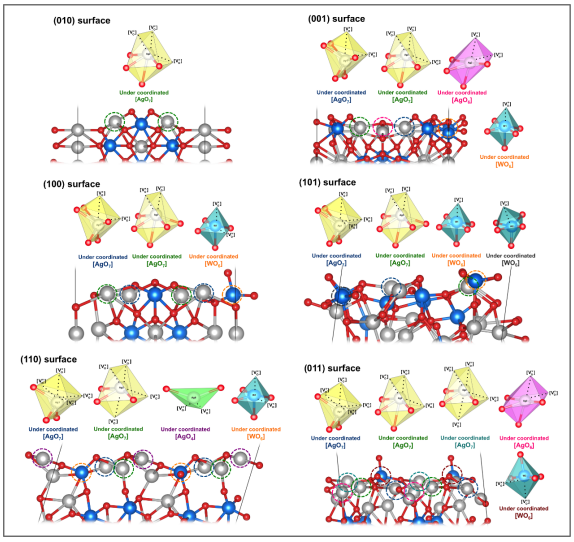

FIGURE 10 – Under-coordinated Ag and W clusters at the (010), (001), (100), (101), (110) and (011) surfaces of the α-Ag_2WO_4.

An analysis of the results presented in Table 2 and Figure 10, indicates that the most stable surface, (010), presents only one type of under-coordinated cluster $[AgO_4 \cdot 3V_O^x]$ at the Ag1 cation. In the (100) surfaces, Ag1 and Ag2 cations appear under-coordinated with $[AgO_5 \cdot 2V_O^x]$ clusters and $[WO_4 \cdot 2V_O^x]$ clusters are observed for the W1 cation. In the (001) surface shows the $[AgO_5 \cdot 2V_O^x]$, $[AgO_4 \cdot 3V_O^x]$ and $[AgO_4 \cdot 2V_O^x]$ clusters associated to the Ag1 and Ag2, and Ag3 cations, respectively, while there are $[WO_5 \cdot V_O^x]$ clusters at the W1 cation. In the case of the (110) surface, $[AgO_4 \cdot 3V_O^x]$ clusters for Ag1 and Ag2 cations, $[AgO_2 \cdot 2V_O^x]$ clusters for the Ag5 cation, and $[WO_4 \cdot 2V_O^x]$ clusters for the W1 cation are found. The (101) surface is formed by $[AgO_4 \cdot 3V_O^x]$ and $[AgO_5 \cdot 2V_O^x]$ clusters of Ag1 and Ag2 cations, respectively, and $[WO_5 \cdot V_O^x]$ clusters for W1 and W2 cations. At the most unstable surface (011), there are five different kinds of clusters: $[AgO_4 \cdot 3V_O^x]$ clusters for Ag1 cations, $[AgO_4 \cdot 3V_O^x]$ and $[AgO_3 \cdot 4V_O^x]$ clusters for Ag2 cations, $[AgO_4 \cdot 2V_O^x]$ clusters for Ag3 cations and $[WO_4 \cdot 2V_O^x]$ clusters for W3 cations.

TABLE 2 – Surface Energy Values (E_{surf}, eV), Contribution of the Surface Area by the Total Area (C_i, %) and the Polyhedron Energy ($E_{polyhedron}$, eV) for Each Morphology of α-Ag_2WO_4.

Surface	E_{surf} (C_i)		
	α-Ag_2WO_4-Ideal	**α-Ag_2WO_4-R**	**α-Ag_2WO_4-C**
(010)	0.20 (52.5)	0.80 (14.4)	0.20 (33.3)
(100)	0.38 (27.6)	0.70 (0.00)	0.20 (33.3)
(001)	0.53 (19.9)	0.20 (35.6)	0.20 (33.3)
(110)	0.65 (0.00)	1.10 (0.00)	1.10 (0.00)
(101)	0.68 (0.00)	0.32 (50.0)	0.68 (0.00)
(011)	0.83 (0.00)	0.83 (0.000)	0.83 (0.00)
$E_{polyhedron}$	0.31	0.35	0.20

TABLE 2 – (cont.) Surface Energy Values (E_{surf}, eV), Contribution of the Surface Area by the Total Area (C_i, %) and the Polyhedron Energy ($E_{polyhedron}$, eV) for Each Morphology of α-Ag_2WO_4.

Surface	E_{surf} (C_i)						
	A	**B**	**C**	**D**	**E**	**F**	**G**
(010)	0.20 (45.7)	0.20 (44.4)	0.20 (40.3)	0.50 (18.6)	0.80 (14.4)	0.20 (39.6)	0.20 (42.1)
(100)	0.38 (15.0)	0.70 (0.00)	0.70 (0.00)	0.70 (0.00)	0.70 (0.00)	0.38 (20.8)	0.20 (42.1)
(001)	0.53 (0.00)	0.53 (0.00)	0.20 (24.8)	0.20 (35.4)	0.20 (35.6)	0.20 (39.6)	0.53 (15.8)
(110)	0.65 (0.00)	0.65 (0.00)	0.65 (0.00)	0.65 (6.50)	1.10 (0.00)	0.65 (0.00)	0.65 (0.00)
(101)	0.32 (39.3)	0.32 (55.6)	0.32 (34.9)	0.32 (39.5)	0.32 (50.0)	0.68 (0.00)	0.68 (0.00)
(011)	0.83 (0.00)	0.83 (0.00)	0.83 (0.00)	0.83 (0.00)	0.83 (0.00)	0.83 (0.00)	0.83 (0.00)
$E_{polyhedron}$	0.27	0.27	0.24	0.33	0.35	0.24	0.25

Therefore, we can confirm that there is a relationship between the presence of a large amount of under-coordinated clusters at the surface and the surface energy values.[38]

A detailed analysis comparing the two different surfaces in the α-Ag_2WO_4-R and α-Ag_2WO_4-C morphologies, namely the (101) and (100) exposed facets (see Figure 10), indicates that both surfaces have Ag1 and Ag2 cations at the top of each surface, but the (101) surface presents more under-coordinated [WO_6] clusters near the top of the surface with respect to the (100) surface.

The natural starting point for predicting morphology type is to establish the relative stabilities of all surfaces, where the lowest surface energy will be thermodynamically preferred. While it is well-established that the kinetics required to reach different morphologies from a specific precursor state can often

be manipulated by the presence of a surfactant to result in the synthesis of another morphology, the relative stability of kinetically-accessible morphologies then falls within a fairly narrow range of energies. The relative stabilities of each morphology can be directly modified if they are grown in the presence of a surfactant. The surface energies of the different facets can be modified by interaction with the surfactant, which causes reordering in their relative stabilities.

Wulff's crystal representation of the optimized α-Ag_2WO_4 is depicted in the central part of Figure 9, and the different morphologies, hexagonal rod-like α-Ag_2WO_4-R and cuboid-like α-Ag_2WO_4-C, can be obtained by assuming different values for the surface energies of the different facets. This interpretation has the advantage that all faces grow from the initial α-Ag_2WO_4 crystal (α-Ag_2WO_4-Ideal), depending on their surface energy value.

From the calculated values of polyhedron energies reported in Table 2, we can obtain the energy profile that links the ideal morphology to the experimentally observed hexagonal rod-like, α-Ag_2WO_4-R (see a Reaction Path (A) on Figure 11), and cuboid-like α-Ag_2WO_4-C (see Reaction Path (B) on Figure 11) morphologies. Figure 11 illustrates the good agreement between the experimental and theoretical morphologies. The principal idea of this representation is that the α-Ag_2WO_4-R and α-Ag_2WO_4-C, associated to stable morphologies, can be energetically related to the ideal morphology along two alternative pathways via intermediates A-G.

The pathway depicted in Figure 11A involves five steps: the first one is achieved by decreasing the value of E_{surf} of the (101) surface with appearance of the A morphology, followed by two stages related to an increase and decrease in the values of E_{surf} for the (100) and the (001) surfaces, with formation of the B and C morphologies, respectively. The C morphology resembles the experimental α-Ag_2WO_4-R (see Figure 4A); however, it is not elongated, as seen in Figure 4B. From C and by increasing the values of E_{surf} for the (010) surface, an intermediate D morphology is reached and by increasing the value of E_{surf} for the (010) surface, the E morphology is obtained, corresponding to a maximum value of $E_{polyhedron}$. Finally, by increasing the value of E_{surf} for the (110) surface, the α-Ag_2WO_4-R morphology is achieved (see Figure 4B). Along this pathway, there is an energy barrier in the fourth step.

The pathway depicted in Figure 11B corresponds to the process linking the α-Ag_2WO_4-C morphology and the ideal morphology. This path involves a decreasing in E_{surf} values for the (100) and (001) surfaces and is a barrier-less process, via E and F morphologies. This is the energetically favorable path and allows us to explain the effect of the anionic surfactant SDS in the synthesis process. As observed in the FE-SEM images in Figure 4C and 4D, the Ag_2WO_4-C morphology can be cubic and elongated-cubic. In this way, the four morphologies (ideal from theoretical calculations, F, G and Ag_2WO_4-C morphologies from Figure 11B) involved in the pathway can be associated with the crystal obtained by the CP method at 90 ºC with anionic surfactant SDS since that Ag_2WO_4-C morphology is formed by the combination of (010), (100) and (001) surfaces.

The order of stability of α-Ag_2WO_4 morphologies is α-Ag_2WO_4-C < α-Ag_2WO_4 ideal < α-Ag_2WO_4-R, as shown in Figure 11. The presence of the anionic surfactant SDS in the synthesis of the α-Ag_2WO_4 crystal prevents the formation of α-Ag_2WO_4-R, resulting in the disappearance of (101) surface and the appearance of the (100) surface to render the α-Ag_2WO_4-C morphology. Analysis of Figure 11B indicates that the anionic surfactant SDS interacts with and stabilizes the (100) and (001) surfaces, mainly on the Ag cations of the under-coordinated clusters. SDS also prevents increase of E_{surf} of the (010) surface to form the elongated hexagonal rod-like morphology, α-Ag_2WO_4-R.

SDS has proven to be an appropriate morphology-directing agent in the CP synthesis of α-Ag_2WO_4. This is primarily related to the surface adsorption of the anionic part of the surfactant on the different crystal surfaces, thus controlling their overall morphology. This kind of adsorption is usually selective to a specific crystal plane, because the active centers of the surface are mainly associated to under-coordinated Ag cations, i.e. [AgO_n] clusters, and consequently, such adsorption leads to an ordered morphology evolution.

Photocatalytic degradation. The structural analysis of both synthesized samples of α-Ag_2WO_4 shows that the main difference between the samples is related to surface effects. There are no significant differences in the results of XRD, FT-IR and FT-Raman spectroscopy between both morphologies. PL analysis, however, showed significant differences in the types of defects. These experimental results, combined with the theoretical simulation of the surfaces and clusters, indicates that the behavior observed in photocatalytic reactions, is due, exclusively, to morphological aspects, and a particular

crystal plane enhances both the reduction/oxidation sites and the photocatalysis process.[44]

Generally, the photocatalytic process involves the following three steps: i) the absorption of photons with energy larger than the band gap of the photocatalyst; ii) the generation, separation, migration or recombination of photogenerated electron-hole pairs and iii) the redox reactions on the photocatalyst surface. The degradation process of RhB is based on an oxidative attack by active oxygen species on an N-ethyl group. The loss of an ethyl group (N,N,N´-tri-ethylated) at RhB has λ_{max} = 539 nm, the loss of two ethyl groups, that results in N,N´- di-ethylated Rhodamine has a λ_{max} = 522 nm, the N´-ethylated Rhodamine (λ_{max} = 510 nm), and the de-ethylated form present a λ_{max} = 498 nm.[45]

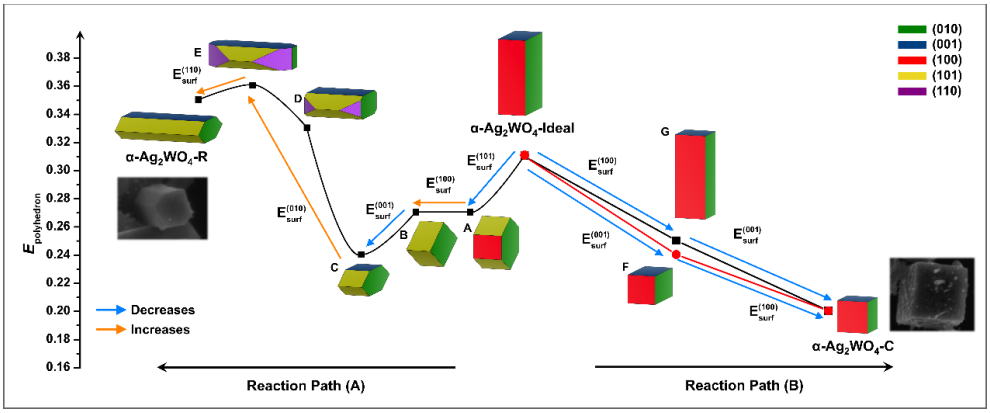

FIGURE 11 – Schematic representation of the energy profile to obtain the (A) α-Ag_2WO_4-R and (B) α-Ag_2WO_4-C morphologies. The intermediate morphologies are indicated as A, B, C, D, E, F and G, obtained by decreasing/increasing the E_{surf} values involved in the process. Experimental FE-SEM images of α-Ag_2WO_4-R and α-Ag_2WO_4-C morphologies of the studied samples are included for comparison.

We monitored the degradation process by analyzing the maximum absorption bands of the RhB spectra as a function of time for both α-Ag_2WO_4-R and α-Ag_2WO_4-C samples. The photocatalytic activities of the α-Ag_2WO_4-R and α-Ag_2WO_4-C samples are given in Figures 12A and 12B, respectively. The degradation of RhB UV radiation without photocatalyst or in the dark in the presence of photocatalyst is carried out in order to understand the influence of the light or photocatalyst. The photocatalytic degradation of RhB follows pseudo first-order kinetics, exhibiting a linear relationship between log(C_0/Ct) and the reaction time. Analysis of Figure 12A indicates that a significant reduction (almost 80%) at the absorption maximum of the RhB solution after 120 min of reaction in the presence of α-Ag_2WO_4-R as catalyst. This result correlates well with the results found in the literature for the same catalyst and conditions.[7] However, the control experiment showed that without a photocatalyst and with α-Ag_2WO_4-C, RhB hardly decomposed during photolysis over a period of 120 min. Analysis of Figures 12A and 12B indicates that RhB exhibits one band with maximum absorption at 554 nm. In addition, Figure 12A also illustrates a significant decrease in the height of the absorption maximum of RhB during the photodegradation process, while Figure 12B shows that after 120 min, a small percentage of the dye was degraded (only 37%). This value is quite close to that of the photolysis reaction in the absence of a catalyst.

Figures 12C and 12D display the linear plots of the standard kinetic data curves obtained for the RhB photodegradation process. The discoloration reaction follows first-order kinetics and can be described by the relationship d[C]/dt = *k*[C], where [C] is the RhB concentration, and *k* indicates the overall photodegradation rate constant and activity. By plotting log(C/C_0) as a function of time through linear regression, where C_0 is the initial concentration of RhB and C is the concentration at time, t, we obtained the constant, *k* (min^{-1}), for the photocatalysis under UV-Vis irradiation of each sample, from the gradients of the simulated straight lines. The corresponding values of *k* for both Ag_2WO_4-R and Ag_2WO_4-C are 4.3 x 10^{-3} min^{-1} and 1.8 x 10^{-3} min^{-1}, respectively, while the corresponding value without a catalyst is 2.1 x 10^{-3} min^{-1}. These results point out that only the α-Ag_2WO_4-R is working as a catalyst, whereas the cuboid-like morphology of α-Ag_2WO_4 negatively affects the photocatalytic activity of α-Ag_2WO_4. For comparison purposes, the value reported for commercial TiO_2 anatase (Aldrich, 99.7%), under similar experimental conditions is *k* = 2.48 (min^{-1}); this is a widely applied standard for several authors.[41]

Several factors can influence reaction rate, namely the structural defects ascribed to ordered-disordered clusters, crystallographic preferred orientation, intermediate electronic levels, high surface energy, roughness, high active surface area, facets,

and so on.[47] The presence of residual anionic surfactant can also contribute to a lower photocatalytic efficiency, acting as hole scavengers.[48] However, we ensured the complete removal of surfactant, as verified by TGA (Supporting Information, SI). According to BET data, α-Ag_2WO_4 possess a surface area of 3.72 m^2/g for the α-Ag_2WO_4-R, and only 1.22 m^2/g for the α-Ag_2WO_4-C. The larger surface area for the α-Ag_2WO_4-R in relation to α-Ag_2WO_4-C is in agreement with the superior performance as photocatalyst of α-Ag_2WO_4-R with respect to α-Ag_2WO_4-C.

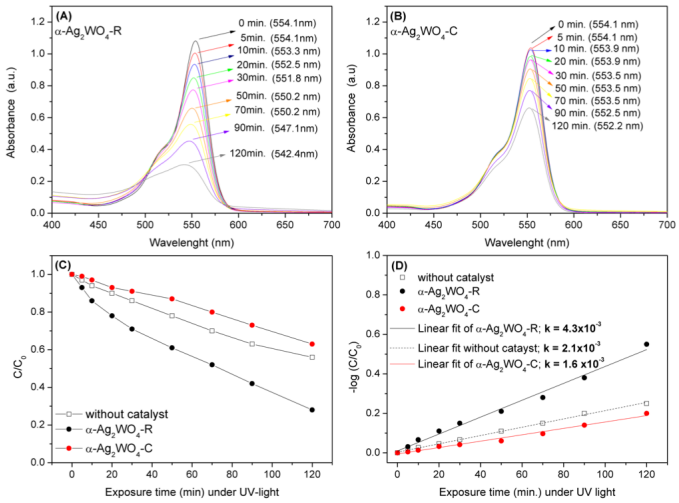

FIGURE 12 – Evolution of UV-vis absorption spectra after 120 min of illumination for the degradation of Rh(B) by the (A) α-Ag_2WO_4-R and (B) α-Ag_2WO_4-C crystals. (C) Photocatalysis degradation profiles of RhB with α-Ag_2WO_4 crystals. (D) First-order kinetics of the samples.

Each surface defect can act as an adsorption site for oxygen and water. The disordered [WO_6] and [AgO_n] clusters are located in intermediate levels near the valence bond (VB), so they interact with H_2O and O_2 molecules from the solution, by adsorption, during the photo-oxidation process. In this manner, the ordered [WO_6] and [AgO_n] clusters that are located below the CB can react with the O_2 molecules, adsorbed on the disordered clusters, by electron transference.

In the presence of air or oxygen, irradiated semiconductors can destroy many organic contaminants. The activation of Ag_2WO_4 by light (hv) produces electron-hole pairs, which are powerful oxidizing and reducing agents, respectively.

In the degradation of organic compounds (such as RhB), the hydroxyl radical, OH*, which comes from the oxidation of adsorbed water, is the primary oxidant; and the presence of oxygen can prevent the recombination of hole-electron pairs.

Water photooxidation: $2H_2O + 4h^{\bullet} \rightarrow O_2 + H^{\bullet}$ (2)

Proton and radical generation: $H_2O + h^{\bullet} \rightarrow H^{\bullet} + OH^*$ (3)

As observed for the α-Ag_2WO_4 semiconductor there are different $[MO_x \cdot xV_O^x]$ clusters, located on the top of the surface and there are also $[MO_6]'_o$ polarized clusters located in the structure, where M = Ag and/or W. These clusters, in turn, can interact with H_2O and O_2 molecules, respectively, to generate OH*, $H^{\bullet}$ and O_2'. The $H^{\bullet}$ species are unstable, and quickly interact with the superoxide radical anion (O_2') forming the perhydroxyl radical (O_2H^*). This is followed by the degradation of RhB by OH* and O_2H^* radicals, in a cyclic process, which ends with formation of the colorless organic compounds (COC), carbon dioxide (CO_2) and water (H_2O).[44]

$O_2' + H^{\bullet} \rightarrow O_2H^*$ (4)

$RhB + O_2H^* + OH^* \rightarrow COC + CO_2 + H_2O$ (5)

For the generation of all the reactive oxygen species, strong adsorption of oxygen molecule, O_2, with concomitant electron transfer process from the oxygen vacancies[45] is necessary. In our case, both distorted [WO_6] and [AgO_n] clusters possess different electron density and oxygen vacancies with the capability of produce electron-hole pairs. However, thanks to the different nature of the Ag−O and W−O bonds within these clusters, the lability and the stability of these vacancies change according to the Ag/W under-coordinated clusters. The predominant presence of the surface (101) is responsible for the hexagonal rod-like morphology, α-Ag_2WO_4-R, in which present under-coordinated Ag and W cations to be active for the RhB photocatalytic degradation.

Although the hexagonal rod-like morphology, α-Ag_2WO_4-R, imparts a photocatalytic effect, its activity is much lower than other common catalysts, like TiO_2. Roca and co-workers[5] synthesized other more energetic facets of α-Ag_2WO_4 by means of the microwave-assisted hydrothermal method, which is a

very efficient method, but with several limitations mentioned previously. We show here that the simple use of a surfactant in a short time reaction can efficiently promote changes in morphology that directly influence the final properties of α-Ag_2WO_4.

Conclusions

Good crystal facet engineering is crucial for the successful synthesis of semiconductor materials with functional applications. To develop functional materials, it is important to control their morphology and structure. The fundamental issue is a lack of in-depth knowledge about nanoparticle formation and crystallization mechanisms and about their surface chemistry. It is important to point out that the chemical environment strongly influences the growth and morphology of the crystals. Altering environmental parameters, for instance by including surfactants, may result in modification of the surface energies of crystal faces and, consequently, the crystals obtained can present different morphologies.

The main conclusions of the present study can be summarized as follows: i) We have experimentally obtained the cuboid-like morphology of α-Ag_2WO_4-C using a simple controlled-precipitation method with the anionic surfactant SDS dissolved in a sodium tungstate solution. ii) Although the Wulff construction, obtained by first-principles calculations, renders that the ideal morphology of α-Ag_2WO_4 is the cube, this morphology is not spontaneously reached by the simple combination of those precursors in the aqueous medium. iii) α-Ag_2WO_4-C morphology is composed of the (001), (010) and (100) surfaces, and the adsorption of the SDS anionic head on the (100) facet provokes the stabilization of the (100) surface and prevents the growth process along the (101) surface. iv) By calculating the energy profiles connecting these morphologies, a deeper insight, at atomic level, on the role of SDS surfactant is achieved, and hence, SDS has been successfully used as a morphology-controlling agent for the synthesis of α-Ag_2WO_4-C. v) The calculated energy profile, based on the Wulff construction, points out that the anionic surfactant SDS interacts with and stabilizes the (100) and (001) surfaces, mainly on the Ag cations of the under-coordinated clusters. Additionally, the SDS prevents the increase of E_{surf} of the (010) surface to form the elongated hexagonal rod-like morphology, α-Ag_2WO_4-R. vi) Analysis of the type and number of under-coordinated clusters of each surface suggests that on the (100) surface are mainly under-coordinated [AgO_7] clusters, with a little contribution of under-coordinated [WO_6] clusters, while the (101) surface is mainly formed by under-coordinated [WO_6] clusters, with a minor contribution of under-coordinated [AgO_7] clusters. vii) Correlation between the exposed surfaces and photocatalytic activity was revealed, and an explanation of this behavior, arising from different morphologies and structural data, was provided. viii) Theoretical calculations confirm the rationality of the experimental scheme and elucidate the underlying reason for the photodegradation process of Rhodamine B.

These results highlight the importance of considering the chemical environment and the adsorption of surfactant along with the synthetic route when determining the stability and activity of a catalyst with a defined morphology. Our model also reveals some details about the mechanism involved and gives some important information about how to improve photocatalytic activity by designing the morphology of the patterned surface or improving the synthesis conditions or restructuring/shape control techniques.

Rather than individual numbers, the most important outcomes of these simulations are the general, chemical trends they have revealed. There, and here, predictive atomistic simulations are likely to play an increasingly important role. The rationally-controlled chemical synthesis of well-defined morphologies may open up a valuable synthetic route, and, in terms of future perspectives, this morphology control strategy can be extended to explore other Ag based materials, where shape is the most important characteristic for application.

Acknowledgments

The authors acknowledge the financial support from Fundação de Amparo à Pesquisa do Estado de São Paulo (FAPESP 2012/14004-5, 2013/07296-2, 2017/07240-8 and 2013/26671-9), Conselho Nacional de Desenvolvimento Científico e Tecnológico (CNPq 439234/2016-6, 150205/2017-1 and 166281/2017-4), Generalitat Valenciana (PrometeoII/2014/022, Prometeo/2016/079, ACOMP/2014/270, ACOMP/2015/1202), Ministerio de Economia y Competitividad, (project CTQ2015-65207-P), and Programa de Cooperación Cientifica con Iberoamerica (Brasil) of Ministerio de Educación (PHBP14- 00020). We also thank Prof. Dr. Máximo S. Li, from IFSC-USP, USP, São Carlos, SP, Brazil for his help with photoluminescence measurements, Prof. Dr. Ernesto Antonio Urquieta Gonzales, from Chemistry Engineering Department (DEQ) – UFSCar, São Carlos, SP, Brazil for the BET analysis.

References

1.Kant, R. Textile Dyeing Industry an Environmental Hazard. *Nat. Sci.* **2012,** *04*, 22-26.

2. Mai, L.; Xu, L.; Gao, Q.; Han, C.; Hu, B.; Pi, Y. Single Beta-$AgVO_3$ Nanowire H_2S Sensor. *Nano Lett.* **2010**, *10*, 2604-2608.

3. Xu, Z.; kibria, Md. Z.; AlOtaibi, B.; Duschesne, P. N.; Besteiro, L. V.; Gao, Y.; Zhang, Q.; Mi, Z.; Zhang, P.; Govorov, A. O. et al. Towards Enhancing Photocatalytic Hydrogen Generation: Which Is More Important, Alloy Synergistic Effect or Plasmonic Effect? *Appl. Catal. B: Environ*. **2018**, *221*, 77-85.

4. Teh, C. M.; Mohamed, A. R. Roles of Titanium Dioxide and Ion-Doped Titanium Dioxide on Photocatalytic Degradation of Organic Pollutants (Phenolic Compounds and Dyes) in Aqueous Solutions: A Review. *J. Alloys Compd.* **2011,** *509*, 1648-1660.

5. Panthi, G.; Park, M.; Kim, H.-Y.; Lee, S.-Y.; Park, S.-J. Electrospun ZnO Hybrid Nanofibers for Photodegradation of Wastewater Containing Organic Dyes: A Review. *J. Ind. Eng. Chem.* **2015,** *21*, 26-35.

6. Kumar, S. G.; Rao, K. S. R. K. Comparison of Modification Strategies Towards Enhanced Charge Carrier Separation and Photocatalytic Degradation Activity of Metal Oxide Semiconductors (TiO_2 , WO_3 and ZnO). *Appl. Surf. Sci.***2017,** *391*, 124-148.

7. Roca, R. A.; Sczancoski, J. C.; Nogueira, I. C.; Fabbro, M. T.; Alves, H. C.; Gracia, L.; Santos, L. P. S.; de Sousa, C. P.; Andrés, J.; Luz, G. E.; Longo, E.; et al. Facet-Dependent Photocatalytic and Antibacterial

Properties of α-Ag_2WO_4 Crystals: Combining Experimental Data and Theoretical Insights. *Catal. Sci. Technol.* **2015,** *5*, 4091-4107.
8. Wang, X.; Fu, C.; Wang, P.; Yu, H.; Yu, J. Hierarchically Porous Metastable Beta-Ag_2WO_4 Hollow Nanospheres: Controlled Synthesis and High Photocatalytic Activity. *Nanotechnol.* **2013,** *24,* 165602(8pp).
9. Chen, H.; Xu, Y. Photoactivity and Stability of Ag_2WO_4 for Organic Degradation in Aqueous Suspensions. *Appl. Surf. Sci.* **2014,** *319*, 319-323.
10. van den Berg, A. J.; Juffermans, C. A. H. The Polimorphism of Silver Tungstate. *J. Appl. Crist.* **1982,** *15*, 114-116.
11. De Santana, Y. V. B.; Gomes, J. E. C.; Matos, L.; Cruvinel, G. H.; Perrin, A.; Perrin, C.; Andrès, J.; Varela, J. A.; Longo, E. Silver Molybdate and Silver Tungstate Nanocomposites with Enhanced Photoluminescence. *Nanomater. Nanotechnol.* **2014,** *4*, 22(10pp).
12. Dutta, D. P.; Singh, A.; Ballal, A.; Tyagi, A. K. High Adsorption Capacity for Cationic Dye Removal and Antibacterial Properties of Sonochemically Synthesized Ag_2WO_4Nanorods. *Eur. J. Inorg. Chem.* **2014,** *2014*, 5724-5732.
13. da Silva, L. F.; Catto, A. C.; Avansi, W.; Cavalcante, L. S.; Mastelaro, V. R.; Andrés, J.; Aguir, K.; Longo, E. Acetone Gas Sensor Based on α-Ag_2 WO_4 Nanorods Obtained Via a Microwave-Assisted Hydrothermal Route. *J. Alloys Compd.* **2016,** *683*, 186-190.
14. Cavalcante, L. S.; Almeida, M. A. P.; Avansi, W.; Tranquilin, R. L.; Longo, E.; Batista, N. C.; Mastelaro, V. R.; Li, M. S. Cluster Coordination and Photoluminescence Properties of α-Ag_2WO_4 Microcrystals. *Inorg. Chem.* **2012,** *51*, 10675-10687.
15. Andrés, J.; Gracia, L.; Gonzalez-Navarrete, P.; Longo, V. M.; Avansi, W., Jr.; Volanti, D. P.; Ferrer, M. M.; Lemos, P. S.; La Porta, F. A.; Hernandes, A. C.; et al. Structural and Electronic Analysis of the Atomic Scale Nucleation of Ag on Alpha-Ag_2WO_4 Induced by Electron Irradiation. *Sci.Rep.* **2014,** *4*, 5391(7pp).
16. Derby, J. J.; Atherton, L. J.; Gresho, P. M. An Integrated Process Model for the Growth of Oxide Crystals by the Czochralski Method. *J. Cryst. Grown* **1989,** *97*, 792-826.
17. Cui, X.; Yu, S. H.; Li, L.; Biao, L.; Li, H.; Mo, M.; Liu, X. M. Selective Synthesis and Characterization of Single-Crystal Silver Molybdate/Tungstate Nanowires by a Hydrothermal Process. *Chem.***2004,** *10* (1), 218-223.
18. Nguyen, N. T.; Nguyen, B. H.; Ba, D. T.; Pham, D. G.; Van Khai, T.; Nguyen, L. T.; Tran, L. D. Microwave-Assisted Synthesis of Silver Nanoparticles Using Chitosan: A Novel Approach. *Mater. Manuf. Processes* **2014,** *29* (4), 418-421.
19. George, T.; Joseph, S.; Mathew, S. Synthesis and Characterization of Nanophased Silver Tungstate. *Pramana* **2005,** *65* (5), 793-799.
20. Niu, Z.; Li, Y. Removal and Utilization of Capping Agents in Nanocatalysis. *Chem. Mater.* **2014,** *26*, 72-83.
21. Deshmukh, R.; Niederberger, M. Mechanistic Aspects in the Formation, Growth and Surface Functionalization of Metal Oxide Nanoparticles in Organic Solvents. *Chem.* **2017,** *23*, 8542-8570.
22. Bakshi, M. S. How Surfactants Control Crystal Growth of Nanomaterials. *Crystal Growth & Des.* **2016,** *16*, 1104-1133.
23. Brunauer, S. E., P. H.; Teller, E. Adsorption of Gases in Multimolecuar Layers. *J. Am. Chem. Soc.***1938**, 60, 309-319.
24. Andrés, J.; Gracia, L.; Gouveia, A. F.; Ferrer, M. M.; Longo, E. Effects of Surface Stability on the Morphological Transformation of Metals and Metal Oxides as Investigated by First-Principles Calculations. *Nanotechnol.* **2015,** *26*, 405703(11pp).
25. Ferrer, M. M.; Gouveia, A. F.; Gracia, L.; Longo, E.; Andrés, J. A 3D Platform for the Morphology Modulation of Materials: First Principles Calculations on the Thermodynamic Stability and Surface Structure of Metal Oxides: Co_3O_4,α-Fe_2O_3, and In_2O_3. *Model.Simul. Mater. Sci. Eng.***2016,** *24*, 025007(10pp).
26.Skarstad, P. M.; Geller, S., $(W_4O_{16})^{8-}$ Polyion in the high temperature modification of silver tungstate. *Mater. Res. Bull.* **1975,** *10* , 791-799.
27.Rietveld, H. M. A Profile Refinement Method for Nuclear and Magnetic Structures . *J. Apply. Cryst.* **1969**, 2, 65-71.
28. Longo, V. M., de Foggi, C. C.; Ferrer, M. M.; Gouveia, A. F.; Andrés, R. S.; Avansi, W.; Vergani, C.; E.; Machado, A. L.; Andrés, J.; Cavalcante, L. S.;et al. Potentiated Electron Transference in Alpha-Ag_2WO_4 Microcrystals with Ag Nanofilaments as Microbial Agent. *J. Phys. Chem. A* **2014**, *118*, 5769-78.
29. Longo, E.; Cavalcante, L. S.; Volanti, D. P.; Gouveia, A. F.; Longo, V. M.; Varela, J. A.; Orlandi, M. O.; Andres, J. Direct in Situ Observation of the Electron-Driven Synthesis of Ag Filaments on Alpha-Ag_2WO_4 Crystals. *Sci. Rep.* **2013**, *3*, 1676.
30. Longo, E.; Avansi, W., Jr.; Bettini, J.; Andres, J.; Gracia, L. *In Situ* Transmission Electron Microscopy Observation of Ag Nanocrystal Evolution by Surfactant Free Electron-Driven Synthesis. *Sci. Rep.* **2016**, *6*, 21498.
31. Clark, G. M.; Doyle, W. P. Infra-Red Spectra of Anhydrous Molybdates and Tungstates. *Spectrochim. Acta* **1966,** *22*, 1441-1447.
32. Turkovic, A.; Fox, D. L.; Scott, J. F.; Geller, S.; Ruse, G. F. High Temperature Raman Spectroscopy of Silver Tetratungstate, $Ag_8W_4O_{16}$. *Mater. Res. Bull.* **1977,** *12*, 189-195.
33. Wood, D. L.; Tauc, J. Weak Absorption Tails in Amorphous Semiconductors. *Phys. Rev. B* **1972,** *5*, 3144-3151.
34. Kubelka, P.; Munk, F. Ein Beitrag zur Optik der Farbanstriche. *Z. Techn. Phys.* **1931,** *12*, 593-601.

35. Kim, D. W.; Cho, I.-S.; Lee, S.; Bae, S.-T.; Shin, S. S.; Han, G. S.; Jung, H. S.; Hong, K. S. Photophysical and Photocatalytic Properties of $Ag_2M_2O_7$ (M=Mo, W). *J. Am. Ceram. Soc.* **2010,** *93*, 3867-3872.
36. Tang, J.; Ye, J., Correlation of Crystal Structures and Electronic Structures and Photocatalytic Properties of the W-Containing Oxides. *J.Mater. Chem.* **2005,** *15*, 4246.
37. Sczancoski, J. C.; Cavalcante, L. S.; Joya, M. R.; Varela, J. A.; Pizani, P. S.; Longo, E., $SrMOO_4$ Powders Processed in Microwave-Hydrothermal: Synthesis, Characterization and Optical Properties. *Chem. Eng. J.* **2008**, *140*, 632-637.
38. Lin, Z.; Li, J.; Zheng, Z.; Yan, J.; Liu, P.; Wang, C.; Yang, G. W. Electronic Reconstruction of Ag_2WO_4 Nanorods for the Visible-Light Photocataysis. *ACS Nano* **2015,** *9*, 7256-7265.
39. Longo, E.; Volanti, D. P.; Longo, V. M.; Gracia, L.; Nogueira, I. C.; Almeida, M. A. P.; Pinheiro, A. N.; Ferrer, M. M.; Cavalcante, L. S.; Andrés, J. Toward an Understanding of the Growth of Ag Filaments on α-Ag_2WO_4 and Their Photoluminescent Properties: A Combined Experimental and Theoretical Study. *J. Phys. Chem. C* **2014,** *118*, 1229-1239.
40.Martin, D. J.; Liu, G.; Moniz, S. J.; Bi, Y.; Beale, A. M.; Ye, J.; Tang, J. Efficient Visible Driven Photocatalyst, Silver Phosphate: Performance, Understanding and Perspective. *Chem. Soc. Rev.* **2015,** *44*, 7808-28.
41.Huang, K.; Yuan, L.; Feng, S. Crystal Facet Tailoring Arts in Perovskite Oxides. *Inorg. Chem. Front.* **2015,** *2*, 965-981.
42.Kröger, F. A.; Vink, H. J. Relations Between the Concentrations of Imperfections in Crystalline *Solids* **1956,** *3*, 307-435.
43. Liu, G.; Yu, J. C.; Lu, G. Q.; Cheng, H. M. Crystal Facet Engineering of Semiconductor Photocatalysts: Motivations, Advances and Unique Properties. *Chem. Commun.* **2011,** *47*, 6763-83.
44. Huang, M.; Weng, S.; Wang, B.; Hu, J.; Fu, X.; Liu, P. Various Facet Tunable ZnO Crystals by a Scalable Solvothermal Synthesis and Their Facet-Dependent Photocatalytic Activities. *J. Phys. Chem. C* **2014,** *118*, 25434-25440.
45. Wu, T. L., G.; Zhao, J. Photoassisted Degradation of Dye Pollutants. V. Self-Photosensitized Oxidative Transformation of Rhodamine B Under Visible Light Irradiation in Aqueous TiO_2 Dispersions. *J. Phys. Chem. B* **1998,** *102*, 5845-5851.
46. Akpan, U. G.; Hameed, B. H. Parameters Affecting the Photocatalytic Degradation of Dyes Using TiO_2-based Photocatalysts: A Review. *J. Hazard. Mater.* **2009,** *170*, 520-529.
47. Cavalcante, L. S.; Sczancoski, J. C.; Batista, N. C.; Longo, E.; Varela, J. A.; Orlandi, M. O. Growth Mechanism and Photocatalytic Properties of $SrWO_4$ Microcrystals Synthesized by Injection of Ions into a Hot Aqueous Solution. *Adv. Powder Technol.* **2013,** *24*, 344-353.
48. Horváth, O.; Bodnár, E.; Hegyi, J. Photoassisted Oxidative Degradation of Surfactants and Simultaneous Reduction of Metals in Titanium Dioxide Dispersions. *Colloid. Surf. A: Phys. Eng. Asp.* **2005,** *265*, 135-140.
49. Bomio, M. R. D.; Tranquilin, R. L.; Motta, F. V.; Paskocimas, C. A.; Nascimento, R. M.; Gracia, L.; Andres, J.; Longo, E. Toward Understanding the Photocatalytic Activity of $PbMoO_4$ Powders with Predominant (111), (100), (011), and (110) Facets. A Combined Experimental and Theoretical Study. *J. Phys. Chem. C* **2013,** *117*, 21382-21395.
50. Plantard, G.; Janin, T.; Goetz, V.; Brosillon, S. Solar Photocatalysis Treatment of Phytosanitary Refuses: Efficiency of Industrial Photocatalysts. *Appl. Catal. B: Environ.* **2012,** *115-116*, 38-44.

3 – CONCLUSIONS

Crystal facet engineering is crucial for the successful synthesis of inorganic semiconductors with functional applications. For the development of functional materials, it is important to control their morphology and structure and the main goal it understands the surface chemistry, once many physical and chemical processes take places on surfaces. The morphology is a key property of materials.

In summary, in the present doctoral thesis a set of published articles in which the results are reached by a joint use of experimental and theoretical works. The main conclusions can be summarized as follows: (i) the first paper, we provide an in-depth understanding of the morphology and structural, electronic, and optical properties of $ZnWO_4$ nanocrystals. The results showed that the photodegradation of Rhodamine B under ultraviolet light irradiation was associated with the surface energy and the types of clusters formed on the surface of the catalyst. (ii) The second paper illustrated how the first-principles calculations are capable of rationalizing the mechanisms capable to stabilize a given morphology of the as-synthetized micro- and nanoparticles. This strategy allows the prediction of possible morphologies of several inorganic semiconductors by controlling the relative values of surfaces energies. (iii) The third paper demonstrated a correlation between the surface energy and the broken bonding density and the detailed configurational analysis of the different facets allowed to explain and rationalize the experimental results found in the literature. (iv) In the last paper, through the experimental and theoretical approach it was demonstrated a relationship between morphology and photocatalytic activity based on the different numbers of unsaturated superficial silver and tungsten atoms (local coordination, i.e. clusters) of each surface for α-Ag_2WO_4, crystals.

REFERENCES

1 ZARBIN, A. J. G. "Química de (nano)materiais." Quim. Nova, 30 (6): 1469, 2007.

2 DE PAOLI, M. A. "Introdução à Química de Materiais." Cadernos Temáticos de Química Nova na Escola, 2001.

3 CUSHING, B. L.; KOLESNICHENKO, V. L. & O'CONNOR, C. J. "Recent advances in the liquid-phase syntheses of inorganic nanoparticles." Chem. Rev., 104 (9): 3893, 2004.

4 SINGH, J. Electronic and Optoelectronic Properties of Semiconductor Structures. New York, Cambridge University, 2003.

5 LONGO, E.; CAVALCANTE, L. S.; VOLANTI, D. P.; GOUVEIA, A. F.; LONGO, V. M.; VARELA, J. A.; ORLANDI, M. O. & ANDRES, J. "Direct in situ observation of the electron-driven synthesis of Ag filaments on alpha-Ag_2WO_4 crystals." Sci. Rep., **3**: 1676, 2013.

6 MOREIRA, M. L.; PARIS, E. C.; DO NASCIMENTO, G. S.; LONGO, V. M.; SAMBRANO, J. R.; MASTELARO, V. R.; BERNARDI, M. I. B.; ANDRES, J.; VARELA, J. A. & LONGO, E. "Structural and optical properties of $CaTiO_3$ perovskite-based materials obtained by microwave-assisted hydrothermal synthesis: An experimental and theoretical insight." Acta Mater., 57 (17): 5174, 2009.

7 OLIVEIRA, M. C.; GRACIA, L.; NOGUEIRA, I. C.; CARMO GURGEL, M. F. D.; MERCURY, J. M. R.; LONGO, E. & ANDRÉS, J. "Synthesis and morphological transformation of $BaWO_4$ crystals: Experimental and theoretical insights." Ceram. Int., 42 (9): 10913, 2016.

8 GOUVEIA, A. F.; SCZANCOSKI, J. C.; FERRER, M. M.; LIMA, A. S.; SANTOS, M. R.; LI, M. S.; SANTOS, R. S.; LONGO, E. & CAVALCANTE, L. S. "Experimental and theoretical investigations of electronic structure and photoluminescence properties of beta-Ag_2MoO_4 microcrystals." Inorg. Chem., 53 (11): 5589, 2014.

9 WANG, L. & LI, Y. "Controlled Synthesis and Luminescence of Lanthanide Doped NaYF4 Nanocrystals." Chem. Mater., 19 (4): 727, 2007.

10 ZHAI, T.; FANG, X.; BANDO, Y.; DIERRE, B.; LIU, B.; ZENG, H.; XU, X.; HUANG, Y.; YUAN, X.; SEKIGUCHI, T. & GOLBERG, D. "Characterization, Cathodoluminescence, and Field-Emission Properties of Morphology-Tunable CdS Micro/Nanostructures." Adv. Funct. Mater., 19 (15): 2423, 2009.

11 WULFF, G. "On the question of speed of growth and dissolution of crystal surfaces." Z. Kristallogr., 34 (5/6): 449, 1901.

12 HERRING, C. "Some Theorems on the Free Energies of Crystal Surfaces." Phys. Rev., 82 (1): 87, 1951.